

POLITECNICO DI TORINO

Corso di Laurea Magistrale
in Ingegneria per l'Ambiente e il Territorio



Tesi di Laurea Magistrale

*Application of LiDAR and photogrammetry methods
at El Aljibe quarry (Toledo, Spain) to characterize the
rock mass for fragmentation prediction in rock
blasting through Kuz-Ram and xp-frag models*

Relatore

Prof. Engr. Marilena Cardu

Tutor

Prof. Engr. Pablo Segarra Catasús

Maurizio Bernardini

25 marzo 2019

Contents

Acknowledgements	10
Ringraziamenti	12
Agradecimientos.....	14
1. Introduction	1
1.1 SLIM project.....	1
1.1.1 Aims, approach and impacts of the project	2
1.2 Research background.....	3
1.3 Thesis objectives.....	3
2. El Aljibe Quarry and Arnó company	6
2.1 Geology of the area.....	10
2.2 Blasting campaign	15
3. Basic concepts	18
3.1 The origins of discontinuities	18
3.2 Geometrical properties of discontinuities.....	19
3.3 Effect of rock mass characteristics in fragmentation.....	22
3.3.1 Blastability index (Kuz-Ram model)	25
3.3.2 Rock mass discontinuity factor (xp-frag model)	28
3.3.3 Clarification on the models	30
3.3.4 Stereographic projections.....	31
4. Methods.....	34
4.1 LiDAR scanning.....	34
4.1.1 Equipment	35
4.1.2 Principles.....	38
4.1.3 Measurements	39
4.1.4 Limitations	44
4.1.5 Data processing and analysis	44
4.2 Photogrammetry	52
4.2.1 Equipment	53
4.2.2 Principles.....	53

4.2.3 Measurements	54
4.2.4 Limitations	56
4.2.5 Data processing and analysis	57
5. Results: geomechanical models of the blasts	62
5.1 LiDAR scanning results.....	62
5.2 Photogrammetry results	69
5.3 Comparison between LiDAR scanning and photogrammetry results	81
5.4 Comparison with geological compass results.....	87
5.5 Comparison with the 1 st investigation campaign.....	89
6. Calculation of rock factors	92
6.1 Blastability index (Kuz-Ram model).....	95
6.2 Rock mass discontinuity factor (xp-frag model)	97
7. Muckpiles fragmentation analysis.....	100
8. Conclusions	104
9. References	107
Appendix A: geological compass measurements.....	111
Appendix B: geo-referencing coordinates.....	112
Appendix C: manual and automatic structure maps.....	113
Appendix D: density plot resulting from DSE	118
Appendix E: photogrammetry normal set spacing.....	119
Appendix F: photogrammetry total spacing.....	120
Appendix G: stereograms comparison	121
Appendix H: normal spacing comparison.....	127
Appendix I: rock factors.....	128

Figures index

Figure 1.1: structure and objectives of the thesis	5
Figure 2.2: areal vision of the quarry, the transformation plant and the proceeced material stock	7
Figure 2.3: photogrammetric 3D model of the quarry created from drone images	8
Figure 2.4: geographic position of the extraction site	9
Figure 2.5: position of the quarry with respect to the town	10
Figure 2.6: a)Temperature/pressure diagram showing the generally accepted limits of various metamorphic facies; b)Dominant fault rock lithologies function of the stress regime (Segarra, et al., 2018)	11
Figure 2.7: main lithologies present in the specific mine site: I)ultramylonite; II)orthomylonite; III)ultracataclasite; IV)protomylonite (Fueyo and de la Cuadra, 2016)	11
Figure 2.8: position of the three stations where manual measurements were taken	13
Figure 2.9: stereografic representation of the manual measurent by the geological compass	14
Figure 2.10: stereographic representation of the 1,356 joint orientation measurements collected during the first campaign	15
Figure 2.11: reciprocal positions of the six blasts	17
Figure 3.12: schematic representations of total spacing (top), set spacing (centre) and normal set spacing (bottom), (Slob, 2010)	20
Figure 3.13: Simplified bilinear shear criterion for a joint with a regular set of triangular shaped asperities (Hack, 2003)	21
Figure 3.14: schematic representation of non-persistent, persistent and abutting joints (Slob, 2010)	22
Figure 3.15: different mechanic beahaviour in relation to the different fractures structure (Barton,1978)	23
Figure 3.16: three different blasting configurations funtion of the orientation of the joints with respect to the free face: shooting with the dip (top); shooting against the dip (centre); shooting along the strike (bottom) (Hustrulid, 1999)	24
Figure 3.17: schematically representation of the prevention of the propagation of the induced cracks by the presence of parallel-to-face joints	31
Figure 3.18: four types of stereographic projection	32
Figure 4.19: positioning of the laser scanner during the training on-site in El Aljibe quarry	35
Figure 4.20: scanstation field of view	36

Figure 4.21: scanstation components	37
Figure 4.22: operational scheme of the platform (Ravanel, et al., 2014)	39
Figure 4.23: analysed free face and positioning of the targets collimated by the total station (blast № 7)	41
Figure 4.24: six free faces object of measurements	42
Figure 4.25: blasted material at the toe of the bench (blast № 7)	43
Figure 4.26: stocked mukpiles for subsequent analysis on fragmentation (blast № 7)	43
Figure 4.27: raw resulting 3D-cloud model by CloudCompare software (non referenced)	45
Figure 4.28: trimmed model; all useless points are removed	46
Figure 4.29: rotation/translation matrix generated automatically by the software for blast № 12	47
Figure 4.30: position of the six picked points to which are assigned new absolute coordinates	48
Figure 4.31: relative position of one face to others	48
Figure 4.32: configuration for photogrammetry data acquisition; the operator frames the free face (yellow) where the six targets (red) were positioned to allow geo-referencing the resulting 3D model	52
Figure 4.33: photogrammetry equipment consists in a Canon EOS70D camera (left) and six targets (right)	53
Figure 4.34: scheme of photogrammetry acquisition, the pair of photo is taken on an imaginary baseline at a precise distance from the face (UShapeMetriX3D User Manual, 2010)	54
Figure 4.35: final configuration for photogrammetry acquisition of the six photos; in red are represented the six targets to then reference the model	55
Figure 4.36: original 3D model of the face by ShapeMetriX software (blast № 12)	58
Figure 4.37: trimmed and referenced 3D model of the face by ShapeMetriX software (blast № 12)	59
Figure 4.38: manual mapping of the joint sets for blast № 9. Subvertical in South-East direction set in red, subvertical in South-West direction set in blue and subhorizontal set in green	60
Figure 4.39: automatic cluster assignment for blast № 9. Subvertical in South-East direction set in red, subvertical in South-West direction set in blue, subhorizontal set in green and not assigned joints in black	61
Figure 5.40: 3D stereographic projection for blast № 7	63
Figure 5.41: clustered cloud before (top) and after (bottom) the removing of the cluster relative to the bench face (light blue cluster)	64
Figure 5.42: streografic projections of the six blasts form lidar scanning	66

Figure 5.43: density function plot of the normal spacing relative to the discontinuity set J1 for the blast № 12	69
Figure 5.44: manual clustering of the main discontinuity sets by the operator	71
Figure 5.45: automatic clustering of the main discontinuity sets by the ShapeMetrix software	72
Figure 5.46: projection of the planes marked in blast № 9 by the operator for SvSE set	76
Figure 5.47: projection of the planes marked in blast № 9 by the operator for Sh set	77
Figure 5.48: projection of the planes marked in blast № 9 by the operator for SvSW set	77
Figure 5.49: boxplot representation of the normal set spacing for each set	79
Figure 5.50: scheme of the traced scanlines on the automatic structure of blast № 10	80
Figure 5.51: comparison of pairs of stereograms from DSE and ShapeMetriX software. The matches are J1 with Sh, J2-J4 with SvSW, and J3-J5 with SvSE	85
Figure 5.52: comparison between geological compass measurements in station 2 (top) with principal poles individuated by LiDAR (bottom-left) and photogrammetry (bottom-right)	88
Figure 5.53: comparison between 1 st campaign measurements (top) with LiDAR principal poles (bottom-left) and all photogrammetry poles (bottom-right)	90
Figure 6.54: algorithm to mathematically assign each set of each blast to one of the 5 groups	94
Figure 6.55: representation of the Blastability index for each blast	96
Figure 6.56: representation of most unfavourable Rock mass discontinuity factor for each blast	98
Figure 7.57: muckpiles of fragmented material from blast № 7 and 8	100
Figure 7.58: muckpiles of fragmented material from blast № 9, 10 and 11	101
Figure 7.59: configuration of the scanstation for muckpiles laser scanning (second scan for blast № 7)	102
Figure 7.60: resulted segmentation: predominantly non-overlapped elements are presented in color	103
Figure C.61: manual cluster of the structure map marked by the operator	115
Figure C.62: automatic clustering of the structure map by ShapeMetriX software	117
Figure D.63: poles density plot resulting from DSE analysis	118
Figure G.64: comparison of pairs of stereograms from DSE and ShapeMetriX software. The matches are J1 with Sh, J2-J4 with SvSW, and J3-J5 with SvSE	121
Figure G.65: comparison of pairs of stereograms from DSE and ShapeMetriX software. The matches are J3 with Sh, J1-J2-J4 with SvSW	122

Figure G.66: comparison of pairs of stereograms from DSE and ShapeMetriX software. The matches are J1-J2 with SvSW, and J3 with SvSE	123
Figure G.67: comparison of pairs of stereograms from DSE and ShapeMetriX software. The matches are J1-J2 with SvSW, and J3-J4 with SvSE	124
Figure G.68: comparison of pairs of stereograms from DSE and ShapeMetriX software. The matches are J1 with Sh, J2 with SvSW, and J3-J4 with SvSE	125
Figure G.69: comparison of pairs of stereograms from DSE and ShapeMetriX software. The matches are J5 with Sh, and J1-J2-J3-J4 with SvSW	126

Tables index

Table 2.1: main rock mass description parameters (Fueyo, et al., 2016)	12
Table 2.2: schedule of the monitoring activities of the 2 nd investigation campaign in El Aljibe quarry	16
Table 3.3: different behaviour of the rock mass in function of the blasting configuration (Hustrulid, 1999)	25
Table 3.4 parameters involved in the Blastability index formulae (Cunningham, 2005)	27
Table 4.5: resolution setting options	41
Table 4.6: original and final number of point for each blast	46
Table 4.7: analysis procedure of the DSE software	49
Table 4.8: recommended and calibrated values of the input parameters	51
Table 4.9: ranges of the axle spacing S in function of the distance from the face D	55
Table 4.10: number of marked joints for each set of each blast	61
Table 5.11: orientation, density and percentage of assigned points for each set of each blast	67
Table 5.12: mean values of the normal set spacing and their relative standard deviation	68
Table 5.13: orientation, spherical aperture, K parameter, cone of confidence and density for each set of each blast	74
Table 5.14: face plane orientations and their relative pole for each blast	75
Table 5.15: mean values and standard deviation of the normal set spacing for each set of each blast	78
Table 5.16: values of mean, maximum, minimum and standard deviation of the total spacing for each blast	80
Table 5.17: matches between LiDAR (left) and photogrammetry (right) resulting sets	82
Table 5.18: angular distances between each pair of sets poles for blast № 7	85
Table 5.19: mean angular distance for all positive matches of each set of each blast	86
Table 5.20: comparison of the mean normal set spacing and its relative standard deviation for each set	87
Table 6.21: mean Blastability index results for each blast	95
Table 6.22: x ₅₀ passing fraction predicted by the Cunningham model	96
Table 6.23: most unfavourable Rock mass discontinuity factor results for each blast	97
Table 6.24: x ₅₀ passing fraction predicted by the Sanchidrián model	98

Table A.25: list of the orientation values collected in the 3 monitoring stations	111
Table B.26: coordinates of the six target points for each blast	112
Table E.27: values of the normal set spacing for each set of each blast	119
Table F.28: values of total spacing for each of the 3 scanlines for each blast	120
Table G.29: sets matches for blast № 7	121
Table G.30: angular distance (°) between matches for blast № 7	121
Table G.31: sets matches for blast № 8	122
Table G.32: angular distance (°) between matches for blast № 8	122
Table G.33: sets matches for blast № 9	123
Table G.34: angular distance (°) between matches for blast № 9	123
Table G.35: sets matches for blast № 10	124
Table G.36: angular distance (°) between matches for blast № 10	124
Table G.37: sets matches for blast № 11	125
Table G.38: angular distance (°) between matches for blast № 11	125
Table G.39: sets matches for blast № 12	126
Table G.40: angular distance (°) between matches for blast № 12	126
Table H.41: comparison of the mean normal set spacing and its relative standard deviation for each set of each blast	127
Table I.42: Blastability index results for each DSE set of blast № 7	128
I.Table 43: Blastability index results for each DSE set of blast № 8	128
Table I.44: Blastability index results for each DSE set of blast № 9	129
Table I.45: Blastability index results for each DSE set of blast № 10	129
Table I.46: Blastability index results for each DSE set of blast № 11	130
Table I.47: Blastability index results for each DSE set of blast № 12	130
Table I.48: Blastability index results for each ShapeMetriX set of blast № 7	131
Table I.49: Blastability index results for each ShapeMetriX set of blast № 8	131
I.Table 50: Blastability index results for each ShapeMetriX set of blast № 9	132
Table I.51: Blastability index results for each ShapeMetriX set of blast № 10	132
Table I.52: Blastability index results for each ShapeMetriX set of blast № 11	133
Table I.53: Blastability index results for each ShapeMetriX set of blast № 12	133

Table I.54: Blastability index value for each LiDAR and photogrammetry sets	134
Table I.55: Rock mass discontinuity factor results for each DSE set of blast № 7	135
Table I.56: Rock mass discontinuity factor results for each DSE set of blast № 8	135
Table I.57: Rock mass discontinuity factor results for each DSE set of blast № 9	135
Table I.58: Rock mass discontinuity factor results for each DSE set of blast № 10	136
Table I.59: Rock mass discontinuity factor results for each DSE set of blast № 11	136
Table I.60: Rock mass discontinuity factor results for each DSE set of blast № 12	136
Table I.61: Rock mass discontinuity factor results for each ShapeMetriX set of blast № 7	137
Table I.62: Rock mass discontinuity factor results for each ShapeMetriX set of blast № 8	137
Table I.63: Rock mass discontinuity factor results for each ShapeMetriX set of blast № 9	138
Table I.64: Rock mass discontinuity factor results for each ShapeMetriX set of blast № 10	138
Table I.65: Rock mass discontinuity factor results for each ShapeMetriX set of blast № 11	139
Table I.66: Rock mass discontinuity factor results for each ShapeMetriX set of blast № 12	139
Table I.67: Rock mass discontinuity factor value for each LiDAR and photogrammetry sets	140

Acknowledgements

The path done in these five years would have been impossible without the support of many people that are part of my life, sincerely, I win this challenge all thanks to their motivation.

Thanks to the best professor I ever met: Marilena Cardu was always enthusiast of my projects, in every moment I could rely on her with no doubts on her tireless availability. The incredible devotion towards what her work fascinated me and, at the same time, inspired me.

The wonderful experience that I lived at the Politecnico University of Madrid force me to come back to develop this thesis with an excellent group of professors. I found an exceptional confidential atmosphere, however their work shows a very high level. In particular, the professor Pablo Segarra Catusà accompanied me during my whole project, teaching me a lot and giving me great responsibilities. The professor Ana Patricia Pérez Fortes was an important reference for me, her availability allows me to learn very fast.

My parents were the columns of my work, always pushing me to get passionate about what I like to do, never curbing any of my passion. My sister, Michela, was always a solid reference to me, all this was easier following her example. I am grateful to them for having supported me in all my choices, also when this meant leaving to stay two years abroad: they accepted with enthusiasm. I actually noticed their presence more than in every other moment. Grandmother Jolanda was one of the people I miss more in this period, I want to spend so much time with her.

The best friends always were at my side and my desire to come back to see them and open up to them never turned off: I am grateful to Gabriele, Luca, Marco, Mattia and Lorenzo for all the good moments spent together. Your untiring friendship allows me to alleviate many hard times, I missed them.

The harmony I found with Nicola, Nicolas, Nicolò and Pier allows us to form a very joined group, even if far away, always we have been one beside the other, everyone with their challenge. Together we have been a winning team, as much in study as in life.

The companions of the university were my side in such a great way that it would have been impossible without them. A huge thanks to my friends Edoardo, Ettore, Donato, Matteo, Paolo, Pietro and Simone.

I chose to come back in Madrid two times, one of the most relevant reason was the company of my flatmates, but above all friends. Many thanks to Alba, Ariadna, Blanca, Gonzalo and Paula to have been my family during two exciting years. Meeting them make me fall in love with the mentality of another country and allows me to grow and improve my personality. They welcome me into their daily life with a disarming generosity and we built a great friendship that I will never forget.

I am grateful to the Aiki group of Turin: every time I come back to the dojo I felt welcomed as if it was my house. You have always been a solid example to me, I am looking forward to come back to move on the tatami with you.

Ringraziamenti

Il percorso fatto in questi cinque anni sarebbe stato impossibile senza l'appoggio di molte persone che fanno parte della mia vita, sinceramente, ho potuto completare questa sfida solo grazie alla loro motivazione.

Grazie alla migliore professoressa che abbia mai incontrato: Marilena Cardu è sempre stata entusiasta dei miei progetti, ho potuto in ogni momento contare su di lei senza alcun dubbio riguardo la sua instancabile disponibilità. La incredibile dedizione verso ciò di cui si occupa mi ha affascinato e, allo stesso tempo, ispirato.

La meravigliosa atmosfera che ho vissuto all'Università Politecnica di Madrid mi ha costretto a tornare per svolgere questa tesi con un gruppo di professori eccellente. Ho trovato un ambiente eccezionalmente confidenziale, tuttavia il lavoro che svolgono dimostra un livello veramente alto. In particolar modo, il professor Pablo Segarra Catasùs mi ha accompagnato durante tutto il mio progetto, insegnandomi moltissimo e dandomi grandi responsabilità. La professoressa Ana Patricia Pérez Fortes è stata per me un riferimento importante, la sua disponibilità mi ha permesso di imparare molto rapidamente.

I miei genitori sono state le colonne portanti del mio lavoro, spingendomi ad appassionarmi a ciò che mi piace fare, senza mai frenare nessuna mia passione. Mia sorella, Michela, è sempre stata per me un solido riferimento, seguendo il suo esempio è stato tutto più facile. Li ringrazio per avermi appoggiato in tutte le mie scelte, anche quando si è trattato di allontanarmi da loro per andare a vivere due anni all'estero, lo hanno accettato con entusiasmo. In realtà ho sentito la loro presenza più che in ogni altro momento. Nonna Jolanda è stata una delle persone che più mi è mancata in questo periodo, ho voglia di passare ancora tanto tempo con lei.

Gli amici di sempre mi sono sempre stati vicino, il desiderio di tornare per vederli e confidarmi con loro non si è mai spento: ringrazio Gabriele, Luca, Marco, Mattia e Lorenzo per tutti i bei momenti passati insieme. La loro instancabile compagnia mi ha permesso di alleviare molte fatiche, mi sono mancati.

La sintonia che abbiamo incontrato con Nicola, Nicolas, Nicolò e Pier ci ha permesso di formare un gruppo molto unito, anche se distanti siamo stati sempre uno al fianco dell'altro, ognuno con la sua propria impresa. Insieme siamo stati una "squadra" vincente, tanto nello studio come nella vita.

I compagni dell'università mi hanno affiancato in una sfida che, da solo, sarebbe stata impossibile, un immenso grazie a miei amici Edoardo, Ettore, Donato, Matteo, Paolo, Pietro e Simone.

Ho deciso di tornare a Madrid ben due volte, una delle ragioni principali era la compagnia dei miei coinquilini, ma soprattutto amici. Un grazie di cuore ad Alba, Ariadna, Blanca, Gonzalo e Paula per essere stati la mia famiglia per due emozionanti anni. Conoscere loro mi ha fatto innamorare della mentalità di un altro paese e mi ha permesso di crescere come persona. Mi hanno accolto nella loro quotidianità con una disarmante generosità e sono nate quindi delle amicizie che non dimenticherò per tutta la vita.

Un grazie al gruppo dell'Aiki di Torino: ogni qualvolta torno in quel dojo mi sento accolto come se fosse casa mia. Per me sono sempre stati dei solidi esempi, muoio dalla voglia di tornare a muovermi sul tatami con loro.

Agradecimientos

El camino recorrido durante estos cinco años hubiese sido imposible sin el apoyo de muchas personas que forman parte de mi vida, sinceramente, he podido completar este reto solamente gracias a sus motivaciones.

Gracias a la mejor profesora que he encontrado nunca: Marilena Cardu ha estado entusiasta de mis proyectos siempre, pude en cada momento contar con ella sin ninguna duda sobre su incansable disponibilidad. La increíble dedicación para lo a que se dedica me ha fascinado y, al mismo tiempo, inspirado.

La maravillosa atmosfera que he vivido en la Universidad Politécnica de Madrid me ha obligado a volver para redactar esta tesis con un grupo de profesores excelente. He encontrado un ambiente excepcionalmente confidencial, no obstante, el trabajo que hacen demuestra un nivel realmente alto. En particular manera, el profesor Pablo Segarra Catasús me ha acompañado durante todo mi proyecto, enseñándome muchísimo y dándome grandes responsabilidades. La profesora Ana Patricia Pérez Fortes ha sido para mí una importante referencia, su disponibilidad me ha permitido de aprender muy rápidamente.

Mis padres han sido los pilares de mi trabajo, empujándome a apasionarme a lo que más me gusta hacer, sin nunca frenar ninguna mía pasión. Mi hermana, Michela, siempre ha sido para mí una sólida referencia, siguiendo su ejemplo ha sido todo más fácil. Los agradezco por haberme apoyado en todas mis decisiones, también cuando se ha tratado de alejarme de ellos para ir a vivir dos años en el extranjero, lo han aceptado con entusiasmo. En realidad, he sentido su presencia más que en cualquier otro momento. Abuela Jolanda ha sido una de las personas que más he echado de menos en ese periodo, tengo ganas de pasar aún mucho tiempo con ella.

Los amigos de siempre han estado a mi lado siempre, el deseo de volver para verlos y confiarme con ellos no se ha apagado nunca: agradezco a Gabriele, Luca, Marco, Mattia y Lorenzo por todos los buenos momentos pasados juntos. Vuestra incansable compañía me ha permitido aliviar las fatigas, los he echado de menos.

La sintonía que he encontrado con Nicola, Nicolas, Nicolò y Pier nos ha permitido de formar un grupo muy unido, aunque distantes hemos estado siempre uno al lado del otro, cada uno con su propio reto. Juntos hemos estado un “equipo” ganador, tanto en el estudio como en la vida.

Los compañeros de la universidad han estado a mi lado en un reto que, solo, hubiese sido imposible, un inmenso gracias a mis amigos Edoardo, Ettore, Donato, Matteo, Paolo, Pietro y Simone.

He decidido de volver a Madrid dos veces, una de las principales razones era la compañía de mis compañeros de piso, ma sobre todo amigos. Un gracias de corazón a Alba, Ariadna, Blanca, Gonzalo y Paula por haber sido mi familia durante dos emocionantes años. Conocer a ellos me ha hecho enamorar de la mentalidad de otro país y me ha permitido crecer como persona. Me han acogido en sus cotidianidad con una desarmante generosidad y así han nacido unas amistades che no olvidaré para toda mi vida.

Un agradecimiento al grupo del Aiki de Turin: cada vez que vuelvo en ese dojo me siento acogido como si fuese mi casa. Para mi habeis siempre estado unos solidos ejemplos, me muero de la ganas de volver a moverme en el tatami con ellos.

1. Introduction

This thesis consists in the report of the active participation within the SLIM European project, coordinated by the School of Mines and Energy of the Technical University of Madrid (UPM). Thanks to the support received by the Polytechnic University of Turin, the author had the opportunity to take part in a UPM investigation campaign, carried out at “El Aljibe” quarry, during 6 months of permanence in Madrid (Spain). The author took care of part of the monitoring and analysing activities, in particular dealing with two remote sensing methods, laser scanning and photogrammetry, to characterize the rock mass and define two rock factors.

1.1 SLIM project

The SLIM project, namely “Sustainable Low Impact Mining solution for the exploitation of small mineral deposits based on advanced rock blasting and environmental technologies”, was launched in 2016 within the Horizon2020 Programme by the European Commission (under grant agreement No. 730294), and will thus be a 4-year long project. The main purposes of the investigation are: reducing investments costs, identifying environmental impacts and limit waste generation. To do this, an economic, technological and environmental point of view are adopted.

This project includes the validation of technologies developed in three different mining sites in Spain and Austria (i.e. Toledo, Granada, and Eisenerz). The initiative involves 13 active partners from Austria, Denmark, Sweden, France and Spain. These are: the School of Mines and Energy of the Technical University of Madrid (Universidad Politécnica de Madrid, UPM); 3GSM; Benito Arno e Hijos; the Bureau de Recherches Géologiques et Minières; VA Erzberg GmbH; Gate2Growth; the Luleå Tekniska Universitet; Maxam Corp. International; Minpol GmbH, the Montan Universität Leoben, Minera de Orgiva, the Technische Universitaet Graz and ZABALA Innovation Consulting.

The global budget of this project, coordinated by the School of Mines and Energy of the UPM, amounts to 6,979,200 euros. The development of an innovative technological solution, which must be sustainable and at low impact, is in the centre of the project structure and scope. In particular, the aim of this research is to increase the supply of raw materials in Europe, exploiting small mineral deposits located in the continent.

The main practical focuses of SLIM are a comprehensive characterization of explosive technologies and an exhaustive analysis on rock fragmentation, in order to create a technology that allows the measurement of muckpiles properties (in terms of size-distribution) and a new dynamic 3D-modelling system. The efficiency of the founded solutions, developed on-site in the mining site (upstream), will be tested in the corresponding processing plant (downstream).

1.1.1 Aims, approach and impacts of the project

Focusing on rock mass characterization and fragmentation models, the aim of SLIM project will be the research of an advanced blast design software and a new generation of explosives. This will provide optimized fragmentation with minimum rock damage and control of vibrations. With these new instruments, it will be possible to have a sustainable selective low impact mining solution to predict a non-linear mass fragmentation, and control airborne particulate matter, vibrations and nitrate leaching.

Particular attention will be given to the exploitation of small mineral deposits, including chemical complex ore-forming phase. Indeed, in Europe, small mining sites are more numerous than large ones, but at the same time a large variety of minerals can be found. The exploitation of this mineral variety could make the continent less dependent on other countries, from both an economic and a political point of view. Moreover, upstream/downstream approach will be used to validate the technical solutions, first working on-site in the quarry, and then in the processing plants that receive the exploited material. This method will guarantee technical and practical performance to every single process scheme.

The worker safety and the environmental and social aspects are not less important in the SLIM project: this will allow to support the sector sustainability and local community involving. Informing and communicating is an important issue in the mining word, and innovation would help people being more disposed to understand the importance of this sector, impacting positively in population consciousness. Surveying and interviewing actions combined with information and educational campaigns enables to prove the social responsibility of the members of the project.

1.2 Research background

A previous investigation campaign of large scale tests was performed in the quarry from the end of May to the end of September 2017. This first campaign consisted of six blasts located in the same pit where the second campaign was executed, which is object of this thesis. The distance between the investigated areas is approximately 35 m. All the blasts had seven blastholes along one row parallel to the free vertical face of the bench and they consisted of a free surface of less than 25 m long and height about 11.5 m (Segarra, et al., 2018).

The investigation includes the monitoring of the rock mass condition before the blast by: LiDAR scanning of the free face (Fernandez, et al, 2017), data acquisition for photogrammetry analysis (Gomes, et al., 2018) and blastholes deviation recording (Segarra, et al., 2017). Then, different blasting information were collected: detonation velocity, detonation pressure (Segarra, et al., 2017), dust dispersion (Segarra, Sanchidrián, 2017), near seismic vibrations (Sanchidrián, 2017), high speed camera video (Navarro, et al., 2017). Finally, some post-blast measurements were added: televiewer recording (Gomes, et al., 2017), dust sampling, drone ortho-photos collecting (Iglesias, 2017) and LiDAR scanning of the resulting muckpiles (Fernandez, et al, 2017).

1.3 Thesis objectives

This study consists in the validation of the techniques developed in the first part of SLIM project to characterize the rock mass for fragmentation prediction in rock blasting through Kuz-Ram and xp-frag models.

In particular, the investigation work is based on two different remote sensing techniques: digital photogrammetry and laser scanning monitoring (LiDAR). By this way, the exposed rock outcrop can be digitalized with high accuracy in a 3D-points cloud which allows software to detect the fractures structure. From this point, the existing discontinuity datasets can be extracted and analysed by means of their orientation and spacing. This results enable to characterize the rock mass and predict the fragmentation in rock blasting through the Kuz-Ram and the xp-frag models. Then, two rock factors will be calculated: the Blastability index and the Rock mass discontinuity factor.

On the other hand, the use of two different techniques allows an effective comparison of their effectiveness and uncertainty (presented in paragraph 5.3). The use of the digital photogrammetry method (based on *manual mapping* of joints) is more consolidated; therefore, it is more reliable. However, the processing of data from laser scanning, based on a *semi-automatic analysis* procedure, can be executed faster and provides a higher resolution of points. One of the scope of this study will be the calibration of the parameters to input in the software, basing on rock mass condition of the specific site, so that results can be congruent to photogrammetry. A double-test investigation ensures obtaining reliable results and a mutual verification.

Finally, laser scanning is performed on muckpiles from each blast to analyse the fragmentation by means of the grain size distribution. By this way, the effectiveness of the rock factors and the methodologies used could be tested: a correlation between the median grain size predicted by the models and the median grain size estimated by the fragmentation analysis is expected. However, this last verification will be carried out in future works, when the results will be available. In Figure 1.1 a schedule flowchart shows the order of the operations.

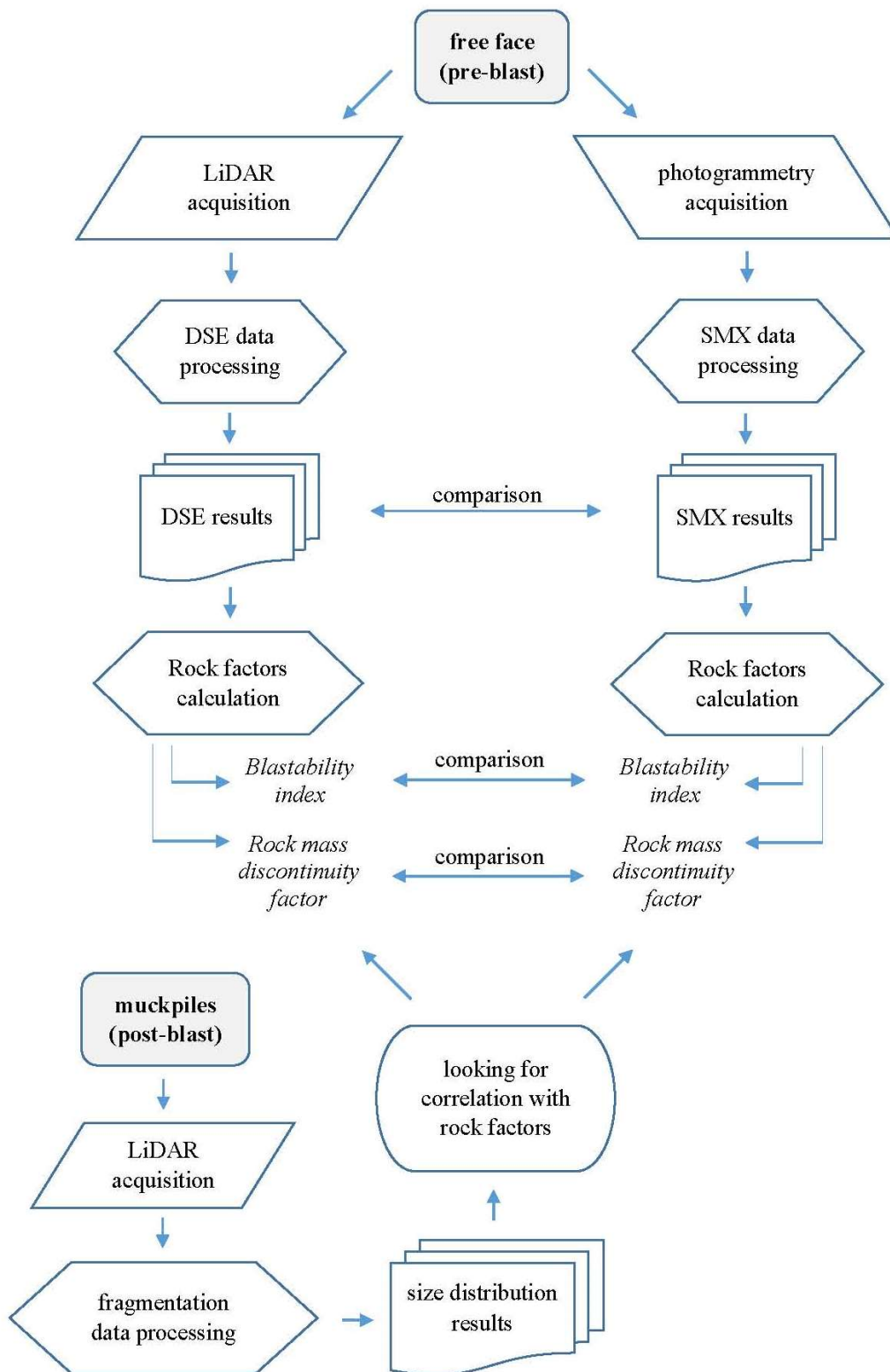


Figure 1.1: structure and objectives of the thesis

2. El Aljibe Quarry and Arnó company

The quarry, located near Toledo (Spain), is an open pit exploitation in mylonite, a metamorphic rock deposit. The exploitation belongs to Benito Arnó e Hijos S.A.U. and has been developed for more than 12 years. Thanks to its characteristics of hardness to wear and fragmentation, the exploited material is very suitable for the manufacture of ballast for rail use (32-56 mm) and pellets for freeways asphalt agglomerates (6-12 mm).

El Aljibe quarry has played a very important and strategic role in the construction of Spanish high speed line (AVE), especially to connect Sevilla, Toledo and Valencia to Madrid. The Arnó company constructed also the Tembleque railway station to allow the transport of the manufactured material.

The mining site, as will be explained in paragraph 2.4, has been studied for many years by the School of Mining and Energy Engineering of the Technical University of Madrid (Segarra, et al., 2018), with the financing by “Cátedra Maxam” (Maxam Civil Explosives) that is a partner of the university.

As Figure 2.2 shows, the quarry has a deep concave structure that often causes water storage problems because the bottom level of the pit is below the water table: in fact “el aljibe” means “the cistern”. The transformation plant and the processed material stock are also visible.



Figure 2.2: areal vision of the quarry, the transformation plant and the processed material stock

In Figure 2.3 a photogrammetric 3D model of the quarry created from drone images is shown. The model was realized with orthophotos collected by a Phantom 4 drone and the digital reconstruction was made by the software ShapeMetriX 3D-SMX (3GSM, 2010) by Luis Iglesias, a UPM SLIM project team member.

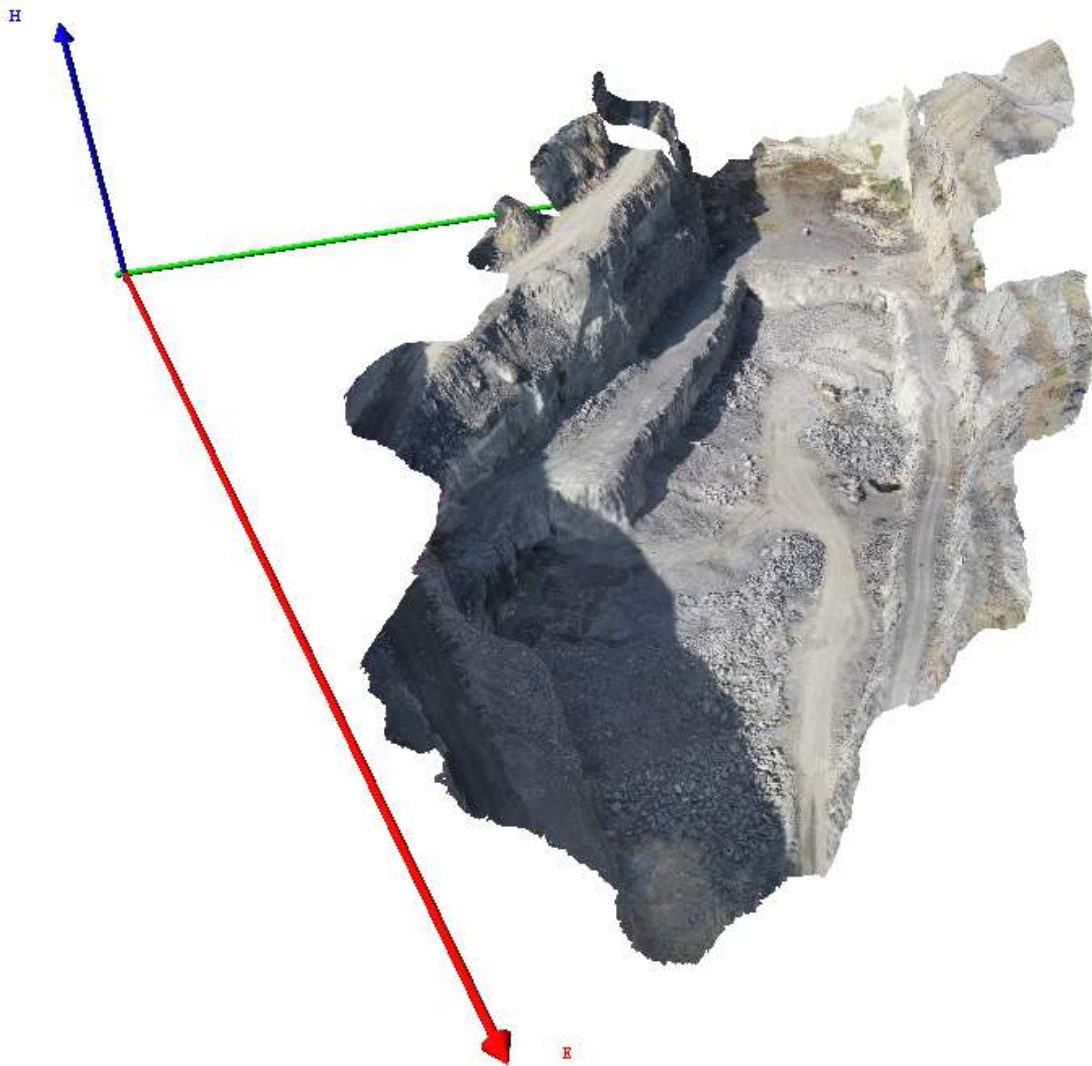


Figure 2.3: photogrammetric 3D model of the quarry created from drone images

Arnó company is a benchmark company of the Spanish sector of construction that was founded in 1965 and is nowadays present in different fields other than construction, such as civil engineering, material production, energy service, logistics and facility management. The company is partner of leading national construction companies and owns developed experience as a contractor for the public administration.

The material produced is used in company activities and is also sold to others. In particular, for the supply of arid material, Arnó relies on different quarries and plants around the Spanish territory. Different igneous and metamorphic rocks are exploited in three main sites: ophite in La Soriana

quarry (Huesca, Spain), andesite in Atienza quarry (Guadalajara, Spain) and mylonite in El Aljibe quarry (Toledo, Spain). Silicic arid and calcareous rocks are extracted, too.

El Aljibe quarry is located in the small town of Almonacid de Toledo (Toledo, Castilla-La Mancha, Spain) and is 90 km far from Madrid (see Figure 2.4 and 2.5); its elevation is 720 m a.s.l. The central position is strategically convenient to allocate the manufactured material almost all over the country.



Figure 2.4: geographic position of the extraction site



Figure 2.5: position of the quarry with respect to the town

2.1 Geology of the area

The exploited rocks in El Aljibe quarry belongs to a metamorphic belt 1-1.5 km long and 400 m high (Martínez-Salanova, et al., 2009). This belt responds to a ductile shear zone which was developed during the final tectonic event in the Hercinian Orogeny (Enrile, 1981). This geological structure gave origin to mylonite and cataclasite series.

Mylonites from El Aljibe derived largely from migmatites formed in amphibolite facies conditions of pressure and temperature, which are 400 °C and 0.4 GPa according to Figure 2.6-a. In the lower part of the deposit, where the confining pressure and temperature were higher, mylonite and ultramylonite are present, as shown in Figure 2.6-b (Segarra, et al., 2018).

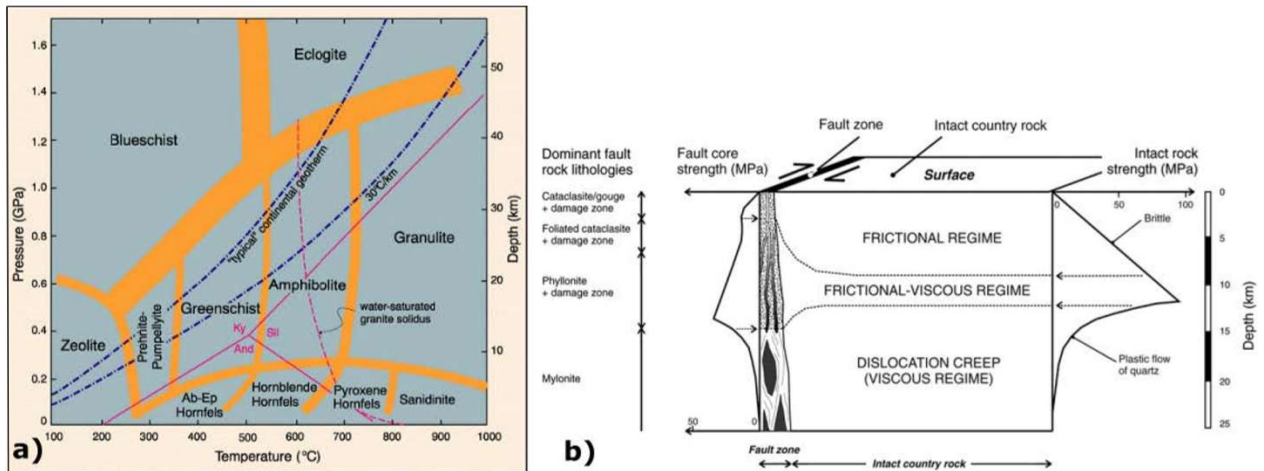


Figure 2.6: a) Temperature/pressure diagram showing the generally accepted limits of various metamorphic facies; b) Dominant fault rock lithologies function of the stress regime (Segarra, et al., 2018)

The main lithologies present in the mine site are ultramylonite (Figure 2.7-I), orthomylonite (Figure 2.7-II), ultracataclasite (Figure 2.7-III) and protomylonite (Figure 2.7-IV). The predominant rock type in El Aljibe quarry is orthomylonite, which is mylonite of magnetic protholyte. It is formed by tectonic forces, its density is 2.71 t/m³ and it is very hard and tough.

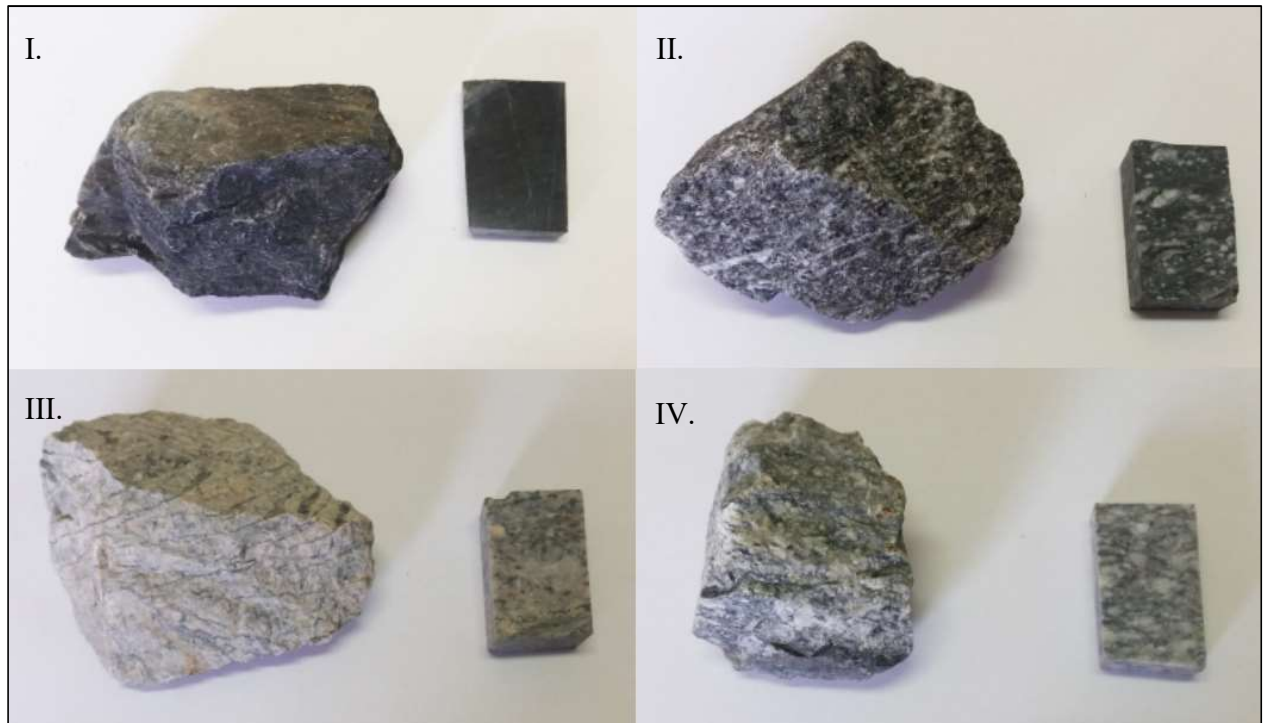


Figure 2.7: main lithologies present in the specific mine site: I) ultramylonite; II) orthomylonite; III) ultracataclasite; IV) protomylonite (Fueyo and de la Cuadra, 2016)

According to their composition, the mylonites have a porphyry-clastic texture with potassium feldspar and plagioclase clasts encompassed in a matrix with biotite foliation recrystallized in quartz crystals (Benito Arnó e hijos, 2016). The mylonite band affects a strip of the Mora-Gálvez granite pluton that extends south of Toledo. The exploited mylonites show a porphyroblastic texture with potassium and plagioclase feldspar phenoblasts encompassed in a matrix of biotitic foliation recrystallized with quartz crystals.

In addition, a geology assessment conducted in El Aljibe quarry by Arnó company is shown in Table 2.1.

Table 2.1: main rock mass description parameters (Fueyo, et al., 2016)

Parameter	Value
Uniaxial compressive strength	182.3 MPa
Density	2710 kg/m ³
Young's modulus	19.8 GPa

In this study, the whole area of the quarry is geologically investigated to understand the mechanism of the ore deposit formation and the tectonic forces that subsequently modified it. One of those monitoring consists in the measurement of the orientation of the visible joints that lean out from the surface by the geological compass. In particular, 85 manual measurements, collected in the 3 stations shown in Figure 2.8, are collected. The entire data list is available in Table A.21 of Appendix A.



Figure 2.8: position of the three stations where manual measurements were taken

In Figure 2.9 a stereographic representation of the poles of the joints, created by RockWorks (RockWare, 2016), is reported. In paragraph 5.4, those data will be compared to the results from semi-automatic analysis of LiDAR and manual mapping of photogrammetry.

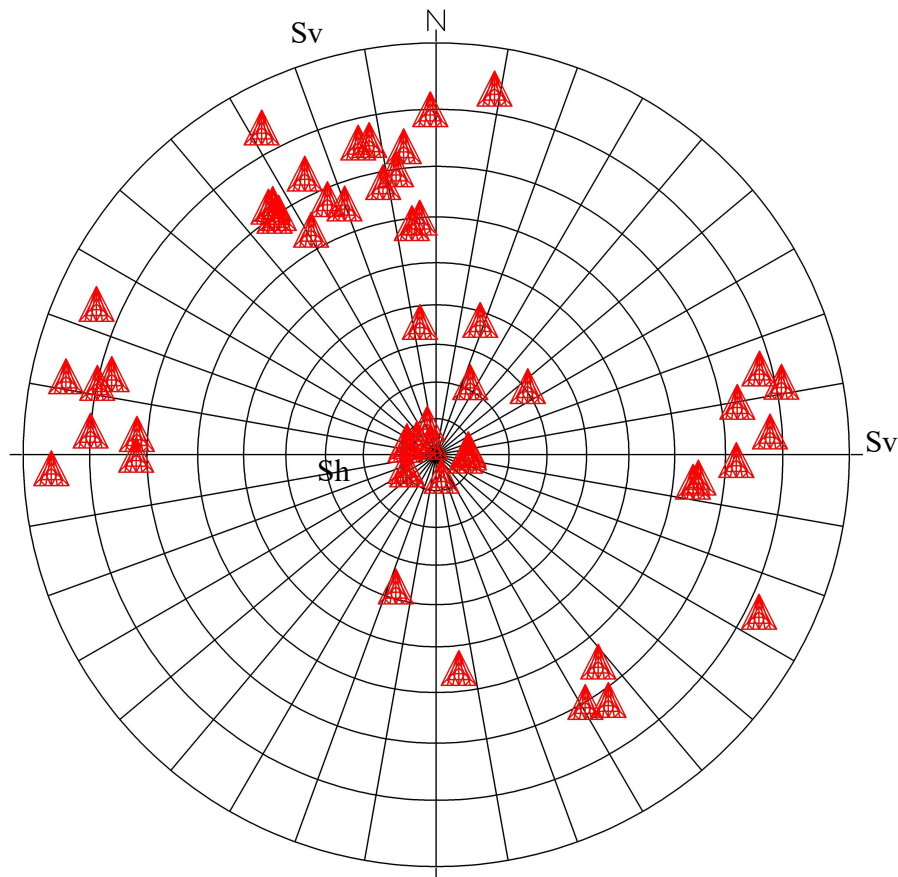


Figure 2.9: stereographic representation of the manual measurements by the geological compass

The joints poles tend to group in different clusters, as a consequence of a defined structure of discontinuities. In particular, three main families can be considered: one subhorizontal (Sh) and two subvertical (Sv).

During the first campaign, carried out from May to September 2017, a total amount of 1,356 measurements of the joints orientations were collected. Those data derive for three different investigation methods: photogrammetry monitoring, geological compass data collection and Televiewer inspection. The latter technique consists in a logging tool with an optical camera that is lowering through the borehole while collecting 360° oriented image of the hole walls from which is possible to individuate joints orientation. All these data are grouped by the RockWorks16 software in the stereographic diagram of Figure 2.10.

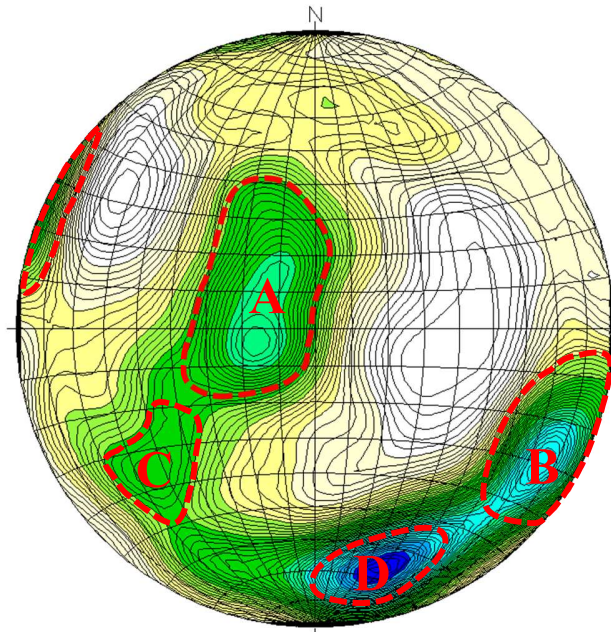


Figure 2.10: stereographic representation of the 1,356 joint orientation measurements collected during the first campaign

From the results in Figure 2.10 two main tectonic events were individuated. A first tectonic event which is the most important, is relative to the subhorizontal family marked as “A”. At the same time another set was generated, represented with the “D” zone. A second tectonic event, subsequent to the first one, generated the subvertical joints belonging to “B” and “C” families. By comparison with Figure 2.8, a match can be individuated between Sh and “A”, and between Sv and “D” and “B”.

In paragraph 5.5, that information will be compared to the result of this study.

2.2 Blasting campaign

This study reports and analyses the results from the second blasting campaign of the SLIM project. The campaign consisted in the monitoring of a large variety of parameters, those measurements have been carried out before, simultaneously and after 6 programmed blasts. This thesis refers particularly to the assessment of pre-blast rock conditions. For this purpose, two techniques of investigation were adopted (LiDAR scanning and photogrammetry), but much more data were collected by other methods by the whole university team. Table 2.2 lists all different tests and date of execution. Measurements made by the writer are shown in bold.

Table 2.2: schedule of the monitoring activities of the 2nd investigation campaign in El Aljibe quarry

	Date	Pre-blast measurements			Simultaneous measurements				Post-blast measurements			
		LiDAR (free face)	Photogrammetry (free face)	Blasthole deviation	Dust monitoring	Datatrapp II	Near seismic	High speed camera	Televiever	Dust sampling	Drone flight	LiDAR (muckpiles)
Training	Oct, 23 th 2018	X	X	X					X		X	
Blast 7	Nov, 26 th 2018	X	X	X	X	X	X	X	X	X	X	
Blast 8	Dec, 3 th 2018	X	X	X	X	X	X	X	X	X	X	
Blast 9	Dec, 13 th 2018	X	X	X	X	X	X	X	X	X	X	
Blast 10	Dec, 17 th 2018	X	X	X	X	X	X	X	X	X	X	
Blast 11	Dec, 20 th 2018	X	X	X	X	X	X	X	X	X	X	
Blast 12	Feb, 8 th 2019	X	X	X	X	X	X	X	X	X	X	
Fragmentation analysis (B7)	Jan, 30 th 2019											X
Fragmentation analysis (B7, B8)	Feb, 6 th 2019											X
Fragmentation analysis (B9, B10)	Feb, 15 th 2019										X	X
Backbreak analysis	Feb, 21 th 2019		X						X			

Each blast consists in a single row of 7 89 mm holes with a burden and a spacing of around 3 m, the benches height is 12 m. The blastholes were executed, with a nominal inclination of 20°, by a Tamrock DX-800 with an installed measuring-while-drilling system (MWD). The charge was a

double salt emulsion sintetized with microspheres (Riomex DS10000) experimentally manufactured by MAXAM; electronic detonators were adopted as initiation system. The stemming consists of drilling chips. Figure 2.11 shows the 6 blasts at the bottom of the pit.

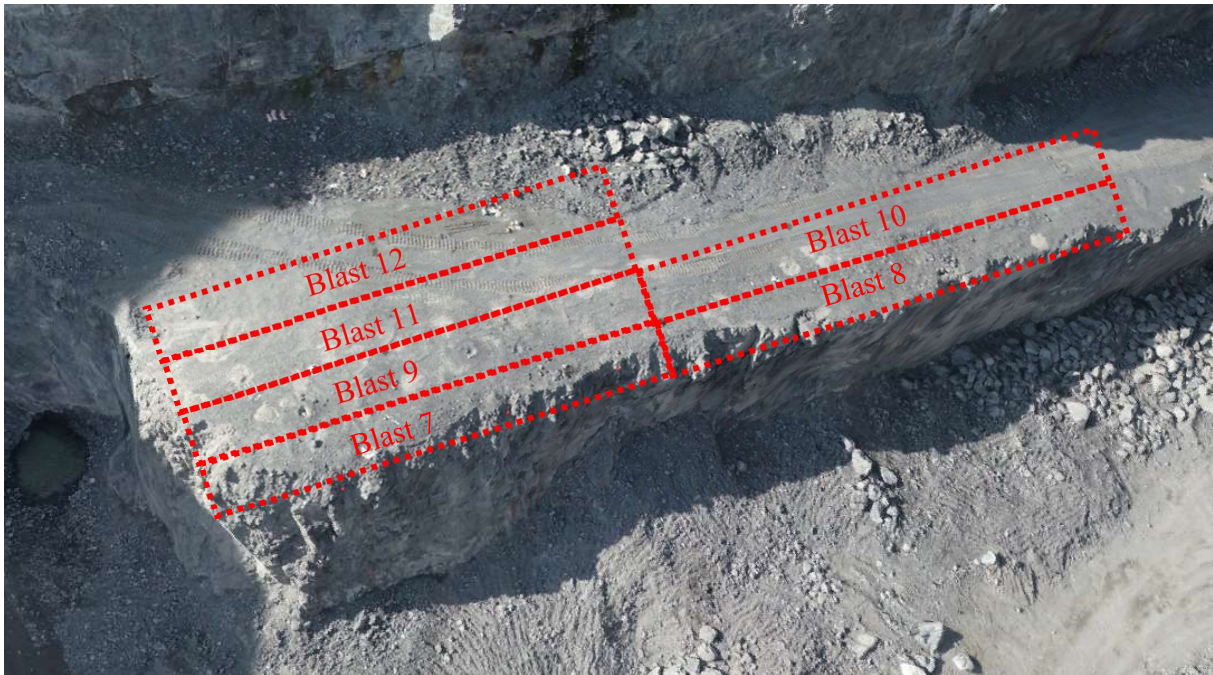


Figure 2.11: reciprocal positions of the six blasts

3. Basic concepts

In order to characterize the rock mass behaviour in blasting, strength properties of the intact rock are not sufficient, as geotechnical conditions of the rock mass affect blast results, due to its heterogeneity and anisotropic nature. Primary causes of these differences with respect to intact rock conditions are discontinuities derived from joints, faults, bedding planes (sedimentary rocks) and foliations (metamorphic rocks). Mechanical discontinuities represent the majority of the “planes of weakness” of the rock mass, reducing shear strength along the plane and tensile strength perpendicular to the plane, in comparison to the intact rock nearby it.

3.1 The origins of discontinuities

First of all, a general classification into two main groups of discontinuities is necessary: *relevant discontinuities* (scale of centimetres), which can cause an effective variation of the rock mass behaviour, and *integral discontinuity* which do not change it. An *integral discontinuity* could be due to foliation in gneisses caused by segregation of minerals into distinct bands or the change in grain size and mineral content observed in sedimentary rocks (Slob, 2010). However, this type of discontinuity may become of mechanical relevance as a result of weathering or stress conditions changes: for example, in some metamorphic rocks, weathering of their internally aligned mineral grains, can develop marked mechanical discontinuities. Others factors, such as stress release, can be added to weathering causing displacement and distortion. On the other hand, other factors, such as cementation or mineralization, can sometimes cause a marked discontinuity to become an *integral discontinuity*.

In all cases, the style of the resulting deformation depends on interactions among a number of physical and chemical factors (Slob, et al., 2010), including:

- the severity of the strain forces;
- the degree of confining pressures;
- temperature;
- the rate at which the deforming forces are applied;
- the rate at which the deformation proceeds;
- the presence and pressure of pore fluids;

- the composition of the rock, and the presence of fluids in the porous media.

In general, discontinuities are due to past large-scale geological processes like tectonics, volcanism, shearing, metamorphism, uplift, sedimentation, etc. These phenomena can induce different types of anisotropy in the rock mass: joints, faults, shears, foliation, fractures and bedding planes.

3.2 Geometrical properties of discontinuities

Identifying and evaluating discontinuities characteristics is a crucial aspect to consider in blasting engineering. In order to achieve this goal, geologists and engineers refer to the four following geometrical properties:

- **Orientation:** it is composed by two variables, the dip direction and the dip angle of planes. The former is a line perpendicular to the intersection of the plane with the horizontal and is usually referred to the North. The latter is the maximum declination of the plane with respect to the horizontal and it is measured in degrees (Slob, 2010). Often, the normal vector exiting the plane is used to define the orientation, especially when a hemispherical projection is required (useful for the recognition of discontinuity sets). Usually there are one or more preferred orientations (sets) in a rock mass and the individuation of these families is the key for characterization.
- **Spacing:** it is useful to define the average distance between the discontinuities in order to predict blocks maximum size (especially in mining activities) and mechanical behaviour (blastability and excavatability). Spacing can be measured with three different methods (i.e. *total spacing*, *set spacing*, and *normal set spacing*). *Total spacing* is the distance between a pair of adjacent discontinuities measured along a scanline. *Set spacing* is instead the measured distance only between joints of the same set. Finally, the scanline for *normal set spacing* must be perpendicular to the average orientation of that set. A schematic explanation is shown in Figure 3.12.

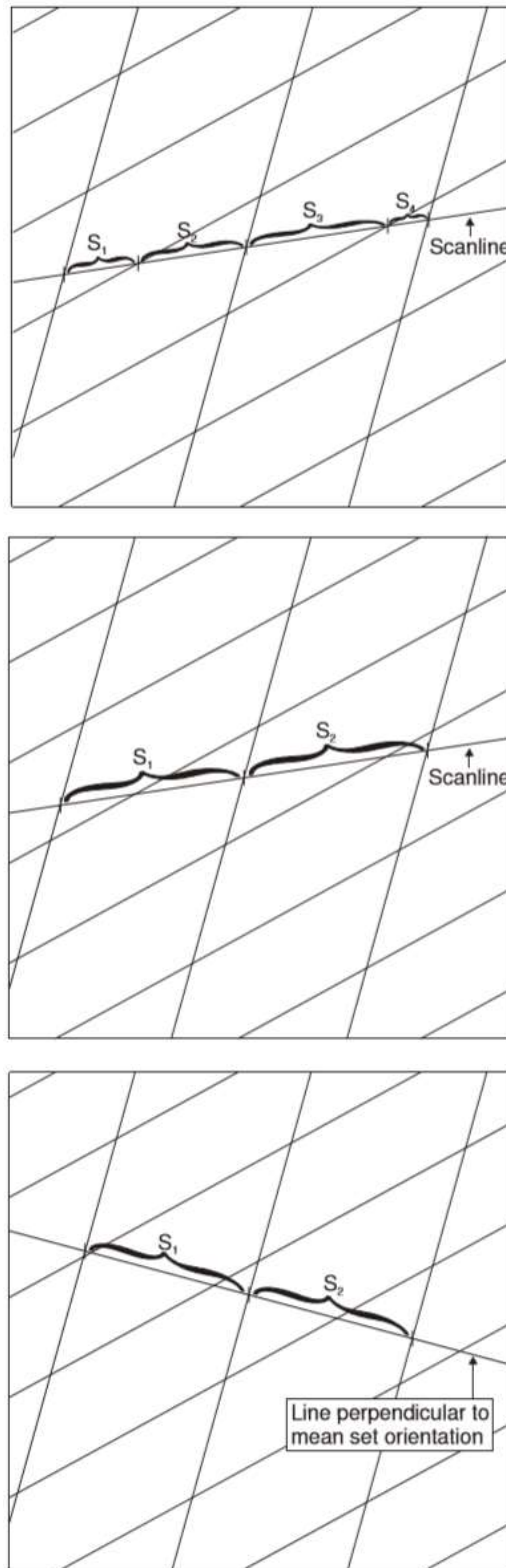


Figure 3.12: schematic representations of total spacing (top), set spacing (centre) and normal set spacing (bottom), (Slob, 2010)

- **Surface roughness:** it is responsible of interlocking between rock blocks (large scale) and influences the local shear strength (small scale). Smoothed and planar interfaces have minor shearing resistance than the stepped or undulated ones. Shear strength can be calculated by the friction angle of the intact rock and the geometry of the discontinuity roughness profiles. In particular, small displacements are mainly governed by second-order asperities, but large displacements depend more on those of the first-order (Patton, 1966). A schematic model is shown in Figure 3.13. Generally, this parameter is not considered in current rock factors indexes.

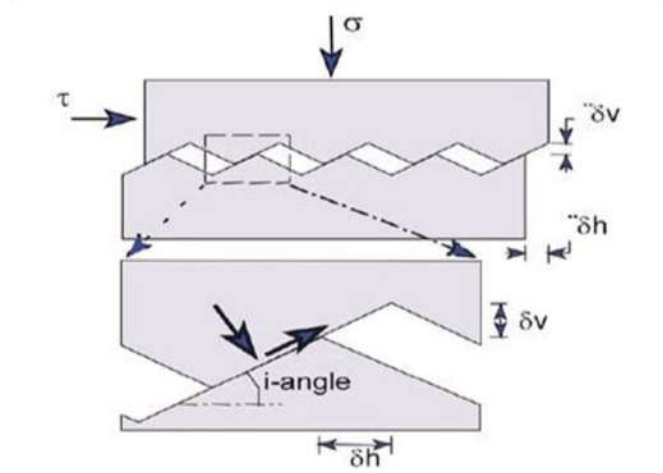


Figure 3.13: Simplified bilinear shear criterion for a joint with a regular set of triangular shaped asperities (Hack, 2003)

- **Persistence:** it is the length of the joints plane. Indeed, sometimes fractures end within the intact rock, whereas in other cases these end against other fractures, thus individuating a rock block. The careful observation of this property is helpful to understand the geological history of the rock mass: later joints tend to be shorter, ending either against earlier ones (*abutting* discontinuities) or within the intact rock (*non-persistent* discontinuities), whereas the earlier ones are longer and continuous (*persistent* discontinuities). Differences between those three types of persistence are shown in Figure 3.14. This property is neither considered in rock mass indexes.

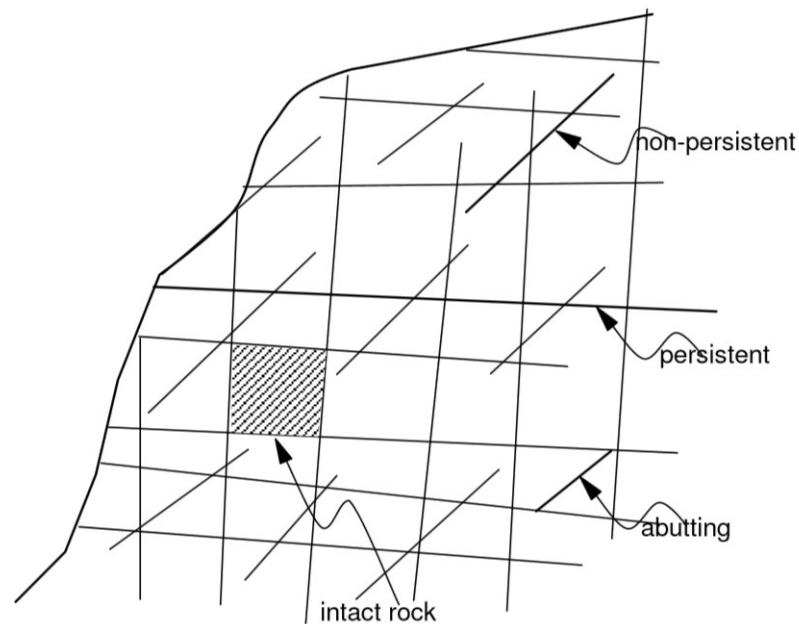


Figure 3.14: schematic representation of non-persistent, persistent and abutting joints (Slob, 2010)

3.3 Effect of rock mass characteristics in fragmentation

The ideal condition of an intact rock is rarely found in nature; in fact, a rock mass has a lot of anisotropic characteristics, causing a complex behaviour in shear creation. Also, pre-existing fractures can cause a change in the orientation of the stress regime, completely altering the conditions. Spacing and orientation of shear failure plans are dependent on both bedding planes and mineral internal distribution. For this reason, a careful geological analysis of the number and types of joints is of great importance for blast design towards proper results in terms of fragmentation and rock motion.

Response of the rock mass to blasting can be very different depending on the orientation and the number of joints, even under the same external conditions. Figure 3.15 schematizes how two different fracture structures can affect differently the mechanic behaviour of the rock mass. Sizes and shapes of rock blocks are dictated by intersections of discontinuities: for this reason, few joints differently oriented between each other can have a greater effect on stability than a great number of pseudo-parallel joints.

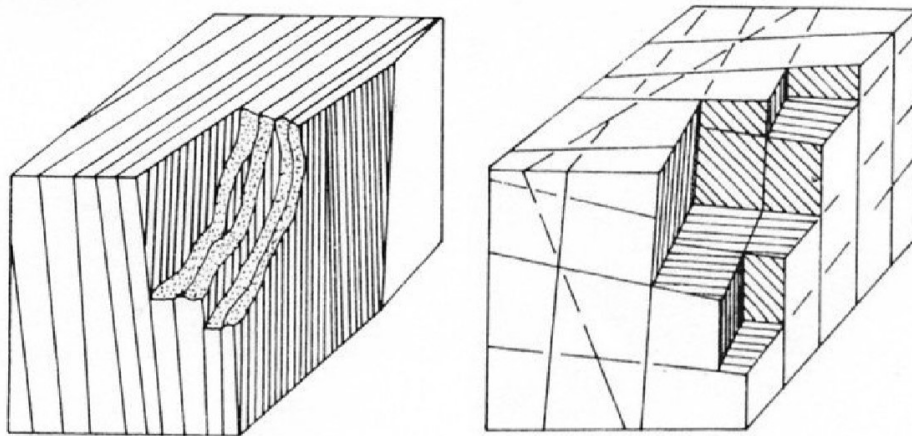
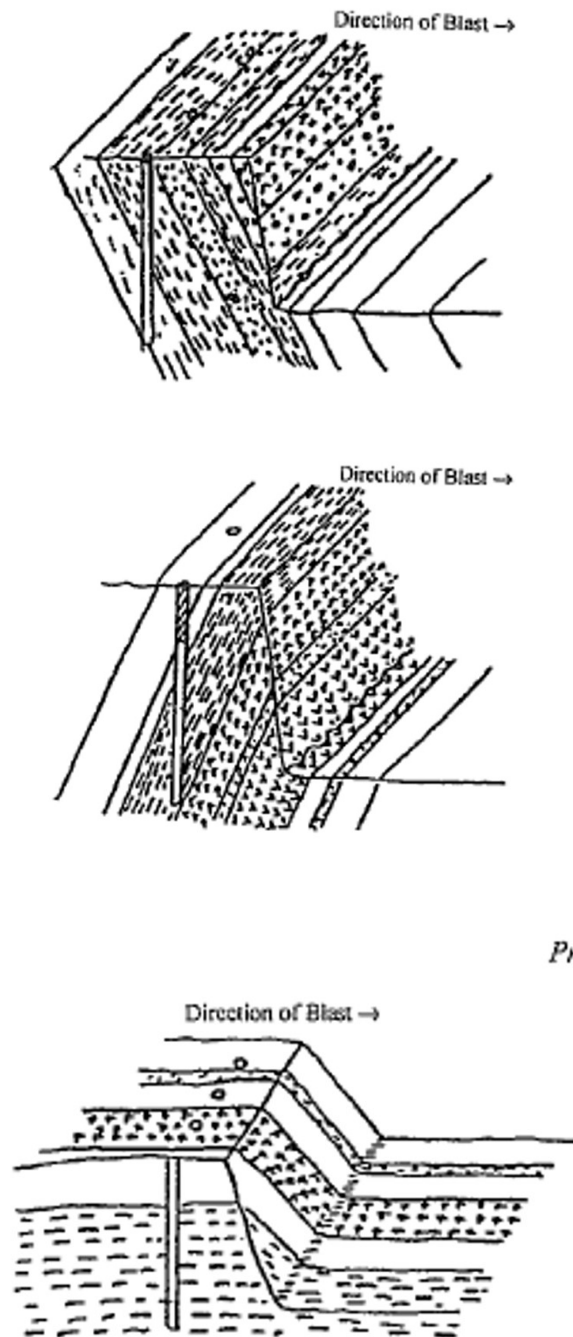


Figure 3.15: different mechanic behaviour in relation to the different fractures structure (Barton, 1978)

In rock blasting many studies tried to give a “rock factor” definition to incorporate rock mass characteristics in prediction formulas of fragmentation or mucking efficiency. Prediction of the size distribution of the fragmented rock constitute a challenge that has been undertaken for decades. These models incorporate the rock mass characteristics, the blast design parameters and the explosive properties. The blasting engineer has now the means, in the form of formulae, to relate the parameters of a given size distribution function to the rock properties and the blast design parameters (Sanchidrián, et al., 2016).

Another relevant aspect to consider for rock mass characterization is the orientation of the joints with respect to the free face to blast. To explain this concept three main cases are shown in Figure 3.16.

- a) Shooting with the dip
- b) Shooting against the dip
- c) Shooting along the strike



Pr

Figure 3.16: three different blasting configurations function of the orientation of the joints with respect to the free face: shooting with the dip (top); shooting against the dip (centre); shooting along the strike (bottom) (Hustrulid, 1999)

Those different conditions highly influence blast results, in particular can affect the backbreak, the toe removal efficacy, the condition of the residual pit floor and the displacement of the muckpile. In Table 3.3, different behaviours of the rock mass are shown.

Table 3.3: different behaviour of the rock mass in funtion of the blasting configuration (Hustrulid, 1999)

	Backbreak	Toe removal problems	Floor condition	Muckpile displacement
Shooting with the dip	high	low	smooth	high
Shooting against the dip	low	high	rough	low
Shooting along the strike	irregular	high	sawtoothed	low

As observable, if backbreak does not presents a problem, the best configuration is found when shooting with the dip. Certainly, the shooting along the strike condition is the worst one; in this case, a re-orientation of the free face is recommended.

Clearly, real conditions are different compared to those previously introduced; however, a more complex structure of joints is commonly found. For this reason, the rock factors estimation is quite difficult to obtain. For the achievement of this study, results of joints sets orientation and spacing from LiDAR scanning and photogrammetry will be the input for the calculation of the two rock factors: Blastability index and Rock mass discontinuity factor. Then, will be also important to assess the uncertainty in the measurements.

3.3.1 Blastability index (Kuz-Ram model)

Different models to predict fragments mean size and fragment size distribution have been developed since the '930s and have been improved during the years.

One of the most relevant is the Kuznetsov's formulae (1973), which express the mean fragment size x_m (Cunningham, 2005):

$$x_m = A \cdot q^{-0.8} \cdot Q^{\frac{1}{6}} \quad eq.1$$

where A is a rock strength factor in the range 7-13, q is the powder factor ($\text{kg}_{\text{TNT.EQ.}}/\text{m}^3$), and Q is the charge per hole ($\text{kg}_{\text{TNT.EQ.}}$).

The amounts of explosive in the powder factor and in the charge per hole are given in TNT equivalent mass, which can be calculated multiplying the mass of explosive by its relative strength with respect to TNT. So, if q and Q are referred to the explosive mass, the equation 1 can be written as:

$$x_m = A \cdot q^{-0.8} \cdot Q^{\frac{1}{6}} \cdot \theta^{-\frac{19}{30}} \quad eq.2$$

where θ is the explosive relative strength with respect to TNT and x_m is the mean size of a Rosin-Rammler distribution.

In 1983, Kuznetsov's formulae was spread by Cunningham who referred to ANFO and not to TNT anymore. In this case, the median fragment size x_{50} is expressed by:

$$x_{50} = A \cdot q^{-0.8} \cdot Q^{\frac{1}{6}} \cdot \left(\frac{RWS}{115}\right)^{-\frac{19}{30}} \quad eq.4$$

where RWS is the relative weight strength (which is always referred to ANFO) of the explosive and 115 is the relative weight strength of TNT. Furthermore, the blastability index A is now expressed as:

$$A = 0.06 \cdot (RMD + RDI + HF) \quad eq.5$$

This formula derives from Lilly (1992). Meanings of involved parameters of this formula are expressed in Table 3.4.

Table 3.4 parameters involved in the Blastibility index formulae (Cunningham, 2005)

RMD (Rock mass description)	
Powdery/friable	10
Vertically jointed	$JF^{(*)}$
Massive	50
$JF^{(*)} = JPS + JPA$ (Joint factor)	
JPS (Joints plane spacing)	
$S_J < 0.1$ m	10
$0.1 \leq S_J < 0.3$ m	20
$0.3 \text{ m} \leq S_J < 0.95 \cdot (B \cdot S)^{1/2}$	80
$S_J > (B \cdot S)^{1/2}$	50
JPA (Joint plane angle)	
Horizontal	10
Dip out the face	20
Strike perpendicular to the face	30
Dip into the face	40
RDI (Rock density influence)	
$= 25 \cdot RD - 50$	
HF (Hardness factor)	
$= Y/3$ if $Y < 50$	
$= UCS \cdot 5$ if $Y > 50$	

S_J : average joint spacing; B : burden; S : spacing; Y : Young's modulus (GPa);
 UCS : uniaxial compressive strength (MPa); RD : rock density (t/m^3).

In 2005, Cunningham corrected his formulae by adding a delay-dependent factor A_t (Bergmann, et al., 1974) and a factor $C(A)$ for the correction of the median size ($0.5 < C(A) < 2.0$). The final expression is:

$$x_{50} = A \cdot A_t \cdot q^{-0.8} \cdot Q_6^{\frac{1}{6}} \cdot \left(\frac{RWS}{115} \right)^{-\frac{19}{30}} \cdot C(A) \quad eq.6$$

where A_t is defined as:

$$A_t = 0.66 \cdot \left(\frac{\Delta T}{T_{max}} \right)^3 - 3.13 \cdot \left(\frac{\Delta T}{T_{max}} \right)^2 - 1.58 \cdot \left(\frac{\Delta T}{T_{max}} \right) + 2.1 \quad \text{if } \frac{\Delta T}{T_{max}} < 1 \quad eq.7$$

$$A_t = 0.9 + 0.1 \cdot \left(\frac{\Delta T}{T_{max}} - 1 \right) \quad \text{if } \frac{\Delta T}{T_{max}} > 1 \quad eq.8$$

and

$$T_{max} = 15.6 \cdot \frac{B}{c_P} \quad eq.9$$

where ΔT is the in-row delay in ms, B is the burden in m and c_P is the P-wave speed in m/ms. As dictated by equations 7 and 8, A_i is not continuous when the ratio $\Delta T/T_{max}$ is equal to 1; a possible correction could be replacing the constant term 2.1 in equation 7 by 2.05 (Sanchidrián, et al., 2016).

Equations 1 and 2 are written for the mean size (x_m) of a Rosin-Rammler distribution that was assumed to accurately describe the fragmented rock, from which the name “Kuz-Ram model”. The Rosin-Rammler, or Weibull, cumulative distribution function is (Cunningham, 2005):

$$P(x) = 1 - \exp\left[-\left(\frac{x}{x_c}\right)^n\right] = 1 - \exp\left[-\ln 2 \left(\frac{x}{x_{50}}\right)^n\right] \quad eq.3$$

where x_c is the characteristic size (the size for which the passing size is $1-1/e$, or 63.2%), n is a shape factor and x_{50} is the median size.

Calculation of Blastability factor A for all six scans will be done in paragraph 6.1.

3.3.2 Rock mass discontinuity factor (xp-frag model)

Another model was recently defined by Sanchidrián and Ouchterlony and derived from the asteroid collision theory. This is a distribution-free model that, for different percentage passing, gives fragment sizes based on rock mass and blast characteristics (Sanchidrián, et al., 2016). By this way a particular distribution function is not needed. A better performance was observed with respect to classical models as “Kuz-Ram” or “Crush-zone” ones.

The model was calibrated using fragmentation data collected from 169 blasts published in literature. This approach consists in the description of discontinuities by means of a combination of only two terms: a joint spacing term J_S and an orientation term J_O . Then, the Rock mass discontinuity factor J_F is now defined as:

$$J_F = J_S + J_O \quad eq.10$$

The first term is formulated as a non-dimensional ratio, but a limiting values a_s is required for large joint spacing, so:

$$J_S = \min\left(\frac{S_j}{L_j}, a_s\right) \quad eq.11$$

where S_j is the discontinuity mean spacing and L_j is a characteristic size (best experimental fits are obtained when the burden value is used). The parameter a_s is expressed as a function of the fraction passing value P normalized to 1 ($0.05 \leq P \leq 1$):

$$a_s = 0.4539 + 0.1557 \cdot P^{-1.123} \cdot (1 - P)^{0.1} \quad eq.12$$

The second term of equation 10 is defined as:

$$J_O = a_O \cdot j_{oi} \quad eq.13$$

where j_{oi} is the Lilly's joints orientation index normalized to 1 (Lilly, 1992). The joint orientation term J_O describes the relative difficulty of the blast to break the toe depending on joints orientation with respect to the free face. The joint orientation index j_{oi} varies between four values: 0.25 (horizontal), 0.5 (dipping out of free face), 0.75 (sub-vertical striking normal to the free face), and 1 (dipping into the free face or no visible jointing). The functional form of the constant a_O is expressed in equation 14, in terms of the fraction passing value P . This parameter allows to give to J_O a weight similar to J_S .

$$a_O = 0.05431 + 0.1737 \cdot P^{-1.102} \quad eq.14$$

For this study, P will be given a value of 0.5, which is equivalent to the calculation of the rock factor J_F to predict the median size x_{50} .

Then, the main equation of the xp-frag model, which defines the percentile size x_P , is:

$$\frac{x_P}{L_c} = k \cdot J_F \cdot k_2^h \cdot \left(\frac{\sigma}{q \cdot e}\right)^K \cdot \frac{1}{L_c^{\lambda \cdot K}} \cdot f_t \quad eq.15$$

where:

- k is a fragment shape factor that depends on the percentile P ;
- k_2 is a bench shape factor: it is powered to h that is a function of P ;
- σ is the rock strength (MPa);
- q is the powder factor (kg/m^3);
- e is the heat of explosion (MJ/kg);
- L_c is the characteristic size: it is powered to λ that is a function of P ;
- f_t is a time function of a non-dimensional delay factor.

Further considerations about the factors of the equation 15 are available in Sanchidrián and Ouchterlony (2016). Calculation of Rock mass discontinuity factor J_F for all six scans will be done in paragraph 6.2.

The numerical value of both parameters is directly proportional to the fragments size resulting after the blast, this means that it is inversely proportional to the fragmentation that can be obtained. In fact, the more unfavourable are the conditions, the higher is the values of the parameters involved in the calculation formulae.

3.3.3 Clarification on the models

When carefully analysing the previous two paragraph it is notable that in neither one of the two models the parallel-to-face joints are considered. In fact, the joint plane angle JPA and the Lilly's joints orientation index j_{oi} assume values only for 4 categories of joints: horizontal, dipping out the face, striking perpendicular the face or dipping in the face. However, an eventual set that presents parallel to the face it is not taken in count for the definition of the two rock factors.

There is a reasonable explanation for this lack. Usually, the benches in open pit exploitations have a low number of families of discontinuity: this allows to avoid blasting in a direction that implies the presence of a parallel set. In fact, this configuration is inconvenient to obtain an optimal fragmentation of the rock mass for different reasons. The explosive detonation energy would be dissipated; the gases developed, in fact, would leak out from the rock mass through the parallel set (same behaviour of the striking perpendicular sets). Furthermore, those fractures would prevent the propagation of the induced cracks towards the free face, then generating greater blocks size. This problem is schematically presented in Figure 3.17.

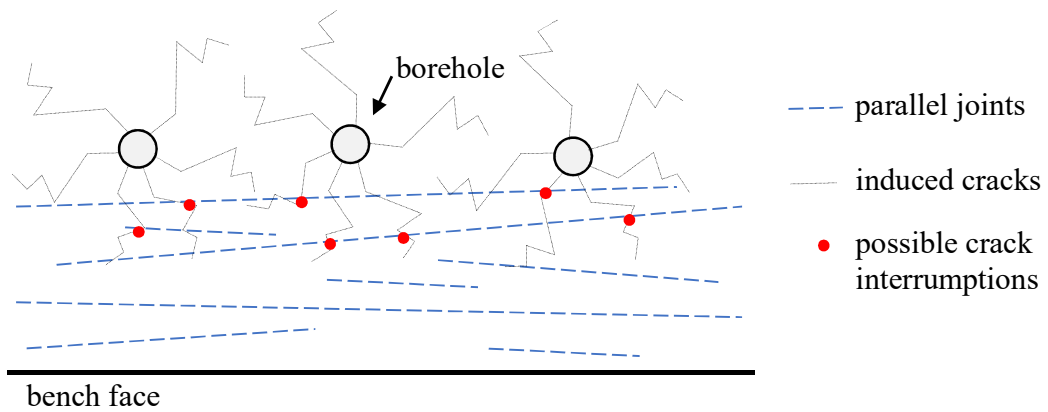


Figure 3.17: schematically representation of the prevention of the propagation of the induced cracks by the presence of parallel-to-face joints

Moreover, the probability of the presence of a set of joints parallel to the free face is relatively low, and this is a further reason why models do not consider it.

As will be explained in this study, the investigated area presents at least 3 different sets of discontinuities, so orientating the blast to avoid this problem is quite difficult. One of the resulting sets (the subvertical in South-West direction one) is unfortunately right parallel to the free face, so it is necessary to introduce a calibrated value for the joint plane angle JPA and the Lilly's joints orientation index j_{oi} .

In particular, for this set, the same parameter values used for “dipping into” sets are assumed because this case represents a similar adverse condition. Then, a value of 40 was assigned to the JPA parameter and a value of 1 to the j_{oi} .

3.3.4 Stereographic projections

In general, a stereographic projection allows to represent the surface of a sphere on a plane. When the sense of the vector is not relevant, as in this study, it is necessary to consider only the inferior hemisphere.

It is possible to use two main different projections:

- *Wulff* projection: the points belonging to the inferior hemisphere are projected on the horizontal plane (passing through the centre of the sphere) using the superior pole (zenith) of the sphere as projection pole. The Wulff diagram introduces a sensible areal distortion, then density conditions could be distorted and the statistical analysis of data prevented. On

the other hand, it is an equiangular representation, so it is mainly used to represent poles because keeps angles undistorted.

- *Schmidt* projection (or *Lambert* projection): to avoid distortion of the previous case, this second diagram is often used to represent poles density. In fact, in this case, the distance between the point and the centre of the circle is modified to make equiareal the representation.

Then, two different nets can be applied to represent planes or poles. The *equatorial net* consists in “great circles” and “small circles” which present the planes dip angle as 90° at the centre and 0° at the external circumference. The *polar net*, instead, consists in radial axes and coaxial circles which present the poles dip angle as 0° at the centre and 90° at the external circumference.

The four possible combinations are presented in Figure 3.18.

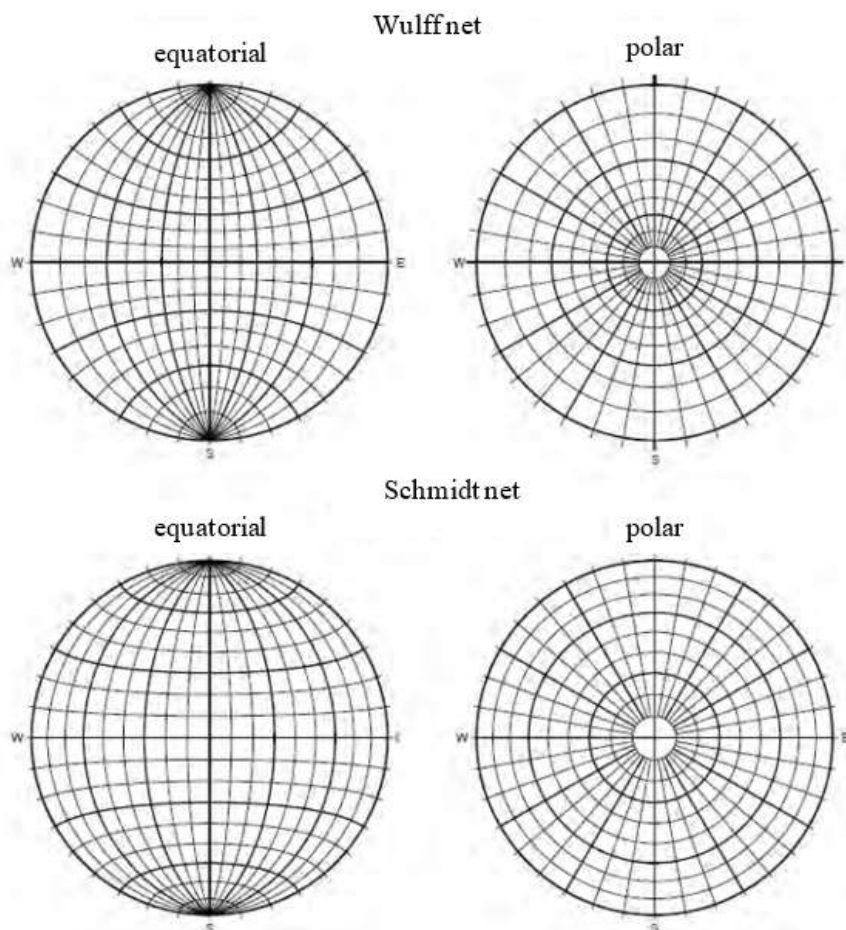


Figure 3.18: four types of stereographic projection

In this study, the *Wulff* projection and the *polar* net are adopted to represent poles with no angular distortion. On the other hand, the *Schmidt* projection and the *equatorial* net is used to represent poles density with no areal distortion.

4. Methods

The face data acquisition was executed with two techniques of remote sensing with completely different procedures and principles. The laser scanning one provides to collect information about a very high amount of points during an approximately 30 minutes surveying, while the photogrammetry procedure is consistently faster. On the other hand, the first method requires a relatively short processing time, while the second imply the spending of different hours of off-site analysis by the operator. This main difference is due to the nature of the post-processing procedure. A *semi-automatic* analysis is adopted, on the laser scanning data, by the Discontinuity Set Extractor software. Instead, a *manual mapping* of the discontinuities is executed, on the photogrammetry data, by the operator.

Both methods will be described in detail in paragraphs 4.1 and 4.2.

4.1 LiDAR scanning

The 3D laser scanning technique of *Light Detection And Ranging* (LiDAR) is based on the time of flight between the laser source (equipment) and the target (in this case a free face). LiDAR relies on a sensor that measures the time spent by the laser pulse to be reflected at the source, and then analyses the wavelengths collected. This technology gives a useful 3D model of the target as output, and for this reason it could be applied in a lot of fields, such as monitoring, topography, forensics and cultural heritage documentation. The combination of laser scans with digital images taken from the same location allows the creation of realistic models in a very short time. Leica Scanstation C10 (in Figure 4.19) can scan and take images at the same time, and to each point of the 3D cloud detected the RGB colour of the corresponding image pixel is given. However, no images were collected in this work.

Nowadays there is an increasing trend in using this tool for assessment of geotechnical conditions of the rock mass. In mining, this technique is mainly used to calculate volumes of ore deposits, scanning periodically muckpiles. In this study instead, laser scanning is used for the detection of fractures, planes and discontinuities families of a rock free face, for its geological characterization. In particular, it is possible to gather a lot of data about discontinuities: orientation, spacing, RQD, and persistence.



Figure 4.19: positioning of the laser scanner during the training on-site in El Aljibe quarry

4.1.1 Equipment

The equipment used for the measurements is a Leica Scanstation C10, that includes a unique portable series of instruments: laser, video camera, data storage and a touch display to control the operations. Thanks to the Smart X-Mirror™ design, the platform can do a high accuracy and long range scanning. This component also allows to spin and oscillate automatically the mirror, a fundamental part for the laser direction. Furthermore, this design guarantees the alignment of the video camera to the laser, to achieve a better targeting and mapping of scans and to let the user conduct full-dome scans in a few minutes (the detection speed ensure collect 50.000 points per second). The covered field of view (FoV) is $360^{\circ} \times 270^{\circ}$, the shadow cone is due to the presence of the instrument and the tripod, like Figure 4.20 shows.

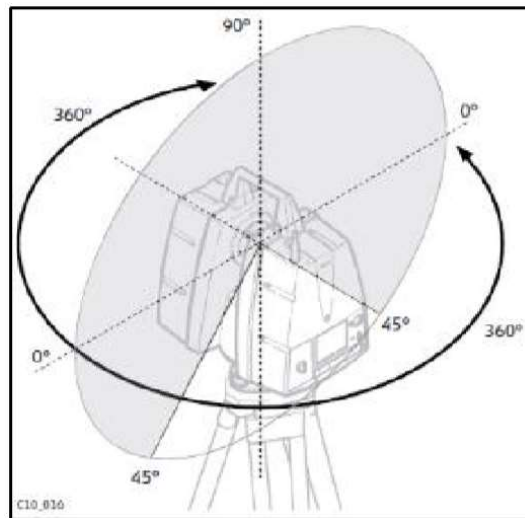


Figure 4.20: scanstation field of view

The laser beam can reach targets at 300 m distance and clearly, the nearest the target, the higher the accuracy.

The instrument includes different components, shown in Figure 4.21; the overall system is designed to be user-friendly and fast to install, also under adverse conditions. Nevertheless, a previous off-site training is needed to understand and learn all the installation and use procedures. Relatively with the figure, the components are the following:

- a. Scanstation C10;
- b. Laptop, not supplied with system (not necessary);
- c. Ethernet cable (not necessary);
- d. Internal batteries;
- e. AC power adapter;
- f. Power cable;
- g. AC power supply for charging station;
- h. Charging station and battery pack;
- i. Tribrach;
- j. Tripod;
- k. Transport container for Scanstation C10;
- l. Alternative transport container for Scanstation C10.

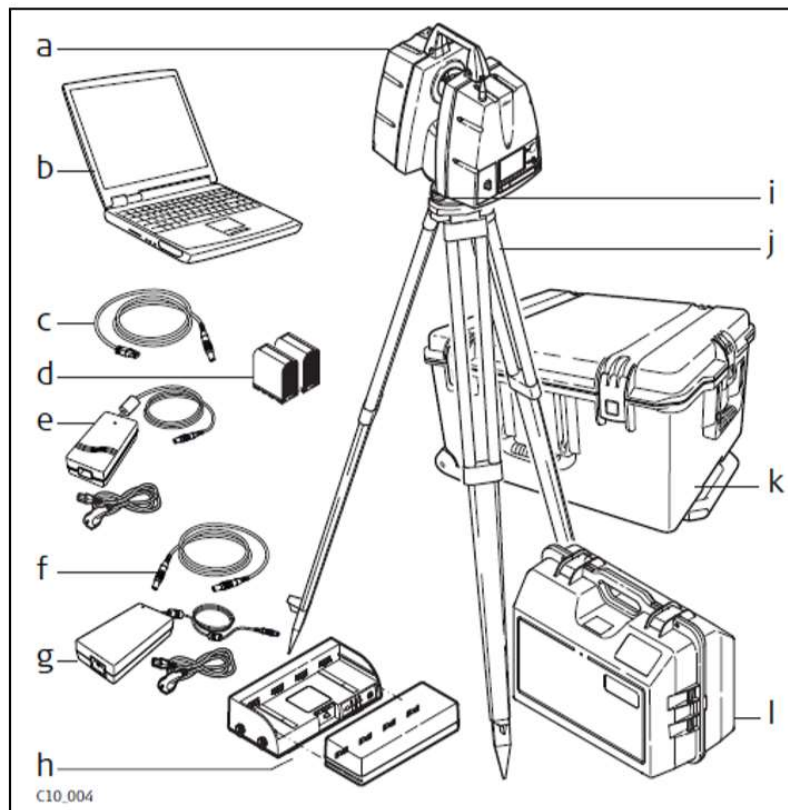


Figure 4.21: scanstation components

It is important to check the charge status of the batteries before use and make sure to have a USB unit to store outputs at the end of the measurements. The overall system is quite heavy, so it is preferable to bring it as near as possible to the point of measure on a van.

Besides these, a sufficient number of targets (in this study 6 targets were positioned on the free face scanned) and a total station to reference all objects (scan station and targets) to a global reference system (GPS) are also needed. Targets consist in 6 red disks with 20 cm diameter; 3 of them are located near the crest and 3 close to the bottom of the free face. Those markers are recognizable in the 3D cloud of points of the digital model enabling the referencing to the global system (GPS) or, in case of multiple scans, to one another.

A careful collection of coordinate data is of great importance, since all measurements would be useless if it is impossible to reference the model correctly.

4.1.2 Principles

The electromagnetic radiation used in laser scanning has a wavelength between 500 and 1,700 nm (Jaboyedoff et al., 2009): this range ensures a proper scan of the target, as this can be very different in relation to the specific application (rocks, rain, aerosol, particulate airborne, non-metallic object, etc.). The beam (or a pulse series) is a directional, coherent, in-phase and highly collimated electromagnetic radiation: this guarantees an extremely fast recording rate and a large amount of 3D information of the terrain.

The target surface reflects waves *via* backscattering; indeed, the instrument cannot detect returning waves if only pure reflection takes place. Terrestrial Laser Scanning (TLS) allows the calculations of distances of points that are several hundreds of metres far (up to 300 metres with Leica Scanstation C10) with a centimetre accuracy. This is possible thanks to the measure of the “time of flight” (Δt) of the laser beam, which travels at the light speed (c). In this way, the software can calculate very easily the distance (d) of every point.

$$2 \cdot d = \Delta t \cdot c \quad eq.16$$

$$d = \frac{\Delta t \cdot c}{2} \quad eq.17$$

Figure 4.22 shows the operational scheme of the platform, which relies on the “time of flight” method. The angle reference ensures positioning of a point in the local coordinate reference system of the scanner. In the scheme, it is observable how the transmitted pulse has a one-pick Gaussian shape, but the reflected one is delayed and distorted. Given the line of sight direction and the attitude of the device (roll, pitch and yaw), the instrument gives to every single point a position (X , Y , Z) in its own local coordinate reference system using simple trigonometric equations. Furthermore, the intensity of the reflected signal is detected, depending on the beam wavelength, type of material, soil moisture and angle of incidence (Jaboyedoff, et al., 2012). The beams impact on an area of variable dimension in function of the distance from the transmitter unit; in fact, the cone of the pulse series opens by moving away, so that the area will be gradually increasing.

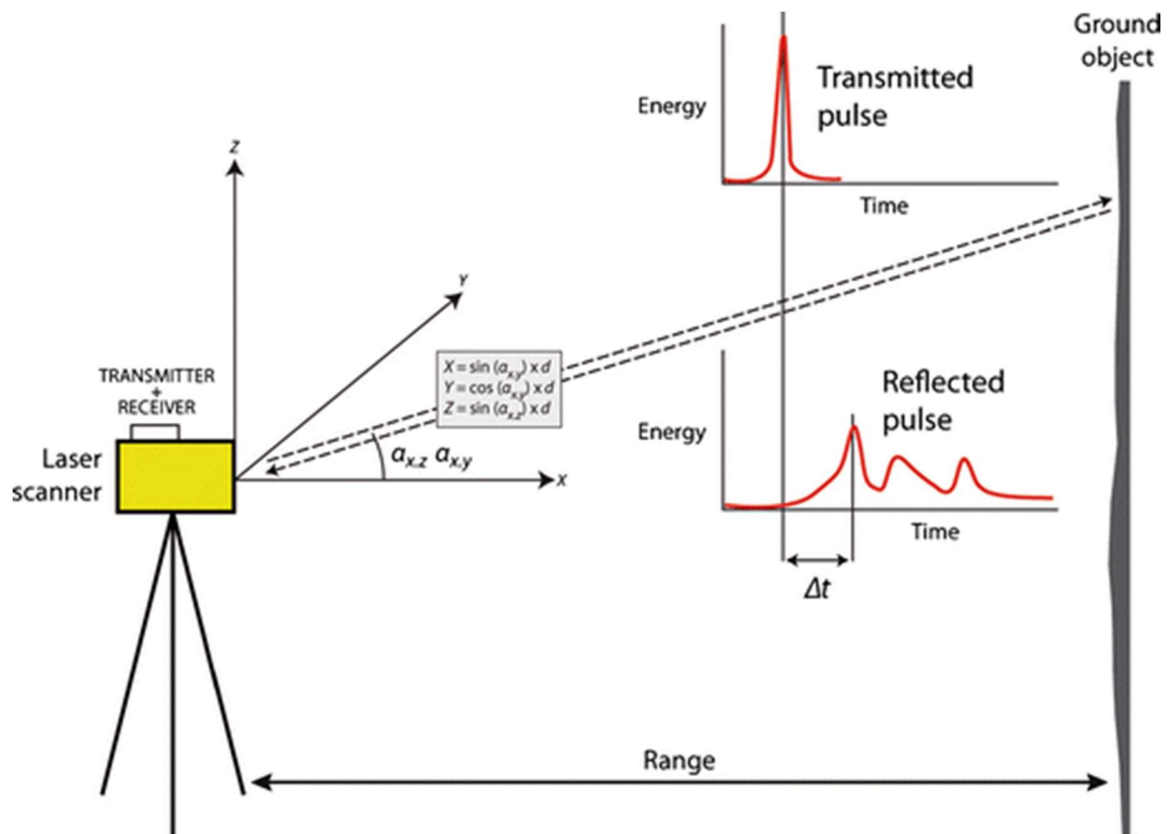


Figure 4.22: operational scheme of the platform (Ravanel, et al., 2014)

Current technologies rely on powerful laser transmitters, high-performance opto-mechanical reflectors and precise receivers, thus generating pulses at very high speed that, in turn, allows the scanner to transmit and receive thousands of pulses per second.

4.1.3 Measurements

First, it was necessary to learn how to use the equipment at three main levels: installation, scanning procedure and data transfer. This training stage was made both off-site and on-site.

Off-site training: definition of user instructions

The instruments were rented from the School of Forestry and Natural Resources (UPM), arrived at university on October 23th, 2018 and were tested indoor. A bookshelf served as the object of the scan, and the guidelines provided in Fernández (2018) were essential during this phase. The main steps that were followed are:

1. Tripod installation: open the tripod legs until the chains attached to them arrive to tension;
2. Install the Scanstation C10 over the tripod: fix it to the tripod by means of the nut;
3. Instrument levelling: focusing on the incorporated bubble, turn the first two foot screws in opposite rotation directions and then third one in order to centre the bubble;
4. Turn-on the scanner: press the *Start* button, then *Main menu* will appear in a few seconds;
5. Create new project: enter the *Manage menu*, then create, name and store a new project;
6. Define station name, origin position and azimuth: enter *New station setup*, name the new station, set origin as $x=0$, $y=0$, $z=0$ (this means the station will be taken as origin) and the azimuth as zero (this means that angles will be calculated starting from the orientation of the scanner when this is turned on);
7. Quick scan: it is first necessary to execute a quick scan with low resolution to define a scan window. To execute the quick scan, enter the *Scan parameters* menu where it is possible to choose the *Field of view* of the scan manually rotating the station and fixing limit horizontal angles. Then choose the *Low resolution* option and start clicking on *Scan* button. This process will take only two or three minutes in which station will move automatically, 3D directing the laser beams;
8. Window selection: at the end of step 7, a rough image of the free face will appear, and through the *Fence* command it is possible to sweep the area of interest in the image (surrounding only the useful free face);
9. Scan: go to the *Scan parameters* menu, in the *Field of view* section the references of the previously selected window will automatically appear. After, set the *Resolution* to *Highest resolution* and start the scan. This process will take approximately twenty minutes and will be stored in the station memory;
10. Data transfer: insert a USB device in its slot and select the *Tools* menu and after *Transfer* section where the project can be selected and transferred;
11. Shut-down the station: click on the 'X' button and then on 'Yes' to confirm to shut down the scanner.

A variation of the scan resolution allows the user to change the horizontal and vertical spacing between collimated points of the free face, as shown in Table 4.5 (Fernández, 2018). Measurements in this study were all executed with *Highest resolution* setting, so 3D models at 100 m distance

would be constructed by clouds of points distant 2 cm from each other. However, measurements are taken at 35 m from the free face, then horizontal and vertical spacing will be approximately 0.007 m.

Table 4.5: resolution setting options

Preset resolution	Horizontal spacing (m)	Vertical spacing (m)	Range (m)
Custom	User defined	User defined	User defined
Low	0.20	0.20	100
Medium	0.10	0.10	100
High	0.05	0.05	100
Highest	0.02	0.02	100

On-site training

On October 23th, 2018 the measuring procedure was tested on-site; this phase was necessary to guarantee effectiveness during real measurements. During the test, both photogrammetry and LiDAR data were collected, allowing also to test different processing software. The laser scan was performed with different resolution setting to choose the more appropriate.

The free face analysed and the positioning of the targets collimated by the total station are shown in Figure 4.23. Measurements were made at a distance of approximately 30 m from the face.



Figure 4.23: analysed free face and positioning of the targets collimated by the total station (blast № 7)

Six blasts measurements

As explained in paragraph 2.2, the blasting campaign consisted in monitoring the conditions before, during and after the 6 programmed blasts. Arnó company reserved a zone of the quarry for the SLIM project investigation (see Figure 2.11). This area was independent from the production area, thus scheduled activities of the quarry were not affected. The 6 free faces that were object of measurements are collected in Figure 4.24.

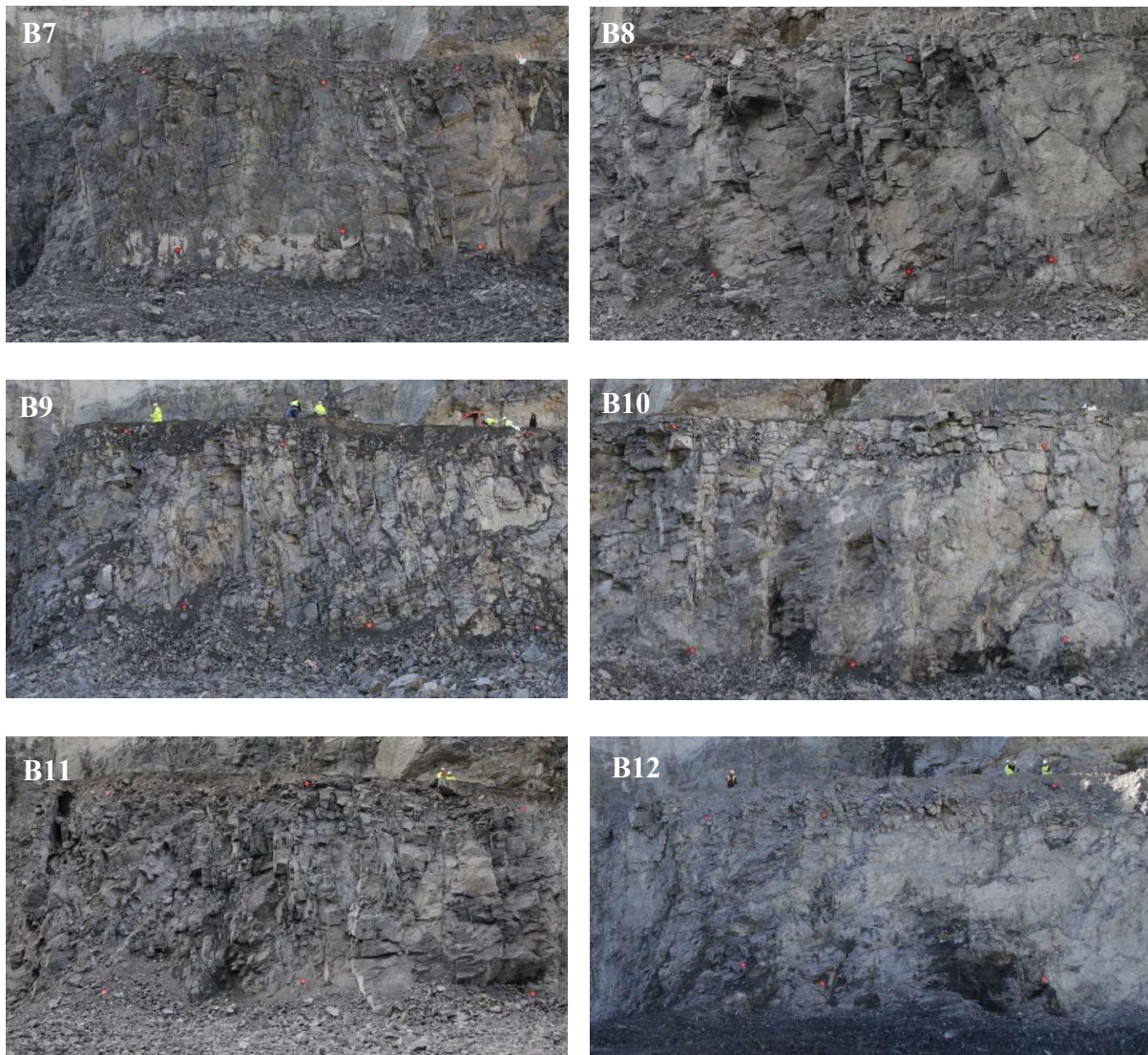


Figure 4.24: six free faces object of measurements

Between each blast, the muckpile at the bench toe (shown in Figure 4.25) was removed to allow the operators to perform the next measurement. The material was charged on dumpers, transported out of the quarry, and stocked next to the processing plant for fragmentation analysis once the 6 blasts were made. An example of muckpile is shown in Figure 4.26; those materials were then scanned to collect information about the fragmentation obtained.



Figure 4.25: blasted material at the toe of the bench (blast № 7)



Figure 4.26: stocked muckpiles for subsequent analysis on fragmentation (blast № 7)

4.1.4 Limitations

The TLS technique has also some not irrelevant limits. The weight of the station amounts to 50 kg (excluding tripod and batteries): this affects its transport through steep or dirty road. Furthermore, the equipment has a high cost, making its use unfeasible for small-medium quarries in Europe. Finally, the relative complex post-processing of data requires several hours and computers able to work with huge amount of data.

There are also others limitations about the positioning of the instrument: often the survey site is constituted by inaccessible areas that complicate the search for a suitable place to install the platform. It is thus necessary to find a compromise among the optimal positioning and the site characteristics. Also, the presence of blocks of rock, yard equipment or vegetation in the path of the laser beam could obstruct the measurements. Positioning targets at the bottom and at the top of the face is quite a dangerous operation because implies passing below and leaning out of the free face, so possible collapse could be a problem.

The instrument precision is inevitably affected by the site unfavourable conditions, for example: bad weather, very brilliant ambient, parallel incident angles, poorly reflecting or very rough surfaces or particulate airborne. Those adverse events can limit the quality of results, even if the resolution of the scan is set at the highest value. Finally, a software which allows the manual analysis of the discontinuities is not provided yet.

4.1.5 Data processing and analysis

Before obtaining results from LiDAR acquired data some pre-processing operations are necessary. Firstly, the raw data are converted from *.bin* to *.txt* extension, then the model can be created, trimmed and referenced. Finally, after the definition of the required parameters, the discontinuities *semi-automatic* analysis can be executed.

Data conversion with Cyclone software

Data collected with Leica Scanstation C10 are transferred to a USB device with a *.bin* extension. To convert the files into *.txt* extension, the licenced software Cyclone (Leica Geosystem Inc., 2012) is used. The codification of the row data prevents the processing with common CAD type software.

The conversion phase is necessary to then import data in CloudCompare (Girardeau-Montaut, 2017) for processing and managing operations. Both software can process points clouds by 3D laser scanner projects.

3D model creation, trimming and referencing with CloudCompare software

The exported scans, with *.txt* extension, are uploaded in CloudCompare, so that a 3D model is generated, consisting in a cloud of approximately 5-10 millions of points, each one made up of three spatial coordinates (x, y, z). Figure 4.27 shows an example of a resulting model.

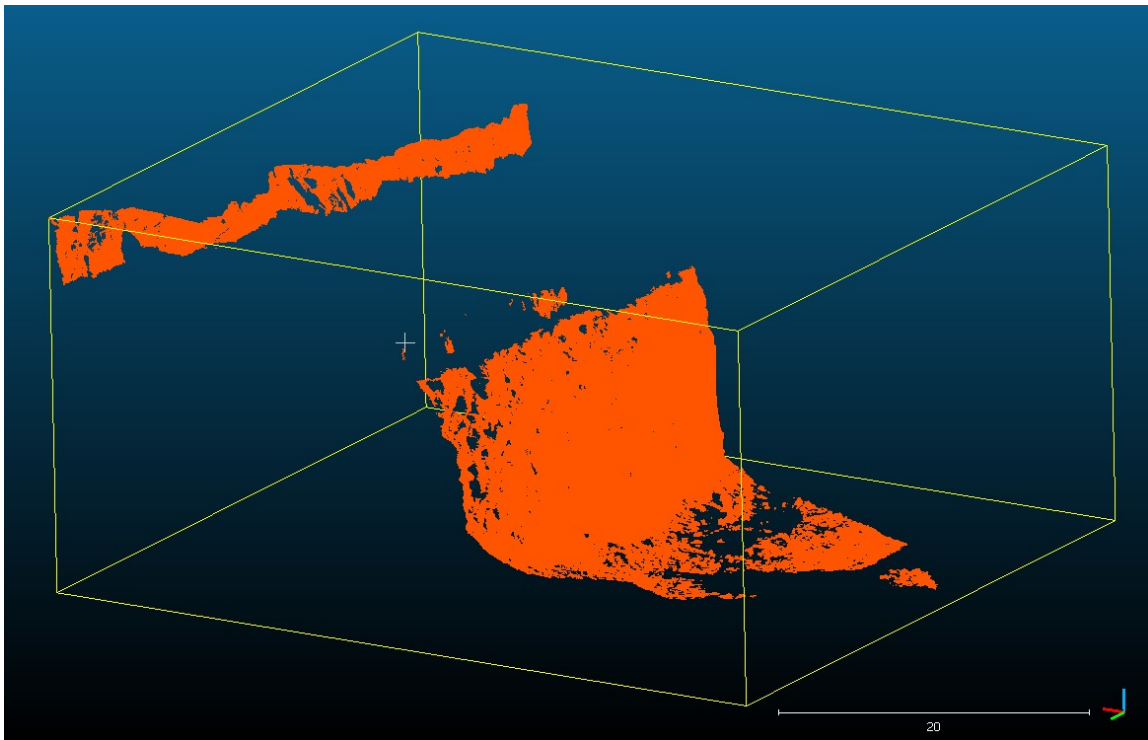


Figure 4.27: raw resulting 3D-cloud model by CloudCompare software (non referenced)

Furthermore, trimming option allows to select and eliminate the undesired or incorrect points. In fact, even though the scan window being carefully chosen, as explained in paragraph 4.1.3, inevitably some points external to the face or some particulate airborne flying between the scan station and the face were collected. An example of trimmed model is shown in Figure 4.28.

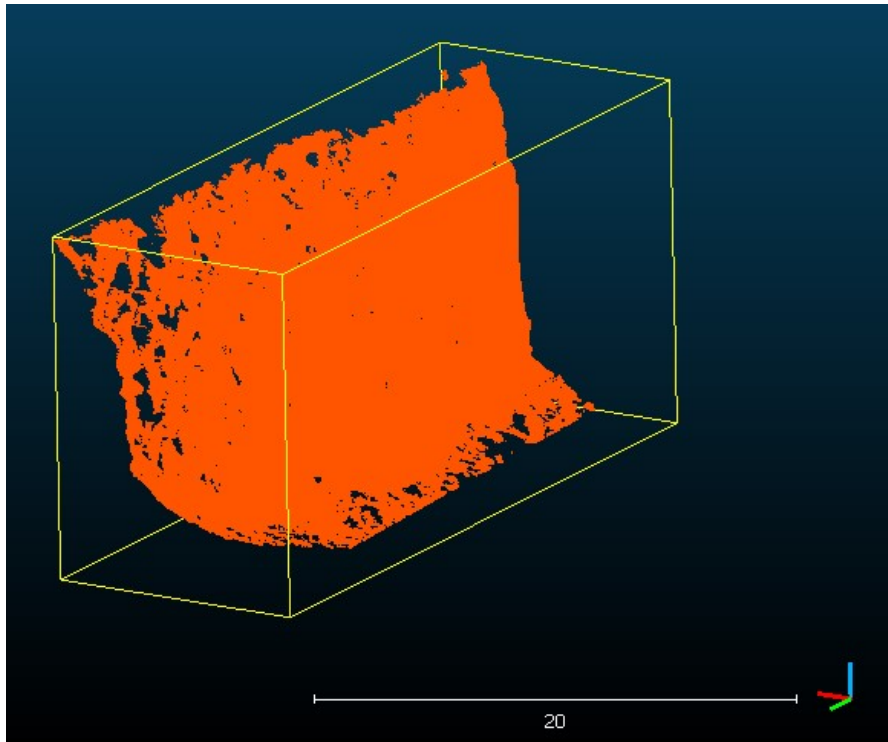


Figure 4.28: trimmed model; all useless points are removed

Then it is important to limit the resolution of the points cloud because a too high density of points can slow processing or even saturate the following analysing phases performed by the Discontinuity Set Extractor (DSE) software (A. Riquelme, 2015). For this reason, a subsampling tool was chosen as a solution to reduce the number of point of the cloud. A minimum distance spacing between points was varied until reducing the points number to approximately 500,000. This operation does not particularly affect the consistency of sampling and details, as explained in the following. Table 4.6 collects the original and final number of points of the models for each blast. The final minimum spacing varies between 0.22 and 0.25 m.

Table 4.6: original and final number of point for each blast

	Blast 7	Blast 8	Blast 9	Blast 10	Blast 11	Blast 12
Original number of points	9,341,282	7,375,710	4,950,281	6,488,080	8,434,778	4,068,972
Defined min. spacing for subsampling (m)	0.025	0.025	0.025	0.022	0.022	0.025
Final number of points	410,886	641,832	454,233	688,241	575,175	435,796

Finally, each model was geo-referenced to ETRS 89 UTM coordinate system. For this, 6 targets (same used for photogrammetry technique) were placed on the free face and surveyed with a total station to give them absolute coordinates. A Quarryman Laser System (QLS) was used for geometrical measurements; the typical accuracy of the instrument in distance is 10 cm and in the vertical and horizontal angles is 0.02° . For 3D model rotation and translation at least four targets were necessary, but all of them were used to reduce the error. Table B.22 (Appendix B) lists used coordinates for each control point of each blast. New absolute coordinates were given to the 6 picked points, that originally have the relative coordinates of the scanstation (see Figure 4.23). Rotation and translation matrixes were automatically generated by the software and so the 3D model was referenced. An example for blast № 12 is shown in Figure 4.29.

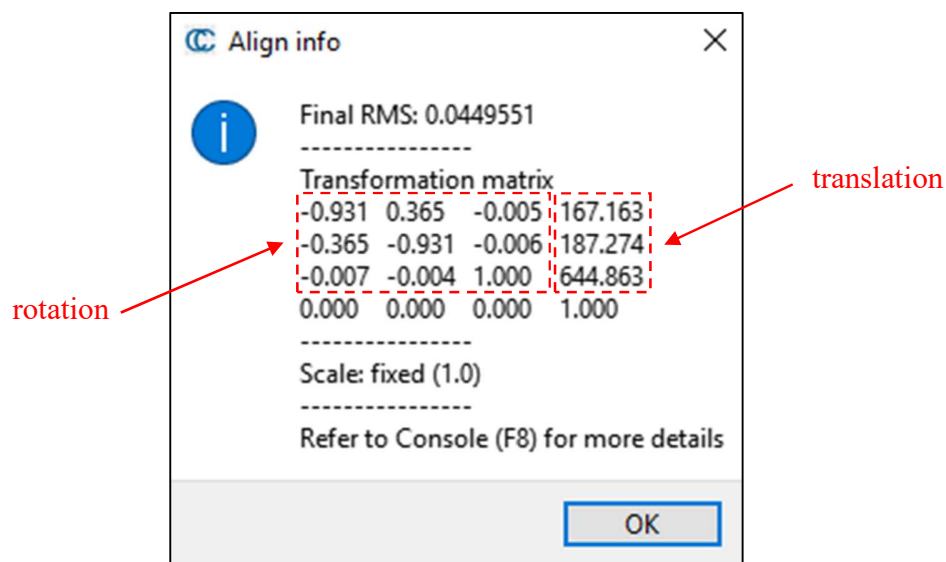


Figure 4.29: rotation/translation matrix generated automatically by the software for blast № 12

As notable in figure, the 4x4 matrix is the product of two matrixes: a rotation and a translation one; the relative factors are highlighted in red. The window of the CloudCompare software allows also to view the *root mean square* deviation (RMSD) resulting from the transformation that, in this case, is 0.045 m.

The 6 picked points to whom new absolute coordinates to rotate and translate the model are assigned are shown in Figure 4.30.

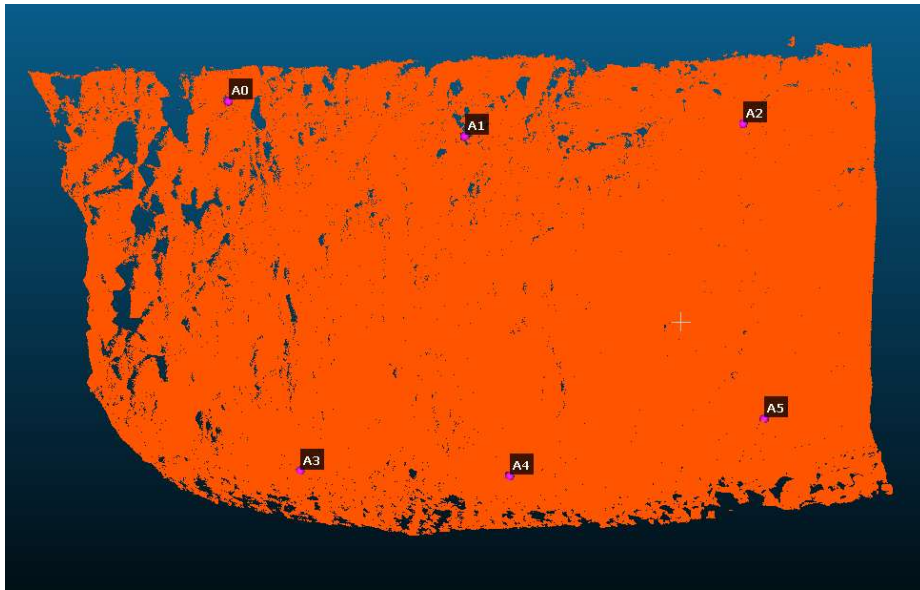


Figure 4.30: position of the six picked points to which are assigned new absolute coordinates

Giving all 6 scans absolute coordinates allows visualizing at the same time, appreciating relative position of one face to others, like Figure 4.31 shows.

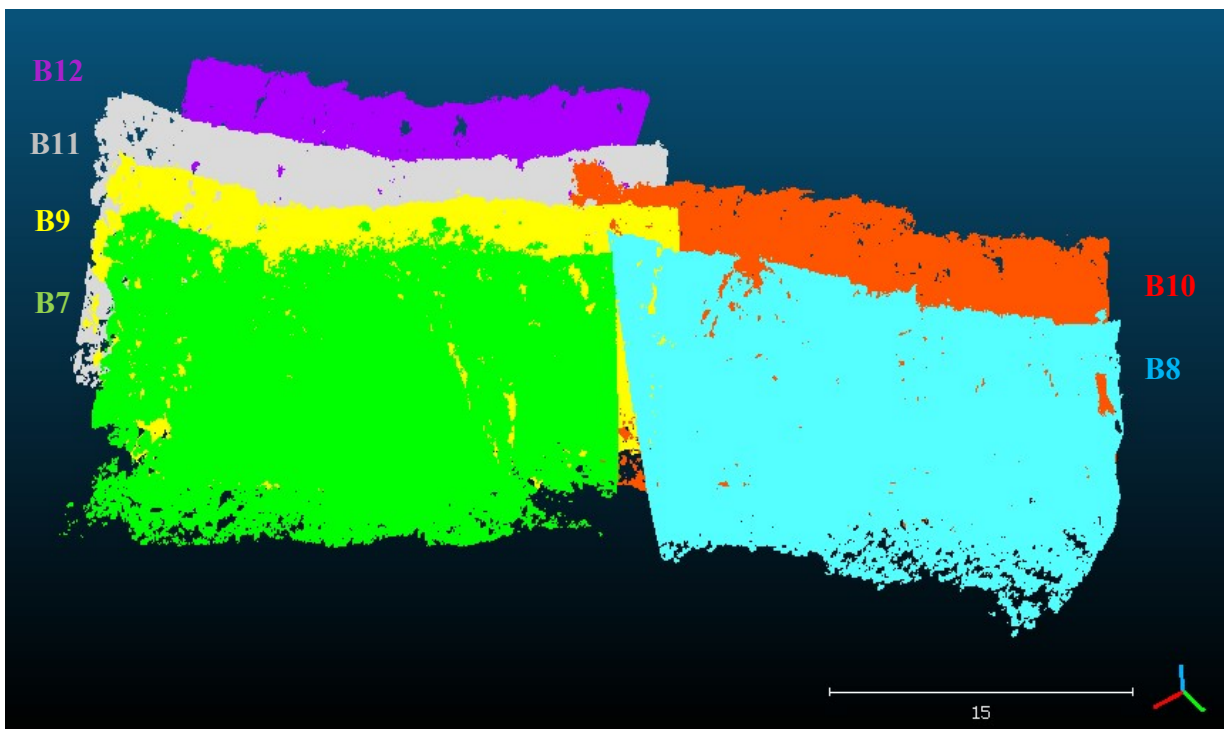


Figure 4.31: relative position of one face to others

Discontinuities detection with DSE software

The DSE (Discontinuity Set Extractor) software is used to detect structural discontinuities. It is an open source software that can process output data from different instruments, such as laser scanner and 3D digitizer. After importing the 3D points clouds, the software, based on Matlab functions, performs a density based analysis of the normal vector deviation. After a semi-automatic processing, DSE software can identify different structure sets and assign to each one the points of the cloud belonging to it (Buyer, et al., 2017).

Riquelme programmed this software to extract discontinuities from a rock mass, identifying and grouping together the point members of the set. He resumed the analysis methodology in the steps shown in Table 4.7 (Riquelme, et al., 2014).

Table 4.7: analysis procedure of the DSE software

Local curvature calculation	I. nearest neighbour searching
	II. coplanarity test
	III. plane adjustment, calculation of the normal vector
Statistical analysis of the plane poles	I. density estimation
	II. semi-automatic set identification
Cluster analysis	I. clustering
	II. plane generation
	III. error fitting test (tolerance)

Semi-automatic analysis means that the software requires the choice of different calibrated parameters values and specific operations options by the operator, to explain its significance the whole procedure of the DSE software is presented:

1. Local curvature calculation

- This operation consists in the search of the nearest neighbour of every point of the raw data in order to create a set, then for each point the discontinuity orientation is determined. Firstly, a *K-nearest neighbour* is defined (*knn*) as a fixed number. In this study, due to the high resolution acquisition, it was necessary to take a high number of neighbours (*knn*=300).

- Later, a coplanarity test was executed to verify whether the points of the sets were coplanar to their nearest neighbour. For this operation it is necessary to define a *tolerance parameter* (η_{max}) that represents the maximum allowable deviation in a subset of points: by this way only reasonable planes are taken in consideration. To represent the data properly a value of 20% was given to η_{max} .
- Finally, a best-fit plane adjustment was executed and then the normal vector was calculated, this process is made for all found subsets.

2. Statistically analysis of the plane

- Different discontinuity sets are individuated within the whole rock mass, then orientation of the principal ones is determined. Projecting the planes poles on a stereographic representation allows calculating their density in each region, then the local maximum is defined. In this phase it is important to control two parameters for de definition of the local maximum: the *cone filter angle* and the *max. poles filter*. The former is the angle between the associated normal vector and the assigned principal plane normal vector. The latter, instead, defines the maximum number of sets to find.
- Now, the software recognizes points belonging to the same discontinuity set (semi-automatic identification) and is able to assign them to the closest principal family.

3. Cluster analysis

- The clustering is carried out to group different subsets into the same cluster and, to do this, a density-based algorithm is used. The recommended value of 1.5 is given to the *standard deviation parameter* (*k sigmas*), which discriminates the merging of two clusters . The *point per cluster parameter*, instead, allows excluding planes constituted by a number of points smaller than the *ppc* value. Changing this parameter can be useful in order to obtain a reasonable normal spacing value (view paragraph 5.1).
- The points that belongs to the same discontinuity plane are localized. A discontinuity plane is a group of points from the same discontinuity set that correspond to a planar

surface. Then, the plane equations of the discontinuities are calculated to mathematically define the planes.

- Finally, a check of the quality of the data fitting is done: the error, defined as the point-plane distance, must be minimum.

Even if for the assignation of parameter values were followed the recommendations of Riquelme (2014), some inputs were changed in order to have a best result, according to the characteristics of the scans. For example, the assumed *knn* parameter value (300) is significantly higher with respect to the suggested one (15-30): this is due to the high resolution of the scans analysed. Processing a large number of points with a *knn*=30 results in an excessive number of clusters. In Table 4.8 both recommended and calibrated parameters values are presented.

Table 4.8: recommended and calibrated values of the input parameters

	Parameter	Simbol	Recommended value	Calibrated value
Local curvature	<i>K</i> -nearest neighbor	<i>knn</i>	15-30	300
	Tolerance (%)	η_{max}	20	20
Principal planes calculation	Min. angle between principal poles (°)	<i>angle min v ppal</i>	10	20
	Min. angle between associated vector and pp vector (°)	<i>cone</i>	30	20
Cluster analysis	Standard deviation	<i>k sigma</i>	~1	1.5
	Point per cluster	<i>ppc</i>	100	100

The results of the *semi-automatic* analysis made with DSE software on LiDAR scanning data are presented in paragraph 5.1.

4.2 Photogrammetry

The photogrammetry was executed as a second method to monitor the pre-blast conditions of the free face. This technique bases on measuring distances from photos, by this way can be assigned the relative position to every point of the framed surface. In this study, the aim of photogrammetry data acquisition is to create a 3D digital model of the bench starting from more images taken from different positions. In Figure 4.32 is shown as the operator frames the free face where six red target are positioned to allow a later geo-referencing of the resulting points cloud. From this model will be possible to characterize the rock mass by a manual mapping of the joints structure. To perform this analysis, the ShapeMetriX 3D software (3GSM, 2010) was used.

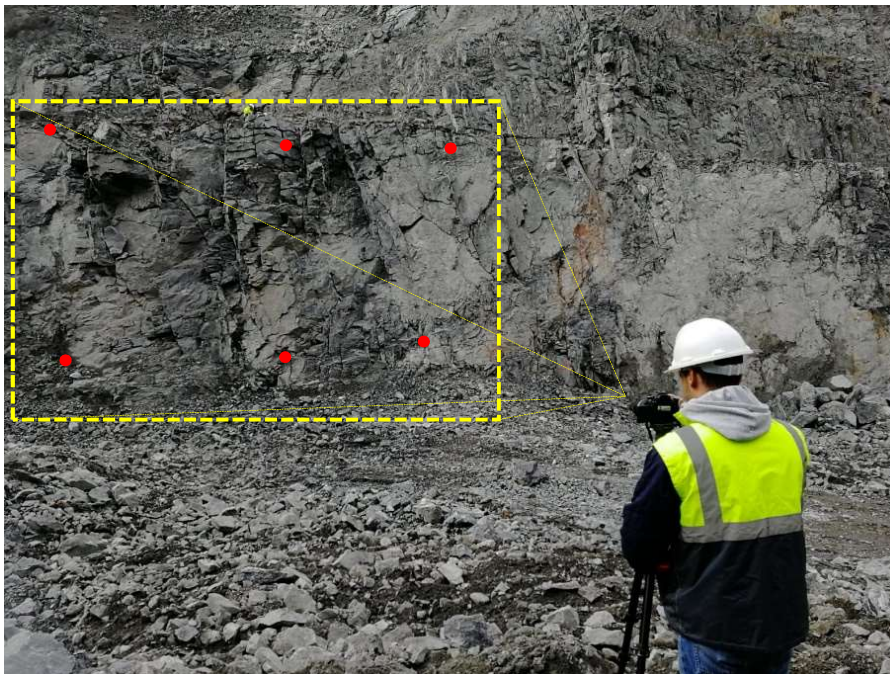


Figure 4.32: configuration for photogrammetry data acquisition; the operator frames the free face (yellow) where the six targets (red) were positioned to allow geo-referencing the resulting 3D model

This methodology is used more than the LiDAR one, then, it is considered as more reliable. The results from photogrammetry (in paragraph 5.2) were obtained after the ones from the laser scanning to avoid to influence the operator's decisions during the manual mapping phase.

4.2.1 Equipment

The needed equipment for the acquisition of data is very simple, this allows to use this technique in almost every site and complete the operation rapidly. For the measurements a digital camera Canon EOS70D was used, equipped with two optical lens (20Mpixel): a Tamron 17-50 mm and a Sigma 10-20 mm. Figure 4.33 shows the instrument with its accessories (USB cable and spare battery) and the targets used for referencing (same used for laser scanning).



Figure 4.33: photogrammetry equipment consists in a Canon EOS70D camera (left) and six targets (right)

Before installing the camera on the tripod, a meter was used to define the position of a “baseline” from which the acquisition is performed. In this study, a 35 m distance from the free face and an axle spacing of 4.5 m between photos was adopted.

4.2.2 Principles

Since the middle of the 20th century, photogrammetry was used in order to obtain reliable measurements from images of different objects. By photographing the environment, for example, it is possible to trace back the real dimensions of its constituent parts.

Nowadays photogrammetry consists in creating a 3D model starting from a stereographic image pair: two pictures of the same object taken from different positions. A software module allows to convert a 2D into a synonymous 3D image; this ensures to collect much more information when off-site processing is executed. In particular, geological, geotechnical and geometric information are the aim of this technique (SMX Manual, 2010). It also possible to merge different models

together in order to cover the entire desired area. Principles of the photogrammetry are schematized in Figure 4.34.

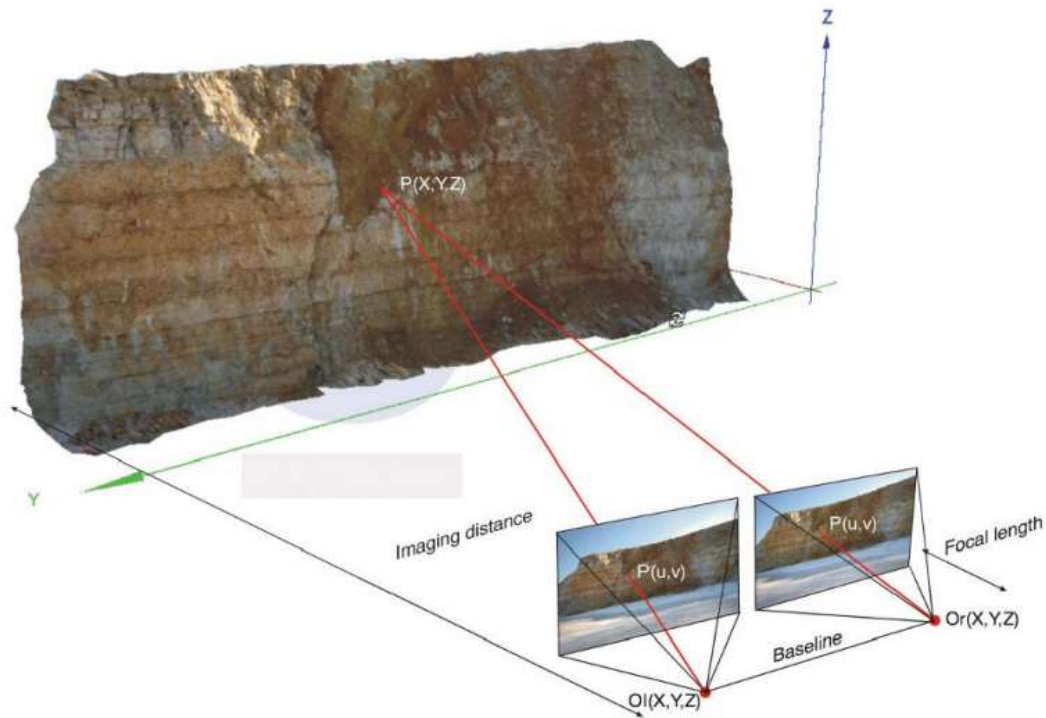


Figure 4.34: scheme of photogrammetry acquisition, the pair of photo is taken on an imaginary baseline at a precise distance from the face (UShapeMetriX3D User Manual, 2010)

4.2.3 Measurements

On-site training: user instruction

On 23th, October 2018 photogrammetry procedure was tested together with laser scanner and other equipment. During the test was studied a scheme to reproduce for the measurement of every blast. Instruction in ShapeMetriX manual were followed to position the camera (SMX Manual, 2010); the values of the imaging distance D from the free face and the baseline on which the photos are taken are listed in Table 4.9. The range of the axel spacing S (from $D/8$ to $D/5$) between each photo taken on that baseline is also expressed in function of D .

Table 4.9: ranges of the axle spacing S in function of the distance from the face D

Distance from the face D (m)	Axle spacing between photos S (m)	
	$D/8$	$D/5$
15	1.88	3.00
20	2.50	4.00
25	3.13	5.00
30	3.75	6.00
35	4.38	7.00
40	5.00	8.00

In this study, the measurements were executed at a distance of 35 m from the free face, so an axle spacing of 4,5 m was adopted. Being the face from 20 to 25 m long, every series consists of a number of photos from 4 to 6. A schematic representation is shown in Figure 4.35.

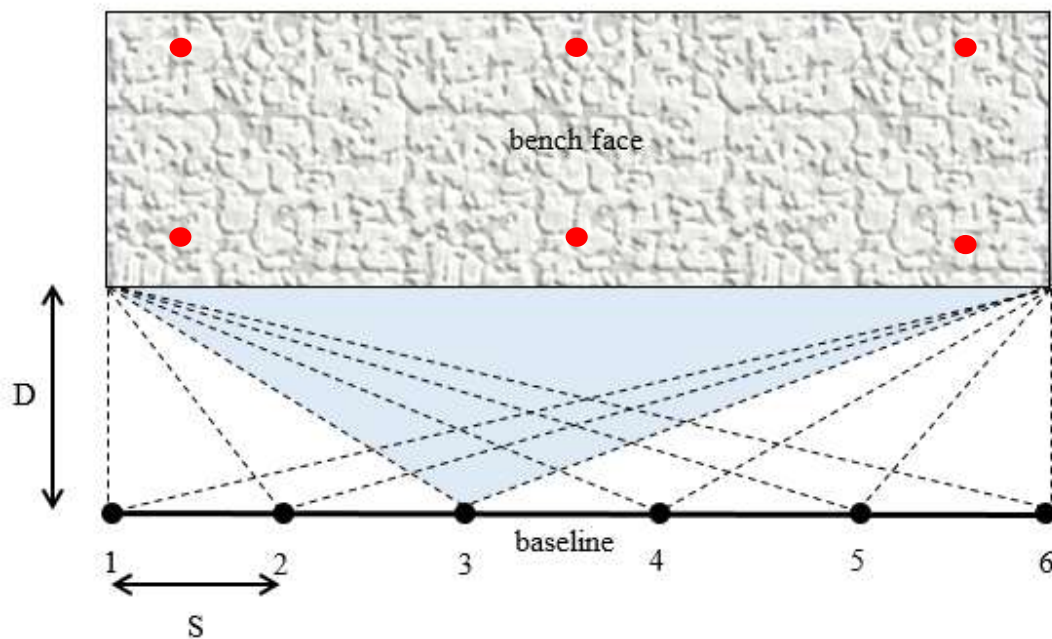


Figure 4.35: final configuration for photogrammetry acquisition of the six photos; in red are represented the six targets to then reference the model

Image taking is important to respect few simple precautions:

- Before starting acquisition is necessary to auto-adjust the focus of the lens with the automatic setting, then it is switched to the manual one till the end of measurement;

- The zoom has to be set up at 17 mm and it is unchanged;
- While taking photos the camera must be more perpendicular to the free face as possible and the face has to occupy one third of the height of the entire image (centrally and horizontally positioned);
- For each position 4 photos are taken, the first including an operator hand indicating the number of the points of acquisition and other 3 of the face (only one of them will be really used, but as a precaution is convenient to take more);
- Finally, it is necessary to note if the series of images are taken starting from the left or the right, in this way is possible to deduct the position of all of these.

Six blasts measurements

Being photogrammetry executed just before the laser scanning on the same free faces (shown in Figure 4.24), what explained in paragraph 4.1.3 remains valid also for photogrammetry measurements. This technique was executed basing on instructions provided in Gomes (2017).

4.2.4 Limitations

Positioning targets at the bottom and at the top of the face is quite dangerous because it implies passing below and leaning out of the free face, so possible collapse could be a problem. Due to this risk, the targets cannot be positioned perfectly parallel to the face, so this can be the cause of eventual distortions in the created 3D model.

If object on different planes are present, as large boulders and unloaded material in front of the bench, the quality of the model will be poorer. Also illumination condition could affect the results goodness, in fact, shadows can be misinterpreted by the processing software.

Furthermore, when the face presents relevant irregularities, the final model could be incomplete or distorted in those areas that were not be visible from the acquisition position because of those protuberances.

Finally, the positioning of the tripod on the precise point individuated in the acquisition scheme (explained in the previous paragraph), can be difficult when boulders or muckpiles in front of the face are present.

4.2.5 Data processing and analysis

The ShapeMetriX 3D software allows processing raw data (2D photo) to create a 3D photogrammetric model and then analysing it from a geological and geotechnical point of view. This process is done by different modules of the program:

- *ReconstructionAssistant*: from stereoscopic image pairs generates 3D images;
- *SurfaceTrimmer*: edits a 3D image;
- *ModelMerger*: merges more 3D images in one;
- *Referencer*: georeferences control points (targets);
- *Analyst*: geological and geotechnical parameters.

3D model creation

To create the model is necessary to load a pair of stereographic photos in the *ReconstructionAssistant* module; in particular, two subsequent photos are chosen in the series acquired. If the series consists in 6 images for example, 3 models will be created: the first with the image 1st and 2nd, the second with the 3rd and 4th, the third with the 5th and 6th.

When loading the pair of images, the software needs a user adjustment to manually overlap as best as possible the 6 targets of one photo to the 6 of the other one. However, a remaining error exists. Then, it is necessary to mark with two lines the ends of the free face; in particular, the crest and the toe. As example, the resulting model for blast № 12 is shown in Figure 4.36; only the highlighted area will be useful for the following analysis.

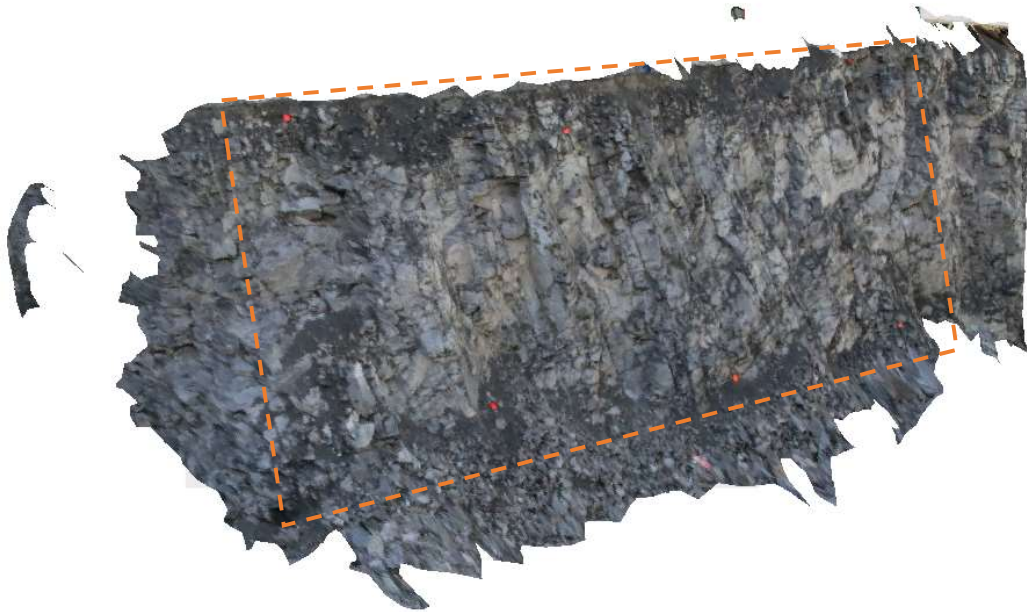


Figure 4.36: original 3D model of the face by ShapeMetriX software (blast № 12)

By the *ModelMerger* module it is also possible to merge two or more different models to increase quality, in this study was chosen to skip this operation because of a distortion problem in the result. However, the possible improvements to achieve were not such relevant and the single model already has a good quality. Then, the operator chooses between the 3 results the one which does not show irregularities or shadows areas. The *ModelMerger* application would be necessary if both photos of the pair do not frame the entirety of the free face.

Trimming and Referencing

At this point of the process, the user can trim the 3D model created by the *SurfaceTrimmer* module. This phase allows to delete useless zones out of the desired free face area (highlighted in Figure 4.36), reducing the number of points constituting the model and thus making the archive smaller.

To reference the models with the *Referencer* module is sufficient to select all six control points and then give them coordinates (X, Y, Z) of the ETRS 89 UTM reference system. The same instrument of LiDAR procedure was used. After assigning position to the reference points, the software will automatically rotate and translate the 3D image. It is then possible to control the standard deviation between the original and the final coordinates of the targets, if its value does not exceed 0,01 m,

procedure can be reasonably considered accepted. As example, the resulting model for blast № 12 is shown in Figure 4.37.



Figure 4.37: trimmed and referenced 3D model of the face by ShapeMetriX software (blast № 12)

Discontinuities detection

Now the model is ready to be geologically and geotechnically analysed by the *Analyst* module. The operator has to manually mark, by a polyline or a plane, all the relevant joints that are visible in the 3D model. Figure 4.38 shows the fracture structure relative to the blast № 9; in this case 163 discontinuities were detected during a three-hour manual analysis. At every joint a family (*structure set*) was assigned, according to its orientation; different colours were given to each set:

- red to the SvSE set (subvertical in South-East direction);
- blue to the SvSW set (subvertical in South-West direction);
- green to the Sh set (subhorizontal).

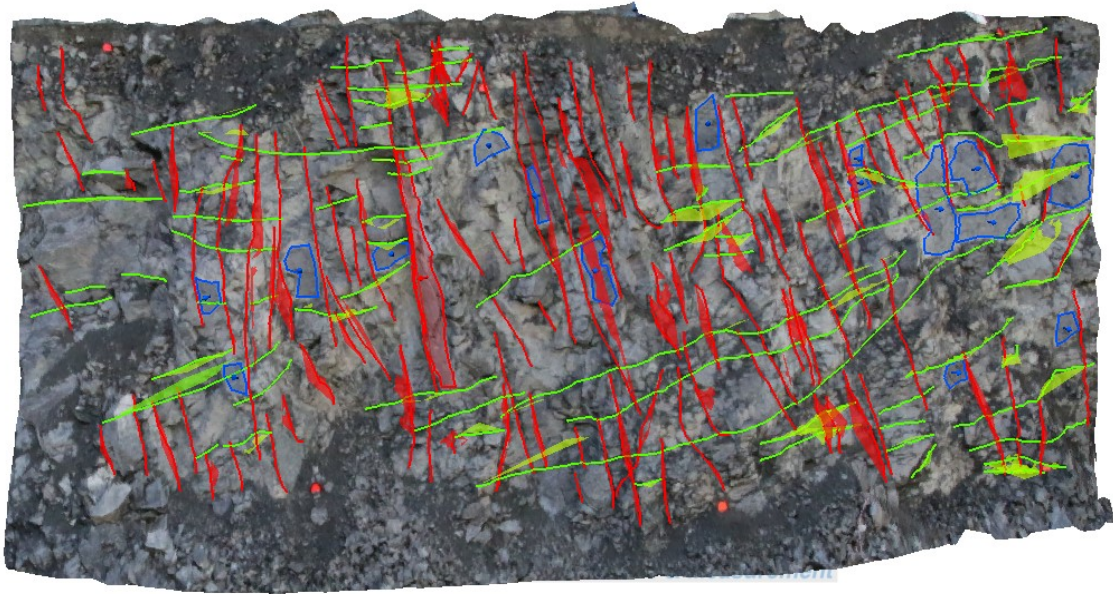


Figure 4.38: manual mapping of the joint sets for blast № 9. Subvertical in South-East direction set in red, subvertical in South-West direction set in blue and subhorizontal set in green

In the figure it is notable as, at each polyline side, the software automatically draws the plane which best fit to the line; for this reason, is important to take care to the curvature of the line while marking.

Then, an automatic clustering is executed by the *clustering menu*; at this point is necessary to choose some parameters:

- Clusters maximum and minimum number: according to previous geological reports of the area a minimum of 2 clusters and a maximum of 3 were assumed; then, for the result plot, a 3 cluster option was selected;
- Number of evaluations: was chosen a 10 iterations algorithm (higher option);
- Membership angle maximum: according to different test and to the experience of 3GSM, the maximum angle allowed between two joints of the same cluster was set up to 35°. Reducing this parameter means a higher number of clusters;
- Confidence: the percentage of confidence was assumed as 95%.

The software algorithm automatically assigns each marked joint/plane to a cluster. This operation is obviously done without considering the previously assigned colour (set) of each discontinuity; therefore, different clusters are created. In Figure 4.39 the automatic cluster assignment for blast

№ 9 is shown: the orientation of the plane associated to each joint allows attributing to different cluster joints that seems to belong to the same one. The discontinuities that do not belongs to any family were given in black.

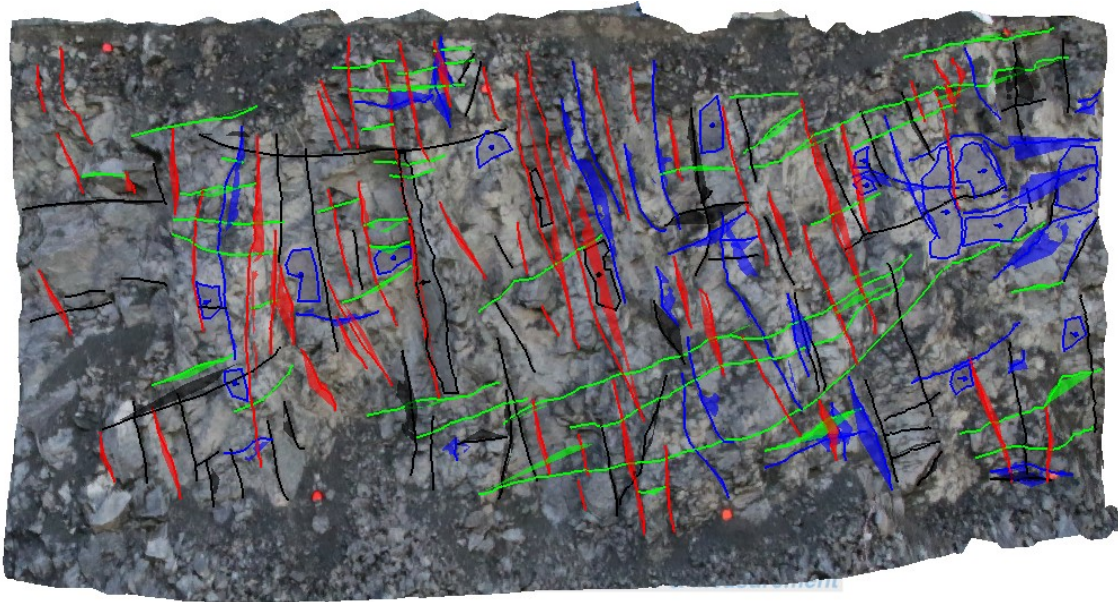


Figure 4.39: automatic cluster assignment for blast № 9. Subvertical in South-East direction set in red, subvertical in South-West direction set in blue, subhorizontal set in green and not assigned joints in black

This procedure was made for each of the six blasts, in Table 4.10 are reported the number of marked joints for each set of each blast.

Table 4.10: number of marked joints for each set of each blast

	BLAST 7	BLAST 8	BLAST 9	BLAST 10	BLAST 11	BLAST 12
Non-assigned	7	12	24	13	11	37
SvSE	32	20	53	26	21	35
Sh	28	36	38	53	25	39
SvSW	24	39	48	42	29	79
Total	91	107	163	134	86	190

Both manual and automatic structures are presented in Appendix C (Figure C.65 and Figure C.66). results from the analysis are reported in paragraph 5.2.

5. Results: geomechanical models of the blasts

The results from both methods consists in the characterization of the main discontinuity sets of the rock mass in terms of orientation (dip direction and dip angle) and normal set spacing. The comparisons were executed researching matches between the sets individuated by the two analysing software using the minimum angular distance criterion. Also the confrontation of the mean normal set spacing was useful to verify the calibration of the input parameters that the two software require.

5.1 LiDAR scanning results

As explained in paragraph 4.1.5, the orientations of the principal plane sets are indicated by the maximum resulting in the poles density plot. In Figure 5.40 the 3D stereographic projection for blast № 7 is shown; in this way the DSE software represent clearly where the most representative poles are. As it is notable, the higher density peak is not considerate as the pole plane of a discontinuity set, but, having a similar orientation of the face plane ($220.6^{\circ}/65.2^{\circ}$), it was attributed to it. In that precise stereographic representation, related to the blast № 7, five poles are individuated (relative to the discontinuity sets J1, J2, J3, J4 and J5).

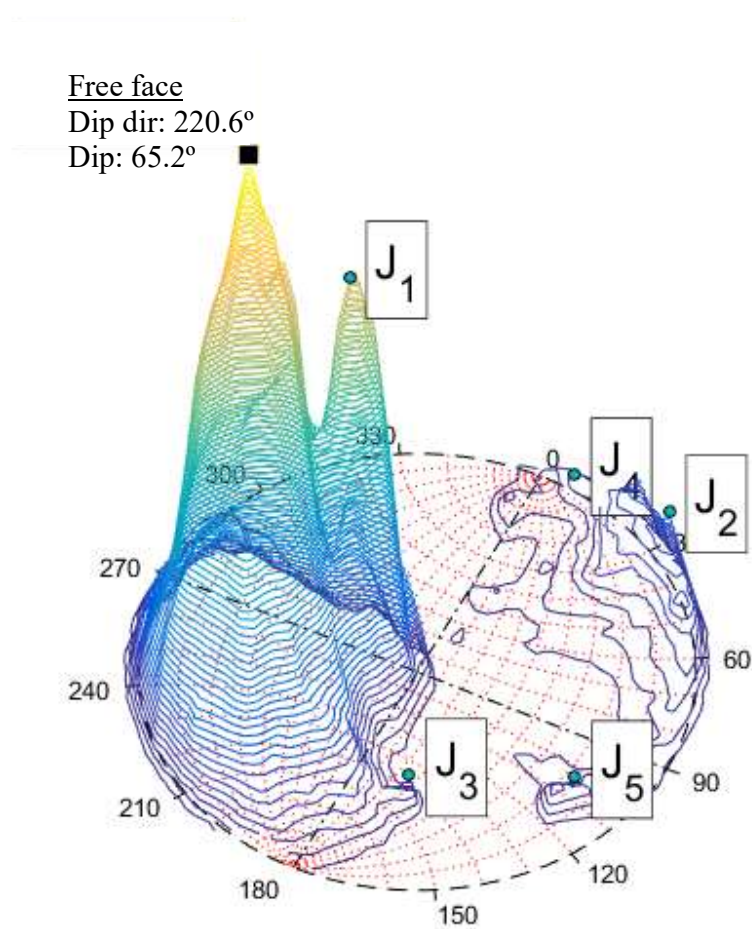


Figure 5.40: 3D stereographic projection for blast No 7

By the *Edit poles* function of DSE software the higher peak is removed, then the pole assignment automatically reassigned the remaining set. The clustered cloud is presented in Figure 5.41, before and after the removing of the cluster relative to the bench face.

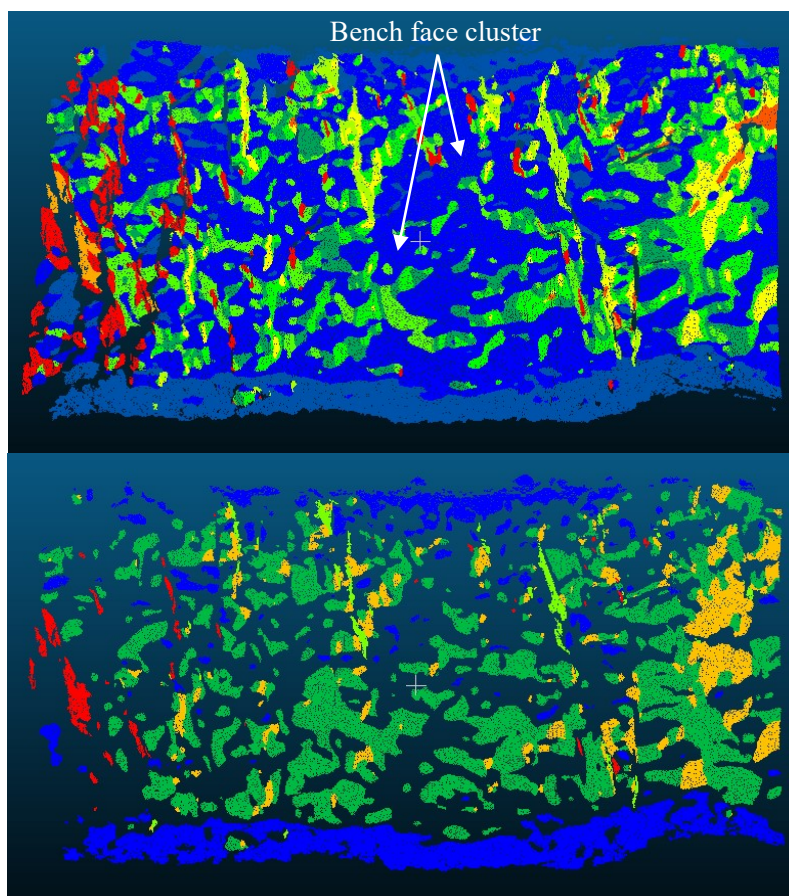


Figure 5.41: clustered cloud before (top) and after (bottom) the removing of the cluster relative to the bench face (light blue cluster)

The software allows the user to eventually discard low density sets or merge two different sets according to geological criteria. Also comparison with photogrammetry results can help in the discrimination of some sets which do not have other feedback. In particular, in paragraph 5.3, the comparison between the two methodologies will allow to combine DSE resulting sets with the ShapeMetriX ones. For example, for blast № 7, J1 will be associated with a subhorizontal set (Sh), J2 and J4 with a subvertical set in South-West direction (SvSW), and J3 and J5 with a subvertical set in South-East direction (SvSE).

Stereographic projections

The stereographic projections are collected in Figure 5.42; in this case a 2D representation of the mean pole assigned to each cluster makes easier to compare one to another. The *Wulff* projection and the *polar* net is adopted to prevent angular distortion. The density plot of each blast are

presented in Figure D.67 of Appendix D. It can be noticed that the main discontinuity sets occurred in more plots approximately in the same zone of the diagram: this is the evidence of a geological structure that repeats in every blast; additional information will be given in the following.

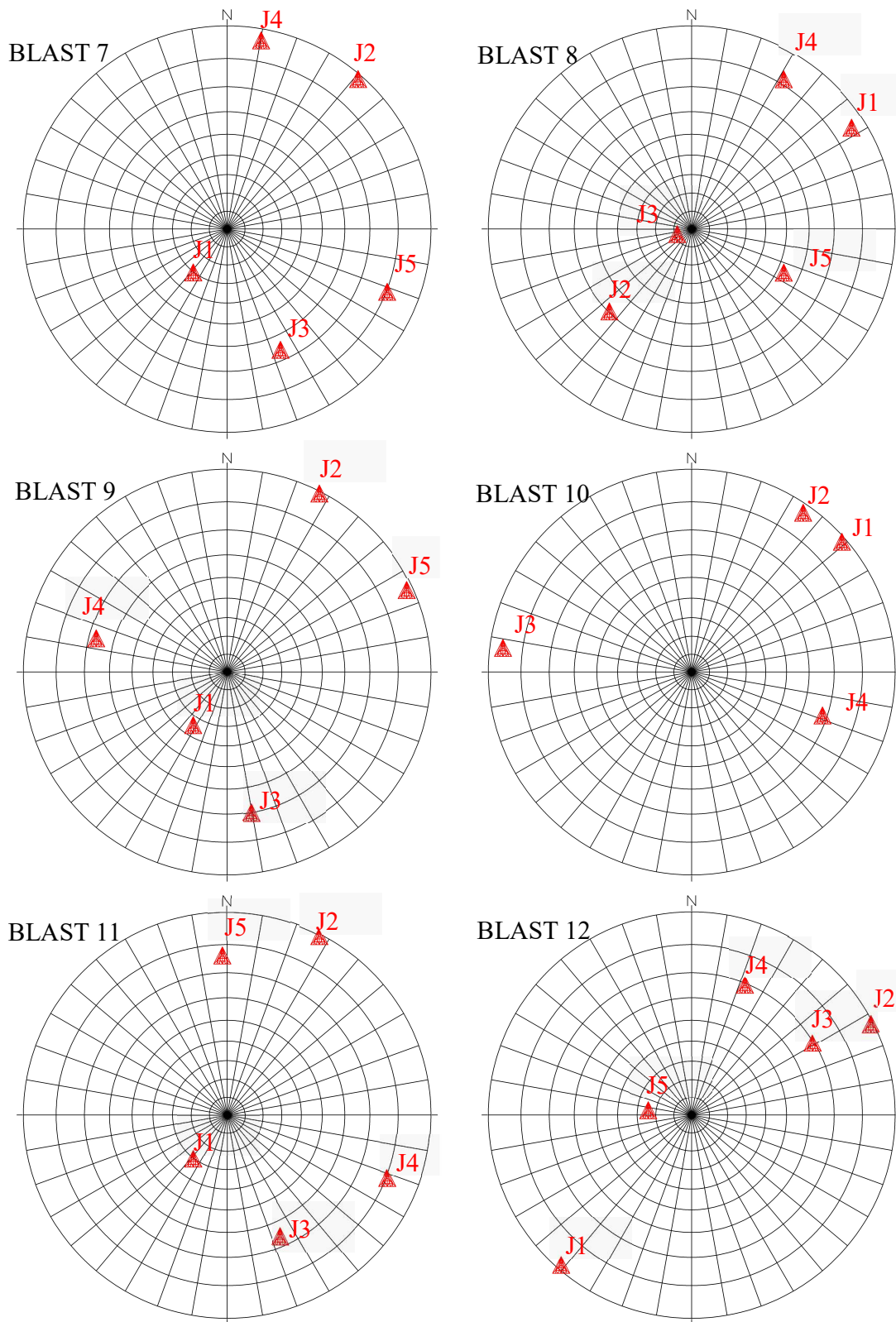


Figure 5.42: stereographic projections of the six blasts from lidar scanning

Discontinuity sets identification

For each discontinuity set the software calculates its orientation (dip direction and dip angle), density of points per area and the number of assigned points (coplanar points) over the total number of points of the model (expressed as percentage). Table 5.11 shows the list of values for each blast.

Table 5.11: orientation, density and percentage of assigned points for each set of each blast

BLAST 7				
	Dip dir (°)	Dip (°)	Density	%
J1	37.93	30.31	24.26	16.00
J2	221.03	88.75	0.45	19.08
J3	336.24	66.00	0.22	1.12
J4	190.17	86.66	0.18	5.72
J5	291.48	80.30	0.18	1.13

BLAST 8				
	Dip dir (°)	Dip (°)	Density	%
J1	237.58	85.89	30.92	26.99
J2	44.97	59.59	18.53	35.10
J3	71.12	8.63	14.29	9.72
J4	211.54	81.70	0.66	18.01
J5	295.39	53.20	0.14	1.16

BLAST 9				
	Dip dir (°)	Dip (°)	Density	%
J1	32.48	34.49	32.05	20.01
J2	207.19	89.40	0.57	18.85
J3	350.22	70.00	0.49	5.56
J4	104.52	67.16	0.32	1.82
J5	245.34	88.20	0.27	8.63

BLAST 10				
	Dip dir (°)	Dip (°)	Density	%
J1	228.96	88.76	0.95	20.96
J2	214.90	87.51	0.87	14.93
J3	97.31	86.19	0.22	3.81
J4	288.42	68.25	0.07	0.83

BLAST 11				
	Dip dir (°)	Dip (°)	Density	%
J1	37.86	30.36	22.62	15.47
J2	207.19	89.42	0.44	17.76
J3	336.24	66.06	0.20	1.18
J4	291.50	80.36	0.17	1.15
J5	178.27	76.32	0.15	1.39

BLAST 12				
	Dip dir (°)	Dip (°)	Density	%
J1	41.07	88.67	21.62	28.50
J2	242.85	89.36	0.23	8.17
J3	239.07	69.45	0.16	0.93
J4	202.20	69.42	0.15	22.38
J5	96.31	24.28	0.11	0.91

The values of *dip dir* and *dip* are needed to define the *joint plane angle* value and the *Lilly's joints orientation index*, essential for the Blastability index and the Rock mass discontinuity factor calculation (view paragraphs 6.1 and 6.2).

Normal set spacing

The DSE *Normal spacing* tool was used to calculate the distance between a joint plane and the subsequent one of the same set (normal set spacing). This distances are measured on a perpendicular direction in relation to one of those two joint planes and, by this way, the minimum distance was collected. This process was made for each cluster of each blast; in Table 5.12 all mean values of the normal set spacing and their relative standard deviation (after “sd”) are collected. Both *full-persistent* and *non-persistent* measurement mode was provided by the software but, nevertheless, the second one was assumed. This decision was taken after the visualization of the free face fractures structure which presents a discontinuous behaviour, and therefore is constituted by non-continuous sets of joints.

Table 5.12: mean values of the normal set spacing and their relative standard deviation

	Blast 7	Blast 8	Blast 9	Blast 10	Blast 11	Blast 12
J1	1.07 sd 0.88	0.84 sd 0,66	0.92 sd 0.74	1.58 sd 1,03	1.05 sd 0.79	0.87 sd 0.74
J2	0.80 sd 0.66	0.71 sd 0.66	1.07 sd 0.88	0.94 sd 0,64	0.85 sd 0.67	0.70 sd 0.53
J3	2.05 sd 1.76	2.08 sd 1.96	1.36 sd 1.10	1.20 sd 0,82	1.87 sd 1.37	2.26 sd 2.88
J4	1.54 sd 1.05	0.67 sd 0.48	2.30 sd 1.51	2.87 sd 1,92	2.60 sd 1.89	2.04 sd 1.99
J5	2.60 sd 2.14	3.31 sd 2.53	2.08 sd 1.38	-	2.02 sd 1.50	0.95 sd 0.07

As explained in paragraph 4.1.5, the *Point per cluster* parameter (*ppc*), used in the discontinuities detection process, can affect the normal spacing values. In fact, increasing the minimum number of point per cluster, every discontinuity set will be constituted by a lower number of clusters, then the normal spacing increases. In this study a value of 100 was assumed for the *ppc* parameter which allows obtaining a reasonable range of normal spacing.

The software provides also the density function plot of the normal spacing for each discontinuity set of each blast; Figure 5.43 shows the one relative to the discontinuity set J1 for the blast № 12.

It is notable as, for non-persistent joints spacing, the variation is much higher than for full-persistent joints spacing.

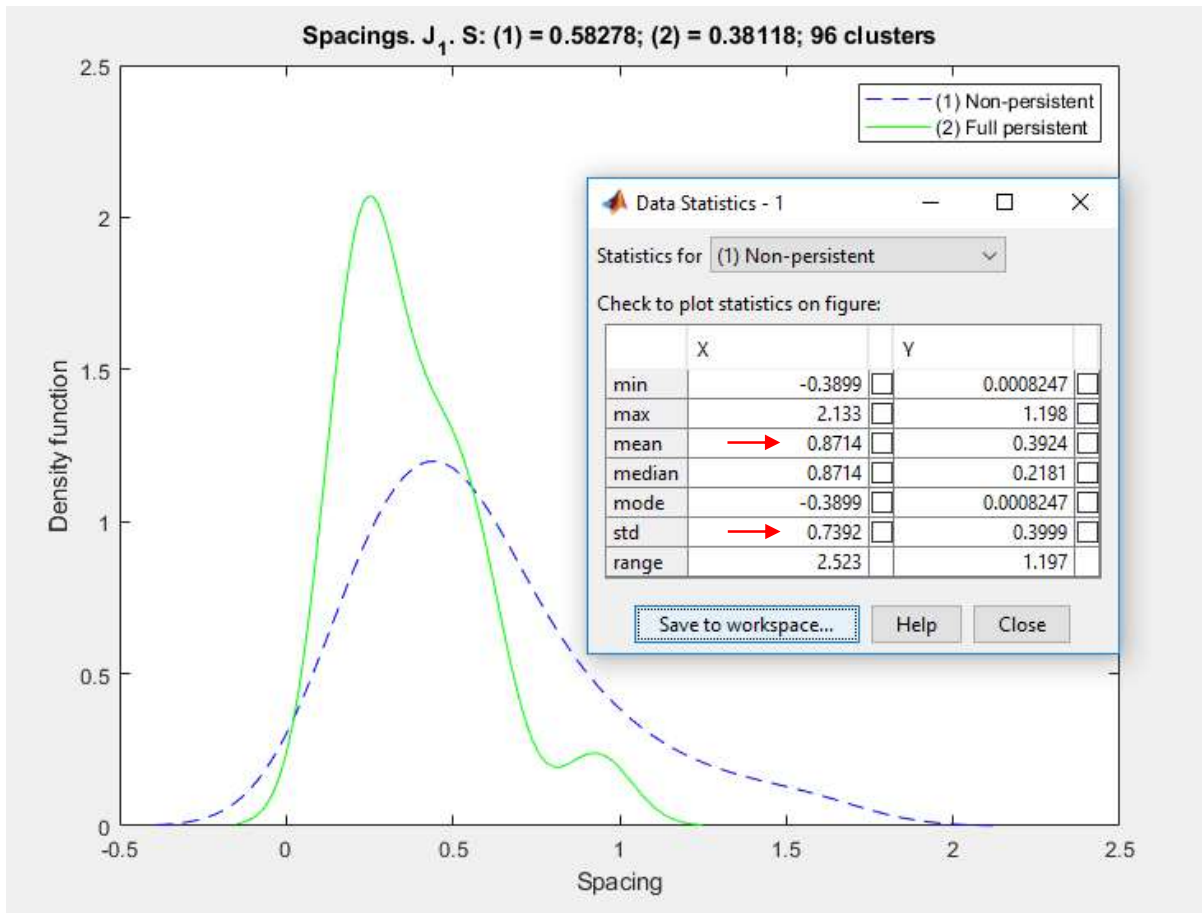


Figure 5.43: density function plot of the normal spacing relative to the discontinuity set J_1 for the blast № 12

5.2 Photogrammetry results

Stereographic projections resulting from manual and automatic clustering

As explained in paragraph 4.2.5, both manual and automatic clustering is executed. In the first instance, the stereographic representation allows to compare one to the other. Then, the numerical

data found about orientations of each set and the spacing analysis will constitute a precise comparison.

Figure 5.44 (manual clustering) and Figure 5.45 (automatic clustering) collect the 12 stereographic projections of the 6 blasts. The *Wulff* projection and the *polar* net is adopted to prevent angular distortion. For each set, the smaller solid circle represents the cone of confidence for a coverage of the 95%, while the larger dashed one represents the spherical aperture. A distinctive colour, previously used during the discontinuities detection, is now associated to each of the four mapped sets:

- red to SvSE set (subvertical in South-East direction);
- blue to SvSW set (subvertical in South-West direction);
- pink to SvE set (subvertical in East direction);
- green to Sh set (subhorizontal).

Using the automatic clustering the subvertical set in East direction (SvE) in pink does not occur. The single blue line represents the bench face plane orientation.

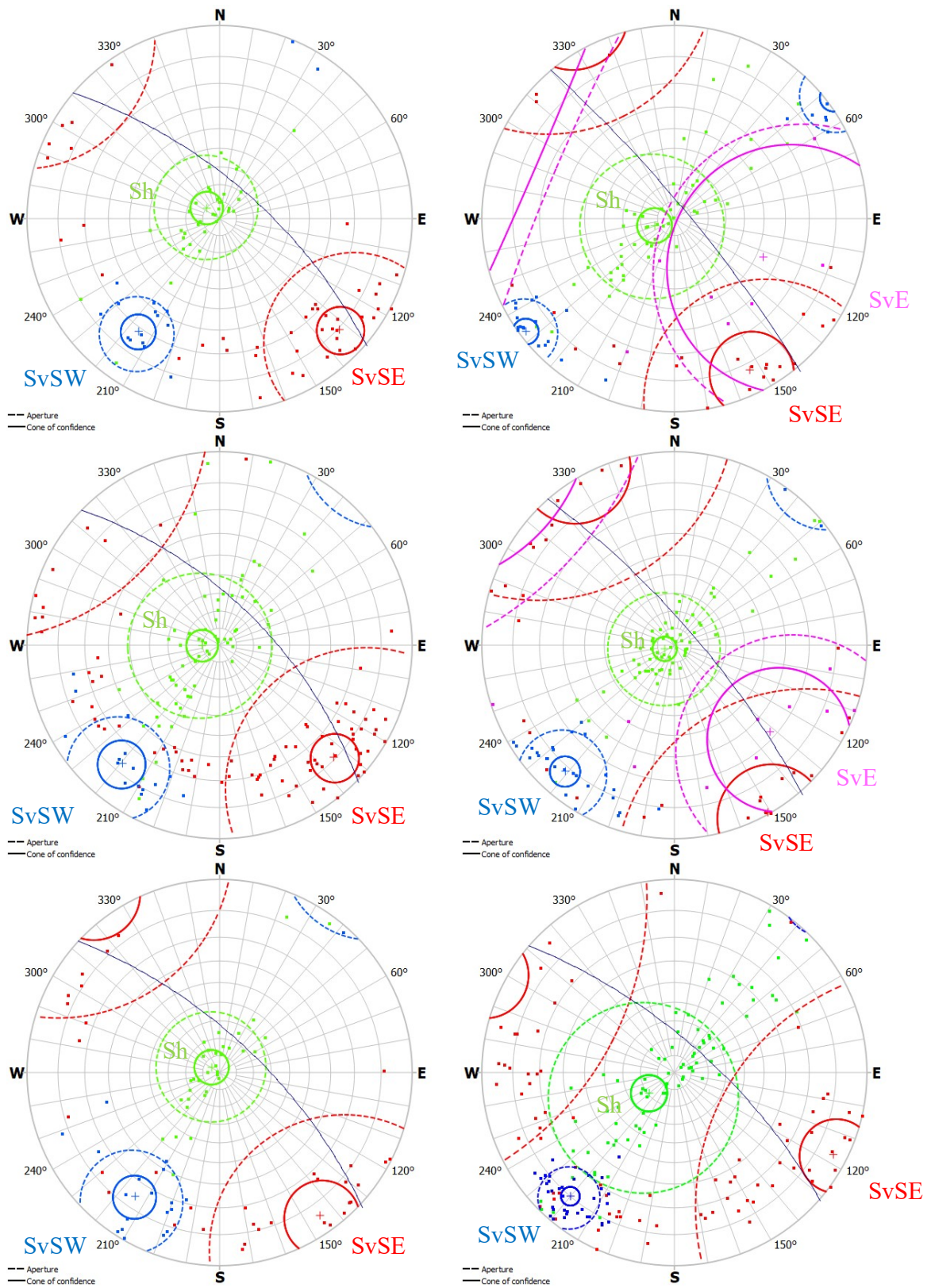


Figure 5.44: manual clustering of the main discontinuity sets by the operator

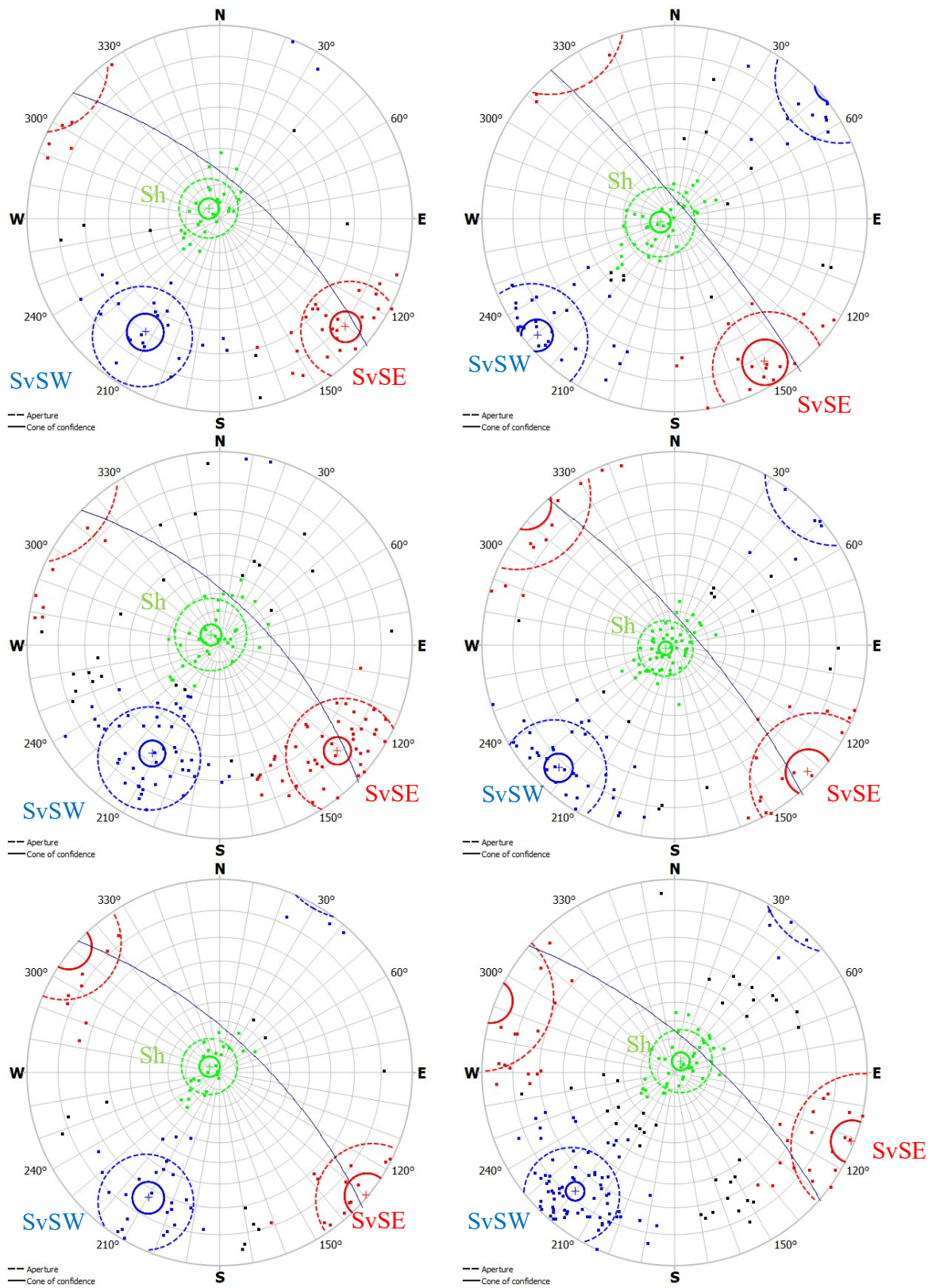


Figure 5.45: automatic clustering of the main discontinuity sets by the ShapeMetrix software

In the first series of stereograms, the 4th set (SvE) in Figure 5.44 appears only in blasts № 8 and 10, while in the second series it does not show up. However, the others three clusters are present in all blasts with a very low variation.

As it is visible, the manual clustering returned high dispersion results, whereas the automatic one gave more compact and defined clusters. Then, some points in manual analysis were erroneously assigned to the wrong set by the operator. In blast № 9 and 12, for example, a lot of points belonging to SvSW set were allocated to SvSE set. This does not happen in the automatic clustering. For these reasons, from this point on, the automatic clustering is considered more appropriated for further analysis and calculations.

Discontinuity sets identification

The ShapeMetriX enables to export information about each set of each blast. In Table 5.13 are listed:

- Orientation of their principal pole: it consists in dip direction and dip angle;
- Spherical aperture: it is a measure of angular dispersion grade of the clusters (represented by the dashed circle in Figures 5.44-45);
- Concentration parameter K : it is a measure of precision and parameter of the Fisher's distribution, further information about it will be given in the following;
- Cone of confidence: it defines a circular area around the mean direction of each set in which the probability to observe a point assigned to that set is $1-p$, then a p value of 0,05 is related to a 95% confidence level (represented by the solid circle in Figures 5.44-45);
- Density: it is calculated as the percentage ratio between the number of joints belonging to the specific set and the total number of joints mapped in the entire blast.

Table 5.13: orientation, spherical aperture, *K* parameter, cone of confidence and density for each set of each blast**BLAST 7**

	Dip Dir (°)	Dip (°)	Spherical aperture	<i>K</i> parameter	Cone of confidence	Density (%)
SvSE	310.59	81.25	16.39	24.32	5.26	35.16
Sh	132.66	8.72	17.35	21.68	5.99	30.77
SvSW	33.29	69.93	19.50	17.20	7.35	26.37

BLAST 8

	Dip Dir (°)	Dip (°)	Spherical aperture	<i>K</i> parameter	Cone of confidence	Density (%)
SvSE	327.75	82.23	18.32	19.22	7.64	18.69
Sh	76.41	8.59	20.29	16.17	6.13	33.64
SvSW	49.73	85.96	17.43	21.71	5.03	36.45

BLAST 9

	Dip Dir (°)	Dip (°)	Spherical aperture	<i>K</i> parameter	Cone of confidence	Density (%)
SvSE	311.75	78.52	19.82	17.07	4.87	32.52
Sh	139.80	7.95	21.08	15.06	6.19	23.31
SvSW	31.98	66.71	20.76	15.58	5.38	29.45

BLAST 10

	Dip Dir (°)	Dip (°)	Spherical aperture	<i>K</i> parameter	Cone of confidence	Density (%)
SvSE	313.37	87.05	19.76	16.83	7.12	19.40
Sh	70.85	5.62	16.30	24.93	4.00	39.55
SvSW	43.51	82.14	17.28	22.13	4.79	31.34

BLAST 11

	Dip Dir (°)	Dip (°)	Spherical aperture	<i>K</i> parameter	Cone of confidence	Density (%)
SvSE	309.83	89.34	16.48	23.67	6.67	24.42
Sh	119.99	6.85	16.44	23.98	6.04	29.07
SvSW	29.73	73.28	17.90	20.43	6.07	33.72

BLAST 12

	Dip Dir (°)	Dip (°)	Spherical aperture	<i>K</i> parameter	Cone of confidence	Density (%)
SvSE	291.23	89.01	20.90	15.27	6.41	18.42
Sh	209.29	7.55	18.43	19.49	5.33	20.53
SvSW	40.00	77.42	16.97	23.19	3.38	41.58

The software considers the discontinuities following a Fisher’s distribution in each set, its analytical form is presented in equation 18 (Fisher, 1953).

$$P = \left(\frac{K}{4\pi \cdot \sin(K)} \right)^{K \cdot \cos(\theta)} \quad \text{eq.18}$$

Where θ is the angular distance from the mean pole of the relative discontinuity set. In the mean pole θ is zero and the density is maximum. When K is high the distribution is confined in the neighbourhood of the maximum, in this case the distribution follows a Gaussian shape (of which K is the invariance in all direction). If K is zero, a uniform distribution would be present in every point of the sphere. The value of this parameter is estimated as presented in equation 19.

$$K = \frac{N-1}{N-R} \quad \text{eq.19}$$

Where N is the number of fractures and R is the mean of the normals of the fractures in the set obtained by vector addition. The equation is valid when $K > 3$ and N is large.

Free faces plane orientation

The software provides also the orientation of the best fitting plane to the bench face: by this way it is possible to relate the orientation of every discontinuity set to the face plane. It is also included in the stereographic representations in Figure 5.42 and 5.43, visible as a continuous blue line.

Table 5.14 shows the face plane orientations and their relative pole for each blast. To pass from the plane to the pole, 180° were added to the strike angle. The mean orientation is 224.63°/72.2°.

Table 5.14: face plane orientations and their relative pole for each blast

	Face plane orientation		Face plane pole orientation	
	Strike (°)	Dip (°)	Dip dir (°)	Dip (°)
Blast 7	40.6	68.4	220.6	68.4
Blast 8	50.1	82.2	230.1	82.2
Blast 9	44.3	65	224.3	65
Blast 10	49	77.7	229	77.7
Blast 11	42.8	68.8	222.8	68.8
Blast 12	41	71.1	221	71.1

This information will be necessary to define the general orientation of each discontinuity set with respect to the free face, which can be classified as: dip into the face, dip out the face, strike perpendicular to the face, horizontal or parallel. This will be indispensable to the calculation of the rock factors in paragraph 6.

Normal set spacing

The ShapeMetriX software enabled obtaining the distance between a joint plane and the subsequent (normal set spacing). This distances are measured on a perpendicular direction in relation to one of those two joint planes; by this way the minimum distance was collected. This process was made for each cluster of each blast; Figures 5.46, 5.47 and 5.48 show an example of the lateral projection of the planes derived from the manual mapping performed by the user for blast № 9. It is notable has the SvSE set presents the higher spacing, while the SvSW presents the lower.

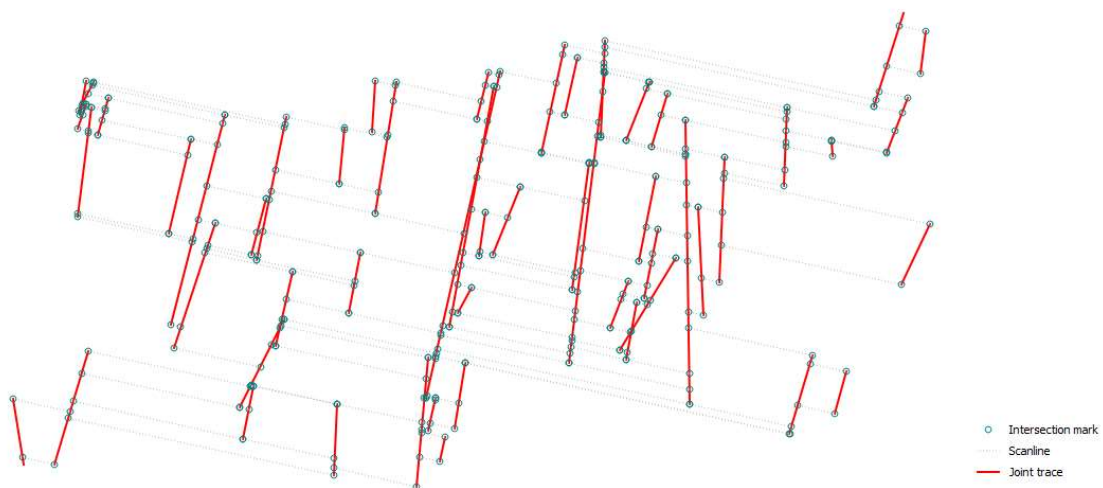


Figure 5.46: projection of the planes marked in blast № 9 by the operator for SvSE set

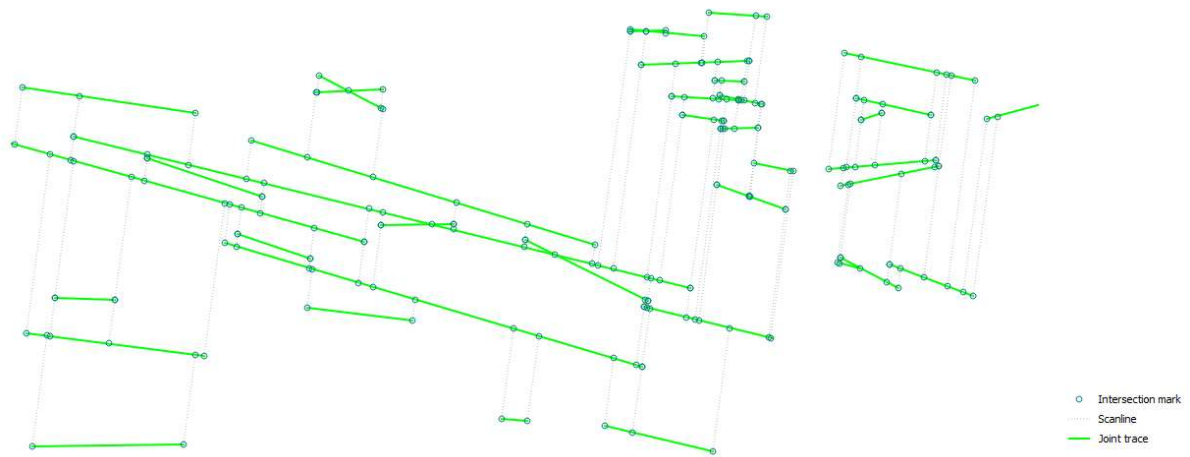


Figure 5.47: projection of the planes marked in blast № 9 by the operator for Sh set

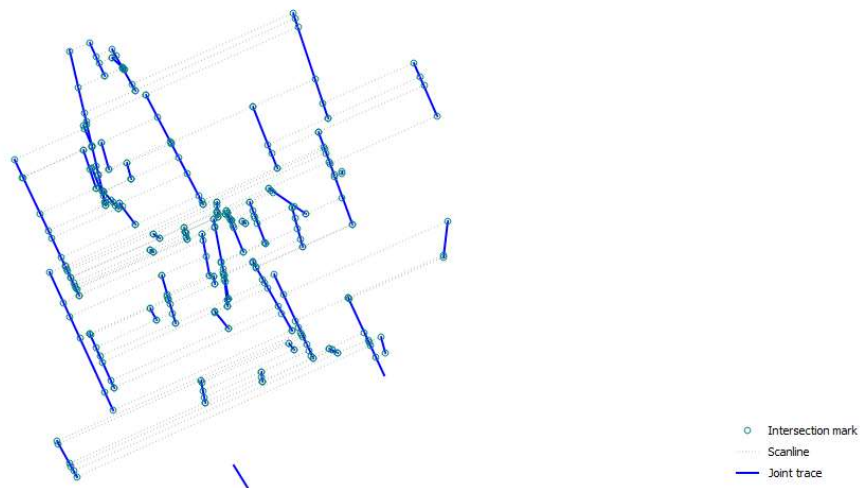


Figure 5.48: projection of the planes marked in blast № 9 by the operator for SvSW set

In Table E.29 (Appendix E) the values of mean, minimum and maximum normal set spacing and its relative standard deviation are collected for each set of each blast. A summary of the means values and their relative standard deviation (after “sd”) is reported in Table 5.15.

Table 5.15: mean values and standard deviation of the normal set spacing for each set of each blast

	SvSE	Sh	SvSW
BLAST 7	2.36 sd 2.82	1.70 sd 1.31	1.03 sd 1.19
BLAST 8	3.42 sd 2.91	1.72 sd 1.62	0.34 sd 0.55
BLAST 9	1.53 sd 1.64	1.30 sd 1.28	1.76 sd 1.78
BLAST 10	4.20 sd 4.29	1.16 sd 1.04	0.73 sd 1.01
BLAST 11	3.78 sd 3.72	1.96 sd 1.59	0.65 sd 0.59
BLAST 12	3.25 sd 3.36	1.63 sd 1.66	0.52 sd 0.57

As observable, except for blast № 9, the SvSE set presents the higher mean normal spacing, while the SvSW presents the lower.

A further statistical analysis consists in the boxplot representation, realized by Matlab; Figure 5.49 visually collects different information:

- The red line inside the box individuates the median value;
- The lower and upper limits of the box represent the interquartile range: it includes the 50% of the data (the upper limit is the 75th percentile and the lower limit is the 25th percentile);
- The red cross symbol stands for an “outlier” value;
- A robust estimation of the 95% confidence interval about the median is individuated by the upper and lower limits of the notch. This last statistic serves to assess the differences in the medians of two groups of data, e.g. if the notches of two boxes overlap, no differences can be assessed at a confidence level of 95 %.

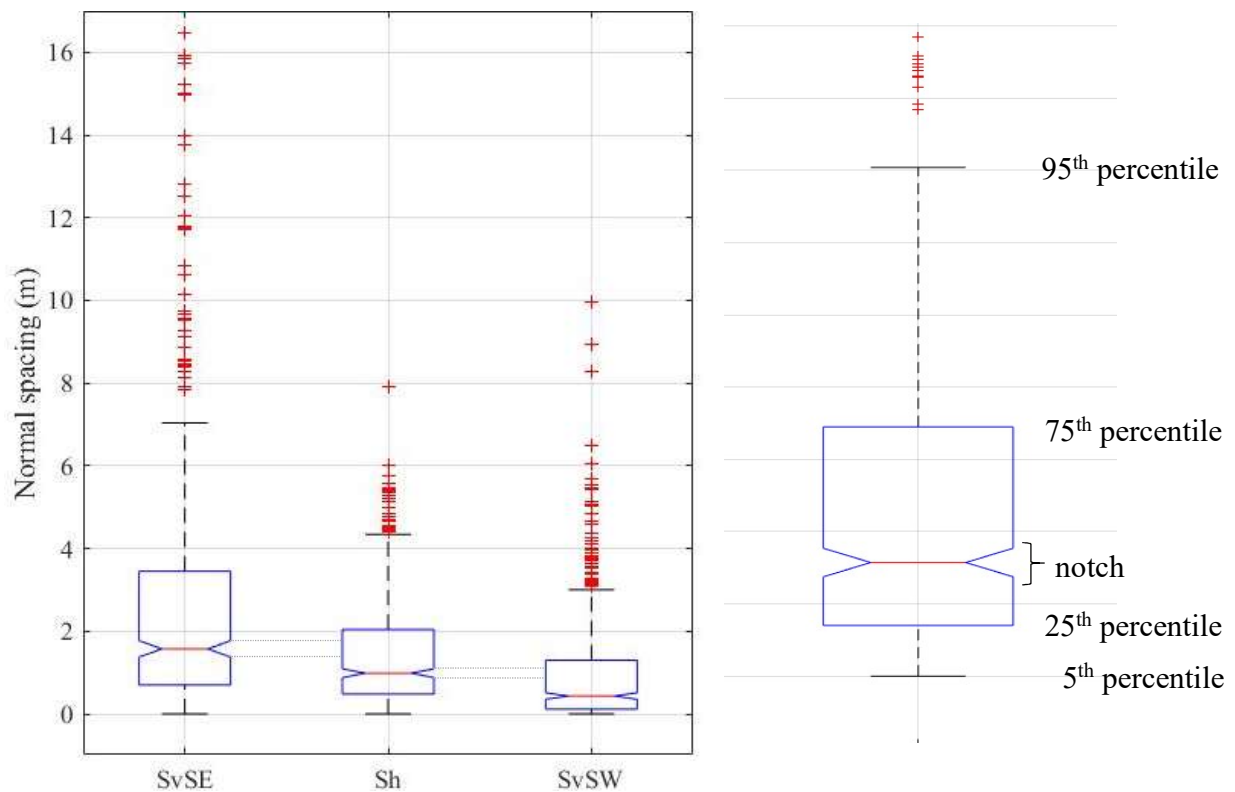


Figure 5.49: boxplot representation of the normal set spacing for each set

As observable in the left of Figure 5.49 the notches relative to the three sets do not overlap, which means those spacings are significantly different each other.

Total spacing

At the time of blasting, as well as the *normal* spacing, the knowledge of the *total* spacing is also interesting. In fact, even though the orientation of joint sets affects the fragmentation (as explained in the paragraph 3.3), analysing the quantity of fractures and their reciprocal spacing, independently of their orientation, is also a useful index. Therefore, photogrammetry models were also analysed to define the mean total spacing.

In ShapeMetriX, 3 scanlines were traced by partitioning the bench height in four equal parts; in Figure 5.51 the scheme for blast № 10 is shown as example. This operation was made after importing the automatic-clustered structure of joints. Then, by the *Show scanline data* tool, was possible to extract a report for each scanline where all type of spacing was collected. The entire list of the spacing of the 18 scanlines is available in the Table F.30 of the Appendix F. In Table 5.16

instead, are grouped only the values of mean, maximum, minimum and standard deviation of the *total* spacing for each blast.

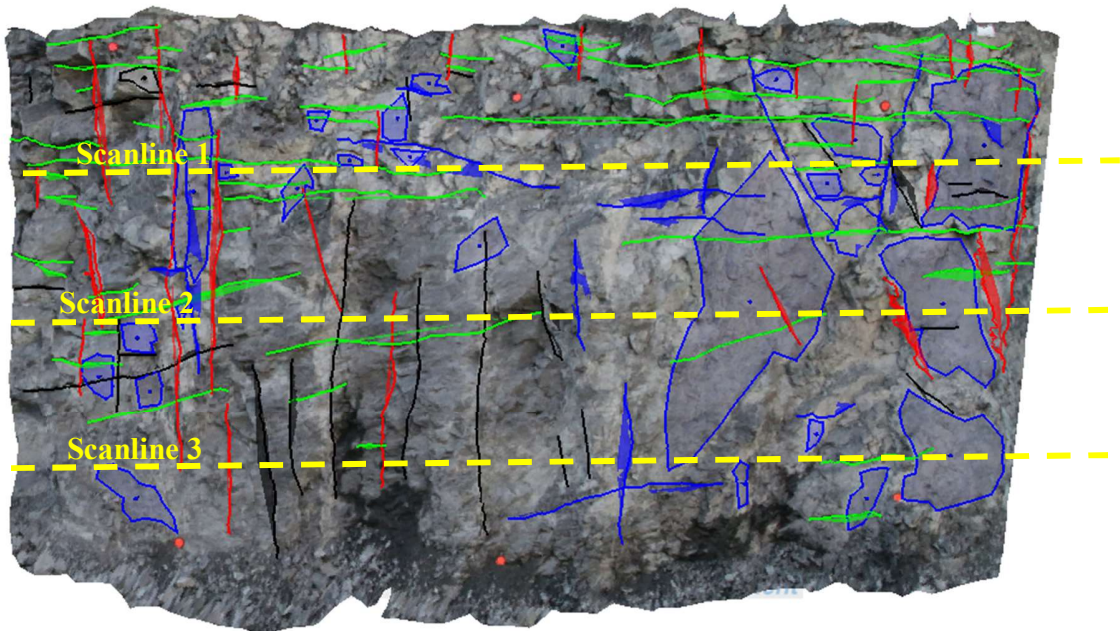


Figure 5.50: scheme of the traced scanlines on the automatic structure of blast № 10

Table 5.16: values of mean, maximum, minimum and standard deviation of the total spacing for each blast

	BLAST 7	BLAST 8	BLAST 9	BLAST 10	BLAST 11	BLAST 12
Mean value	1.09	1.05	0.56	1.23	1.26	0.78
Min value	0.01	0.07	0.04	0.00	0.07	0.02
Max value	3.78	3.59	1.76	6.33	6.20	3.66
Standard dev	0.90	0.84	0.38	1.05	1.22	0.63

Was noticed that the 3rd scanline, which is the bottom one, presents a lower number of intersection with joints with respect to the 1st scanline, which is the top one. Then, for the 3rd scanline were collected a lower number of total spacings. This happened for the six blasts and is due to a non-homogeneous distribution of the discontinuities on the face. In particular, the toe is systematically less fractured with respect to the top.

5.3 Comparison between LiDAR scanning and photogrammetry results

Discontinuity sets comparison

According to the results reported in paragraph 5.1 and 5.2, a satisfactory correlation is appreciable between the two methodologies. In fact, almost a complete combining was possible among the sets individuated by DSE and ShapeMetriX software. The matching results positive if the angular distance between the poles pair is smaller than 35°, the detailed decision criterion and the relative algorithm will be explained in the following.

As can be noticed in Table 5.17, only 4 sets (J5 in blast № 8, J4 and J5 in blast № 9 and J5 in blast № 11) were not associable to any photogrammetry resulting set. However, those sets would find an association if the discrimination angle was increased to 45°. On the other hand, only SvSE set in blast № 8, Sh set in blast № 9, Sh set in blast № 10 and SvSE set in blast № 10 did not found correlation in any LiDAR resulting set. Nevertheless, all others sets were positively matched.

Table 5.17: matches between LiDAR (left) and photogrammetry (right) resulting sets

BLAST 7					
DSE set	Dip dir (°)	Dip (°)	SMX set	Dip dir (°)	Dip (°)
J1	37.93	30.31	Sh	132.66	8.72
J2	221.03	88.75	SvSW	33.29	69.93
J4	190.17	86.66			
J3	336.24	66.00	SvSE	310.59	81.25
J5	291.48	80.30			

BLAST 8					
DSE set	Dip dir (°)	Dip (°)	SMX set	Dip dir (°)	Dip (°)
J1	237.58	85.89	SvSW	49.73	85.96
J4	211.54	81.70			
J2	44.97	59.59			
J3	71.12	8.63	Sh	76.41	8.59
J5	295.39	53.20	-	-	-
-	-	-	SvSE	327.75	82.23

BLAST 9					
DSE set	Dip dir (°)	Dip (°)	SMX set	Dip dir (°)	Dip (°)
J1	32.48	34.49	SvSW	31.98	66.71
J2	207.19	89.40			
J3	350.22	70.00	SvSE	311.75	78.52
J4	104.52	67.16	-	-	-
J5	245.34	88.20	-	-	-
-	-	-	Sh	139.80	7.95

BLAST 10					
DSE set	Dip dir (°)	Dip (°)	SMX set	Dip dir (°)	Dip (°)
J1	228.96	88.76	SvSW	43.51	82.14
J2	214.90	87.51			
J3	97.31	86.19	SvSE	313.37	87.05
J4	288.42	68.25			
-	-	-	Sh	70.85	5.62

BLAST 11					
DSE set	Dip dir (°)	Dip (°)	SMX set	Dip dir (°)	Dip (°)
J1	37.86	30.36	Sh	119.99	6.85
J2	207.19	89.42	SvSW	29.73	73.28
J3	336.24	66.06	SvSE	309.83	89.34
J4	291.50	80.36			
J5	178.27	76.32	-	-	-

BLAST 12					
DSE set	Dip dir (°)	Dip (°)	SMX set	Dip dir (°)	Dip (°)
J1	41.07	88.67	SvSW	40.00	77.42
J2	242.85	89.36			
J3	239.07	69.45			
J4	202.20	69.42			
J5	96.31	24.28	Sh	209.29	7.55
-	-	-	SvSE	291.23	89.01

The incongruences could be consequence of different factors:

- Tolerance: in DSE operations, the tolerance parameter value was set at 20%; in ShapeMetriX analysis instead, it was set at 35%. Clearly, a reduction of this percentage value induces an increasing of the sets number. Therefore, a higher number of discontinuity families was found using the first methodology.
- Resolution: 3D models obtained with laser scanner have a mean final number of points of approximately 550,000 and a mean points spacing of 0.024 m, on the other hand 3D model derived from photogrammetry have approximately 125,000 points and a mean points spacing of 0.08 m. A higher point density per area means more available points to characterise the different planes, so it is explained why more discontinuity sets are individuated by DSE software.
- Algorithm procedure: two software have a different procedure to detect discontinuities. The DSE is based on *semi-automatic* operations that mostly focus on planes detections by the “local curvature calculation” procedure (view paragraph 4.1.5). On the other hand, ShapeMetriX relies on *manual mapping* that mainly examines joints traces, so it calculates planes equations best-fitting 3D polylines.

Associations made in Table 5.17 were deducted by a careful analysis of each set pole orientation (dip direction and dip) obtained by the two methodologies. To do this, the angular distance between each DSE and ShapeMetriX sets poles was calculated with the equation 20. Therefore, the matches result positive if the angular distance between the two vectors is smaller than 35°.

$$\theta_{kj} = \cos^{-1}(|l_k l_j + m_k m_j + n_k n_j|) \quad eq.20$$

where K (l_k, m_k, n_k) and J (l_j, m_j, n_j) are the pair of normal unit vectors relative to the pair of sets found respectively with ShapeMetriX and DSE. This operation is done with a Matlab code that generate K and J starting from the set orientation, then it calculates the angular distance. As example, blast № 7 code is shown:

```

%BLAST7
% sets orientations import (dip dir, dip)
SM=[132.66 8.72; 33.29 69.93; 310.59 81.25];
%Sh, SvSW, SVSE
DSE=[37.93 30.31; 221.03 88.75; 190.17 86.66; 336.24 66.00; 291.48 80.30];
%J1,J2,J3,J4,J5

for k=1:3 %Sh, SvSW, SVSE

    %ShapeMetriX set - K vector generation
    teta=SM(k,1);%Dip direction
    phi=SM(k,2); %Dip angle
    lk=sin(phi*pi/180).*cos(teta*pi/180);
    mk=sin(phi*pi/180).*sin(teta*pi/180);
    nk=cos(phi*pi/180);

    for j=1:size(DSE,1)
        %DSE set - J vector generation
        teta=DSE(j,1);%Dip direction
        phi=DSE(j,2); %Dip angle
        lj=sin(phi*pi/180).*cos(teta*pi/180);
        mj=sin(phi*pi/180).*sin(teta*pi/180);
        nj=cos(phi*pi/180);

        %Angular distance calculation between K and J vectors (equation 20)
        dist7(j,k)=real(acos(abs(lk.*lj + mk.*mj + nk.*nj)))*180/pi;
    end
end
end

```

The resulting matrix makes simple to do matches based on an analytic discrimination. As an example, Table 5.18 presents the angular distances between each pair of sets poles for blast № 7. The positive matches are shown in bold ($\theta_{kj} < 35^\circ$).

Table 5.18: angular distances between each pair of sets poles for blast № 7

	Sh	SvSW	SvSE
J1	32.11	39.75	81.11
J2	88.51	22.63	89.37
J4	82.01	32.60	60.61
J3	74.03	52.67	28.85
J5	88.44	82.43	18.88

A further verification consisted in the comparison of pairs of stereograms (one from DSE and the other from ShapeMetriX). The *Wulff* projection and the *polar* net is adopted to prevent angular distortion. As an example, Figure 5.52 shows the pair from blast № 7; in Appendix G are presented all pairs (Figures G.68-G.73), their relative sets matches and the angular distance between each match (Tables G.31-G.42).

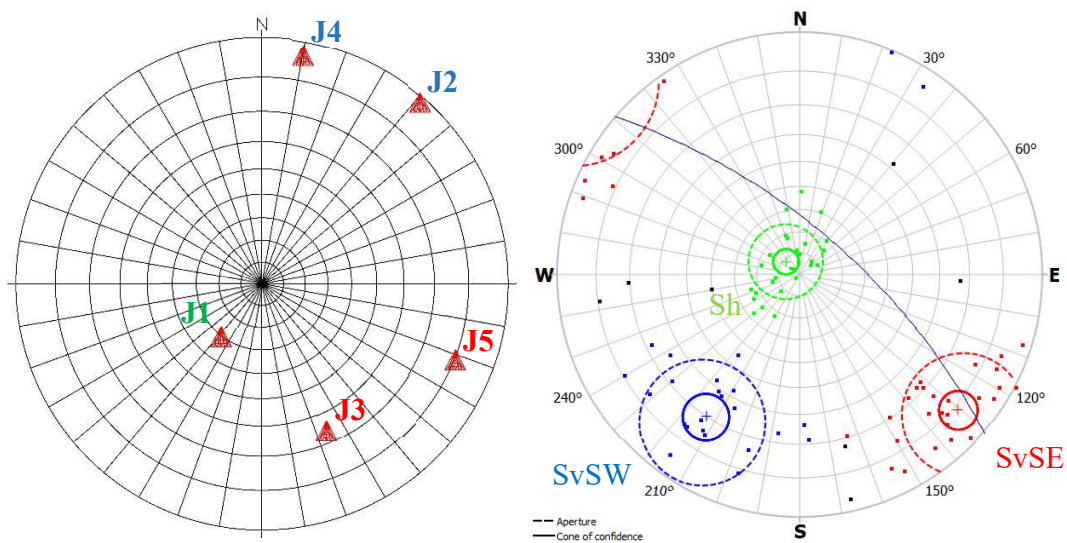


Figure 5.51: comparison of pairs of stereograms from DSE and ShapeMetriX software. The matches are J1 with Sh, J2-J4 with SvSW, and J3-J5 with SvSE

By analysing the entirety of results reported in Appendix G, a systematic pole “rotation” in South-West direction can be observed for SvSW set, which causes its translation to the other extreme of the diagram. On the other hand, a systematic pole “rotation” in North-East direction occurs for Sh set.

The SvSE set is not detectable in LiDAR results from blast № 8 and blast №12, while in photogrammetry ones its presence is clear. The Sh set instead, is not detectable in LiDAR results from blast № 9 and blast №10. Finally, the SvSW set shows in every blast. The DSE software, in fact, mainly rely on plane detection, which are not as exposed for SvSE and Sh sets but are evident for SvSW set. The ShapeMetriX software, instead, mostly process joints traces, so it is able to individuate the SvSE and Sh sets more effectively than SvSW.

In Table 5.19 the mean angular distance for all positive matches of each set of each blast are reported. As notable the maximum value of 35° was exceeded in one case, however, the pair was associated supporting this choice by a visuals analysis of the density plot pair. The SvSW set, which is identified by planes oriented similarly with respect to the free face, presents a higher association with DSE discontinuity sets (J1, J2, ...). On the other hand, Sh and SvSE sets, which are identified by fracture striking the free face, show a lower association. This is due to ability of the DSE software to detect planes (so SvSW) and, by contrast, its difficulty in detecting striking joints (so Sh and SvSE).

Table 5.19: mean angular distance for all positive matches of each set of each blast

	Sh	SvSW	SvSE
BLAST 7	32.10	27.60	23.90
BLAST 8	0.80	19.97	-
BLAST 9	-	28.25	37.90
BLAST 10	-	12.00	33.70
BLAST 11	30.10	17.50	27.45
BLAST 12	28.00	28.28	-

Mean normal set spacing comparison

To characterise de rock mass and its discontinuity families, the analysis of the normal set spacing (defined in paragraph 3.2) is crucial. In particular, it is interesting comparing the values resulting from the two methodologies. In Table 5.20 the *mean* normal set spacing and its relative standard deviation (after “sd”) for each set are compared; Table H.43, that collects the values for each set individuated in each blast, is available in Appendix H.

Table 5.20: comparison of the mean normal set spacing and its relative standard deviation for each set

	DSE results	ShapeMetriX results
SvSE	2.07 sd 1.57	3.09 sd 3.12
Sh	1.28 sd 0.92	1.57 sd 1.41
SvSW	1.12 sd 0.97	0.84 sd 0.94

Set photogrammetry results from SvSE are a little higher with respect to those obtained by LiDAR: this is due to a lower number of joints individuated for that set. This difference is probably due to a difficulty of the operator in the manual-mapping of this precise set and a lower resolution (as explained previously). By increasing the *ppc* parameter value, it could be possible to obtain the same results. It would mean considering only most relevant joints, which probably correspond to those manually identified by ShapeMetriX. Besides, this set presents a very high standard deviation in ShapeMetriX results. However, both results agree with the geological characterization of the area and with the first investigation campaign.

For Sh and SvSW sets, instead, the results are very close one to the other. This can verify: the efficacy of both techniques, the property of the execution of the data acquisition and the correct calibration of the parameters.

5.4 Comparison with geological compass results

As explained in paragraph 2.1, the entire area of the quarry is geologically investigated to understand the mechanism of the ore deposit formation and the tectonic forces that subsequently modified it. One of those monitoring consists in the measurement of the orientation of the visible joints that lean out from the surface by the geological compass. This operation was executed both inside and outside of the quarry site by A. P. Pérez Fortes, a UPM SLIM project team member.

To compare graphically the orientation with previous results a stereographic representation of the orientations is created by RockWorks. Data of manual measurements are relative to the same area where the blasts were executed (station 2). Figure 5.53 presents the resulting plot compared with the stereographic representation of the total poles of the clusters individuated in the six blasts by LiDAR (bottom-left) and photogrammetry (bottom-right) techniques. The *Wulff* projection and the *polar* net is adopted to prevent angular distortion.

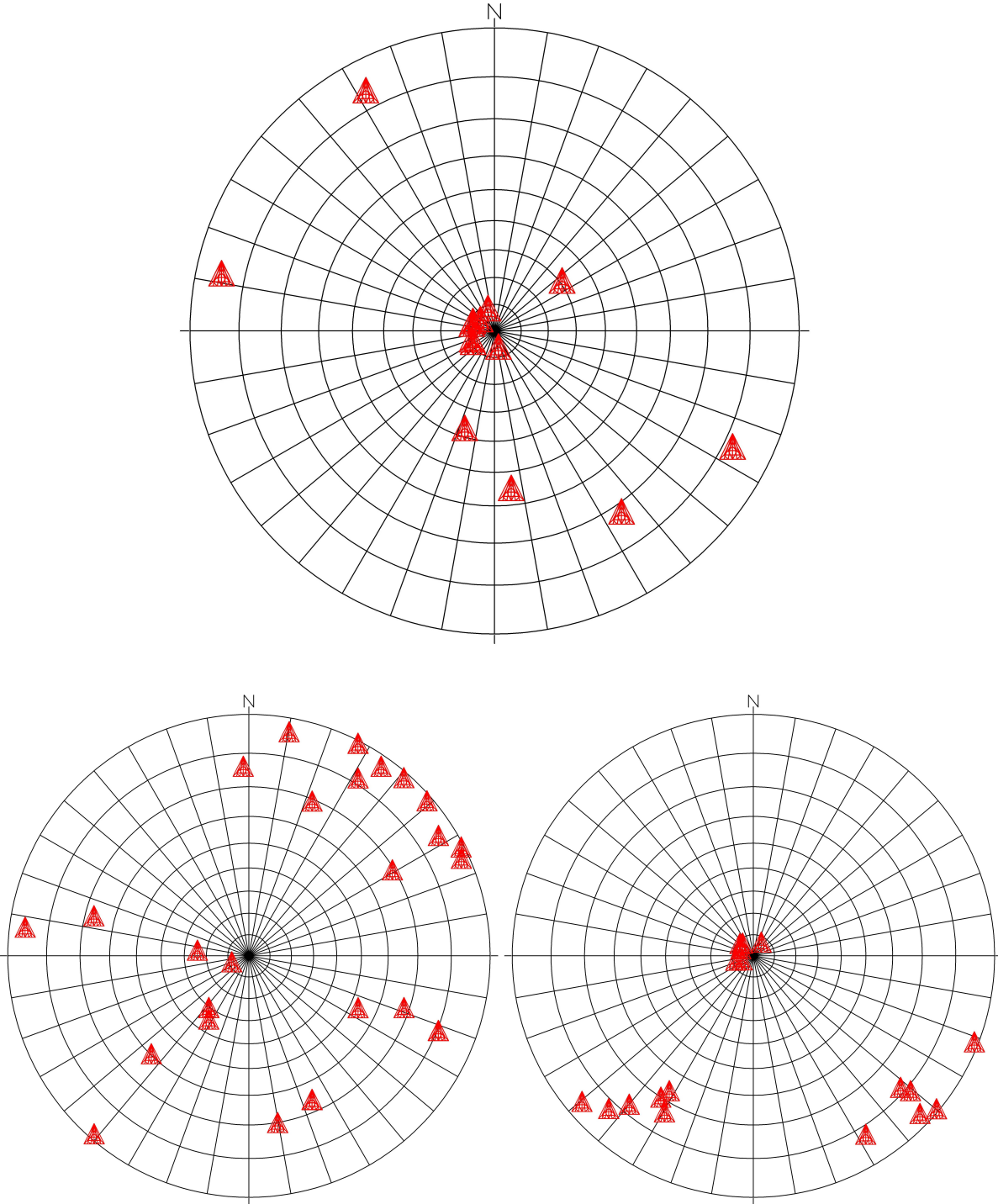


Figure 5.52: comparison between geological compass measurements in station 2 (top) with principal poles individuated by LiDAR (bottom-left) and photogrammetry (bottom-right)

The presence of Sh and SvSE sets is notable in the three diagrams. However, during the acquisition by geological compass was hard to individuate the SvSW set, for this reason it is not present in the top diagram. Maybe, collecting a higher number of measurements could expose this set too. As observable, the photogrammetry results are characterized by a lower dispersion of the mean poles, while the LiDAR ones presents a higher dispersion. However, the correlation between the plots could than validate all techniques efficacy. Finally, it notable as the SvSE photogrammetry set is grouped in two different cluster in LiDAR results.

5.5 Comparison with the 1st investigation campaign

During the first campaign, carried out from May to September 2017, a total amount of 1,356 measurements of the joints orientations were collected. As explained in paragraph 2.1, those data derive from three different investigation methods: photogrammetry monitoring, geological compass data collection and Televier inspection. All these data are grouped by the RockWorks16 software in the stereographic diagram at the top of Figure 5.54; also results from LiDAR (bottom-left) and photogrammetry (bottom-right) are reported for comparison. The *Schmidt* projection and the *equatorial* net is used to represent poles density without areal distortion.

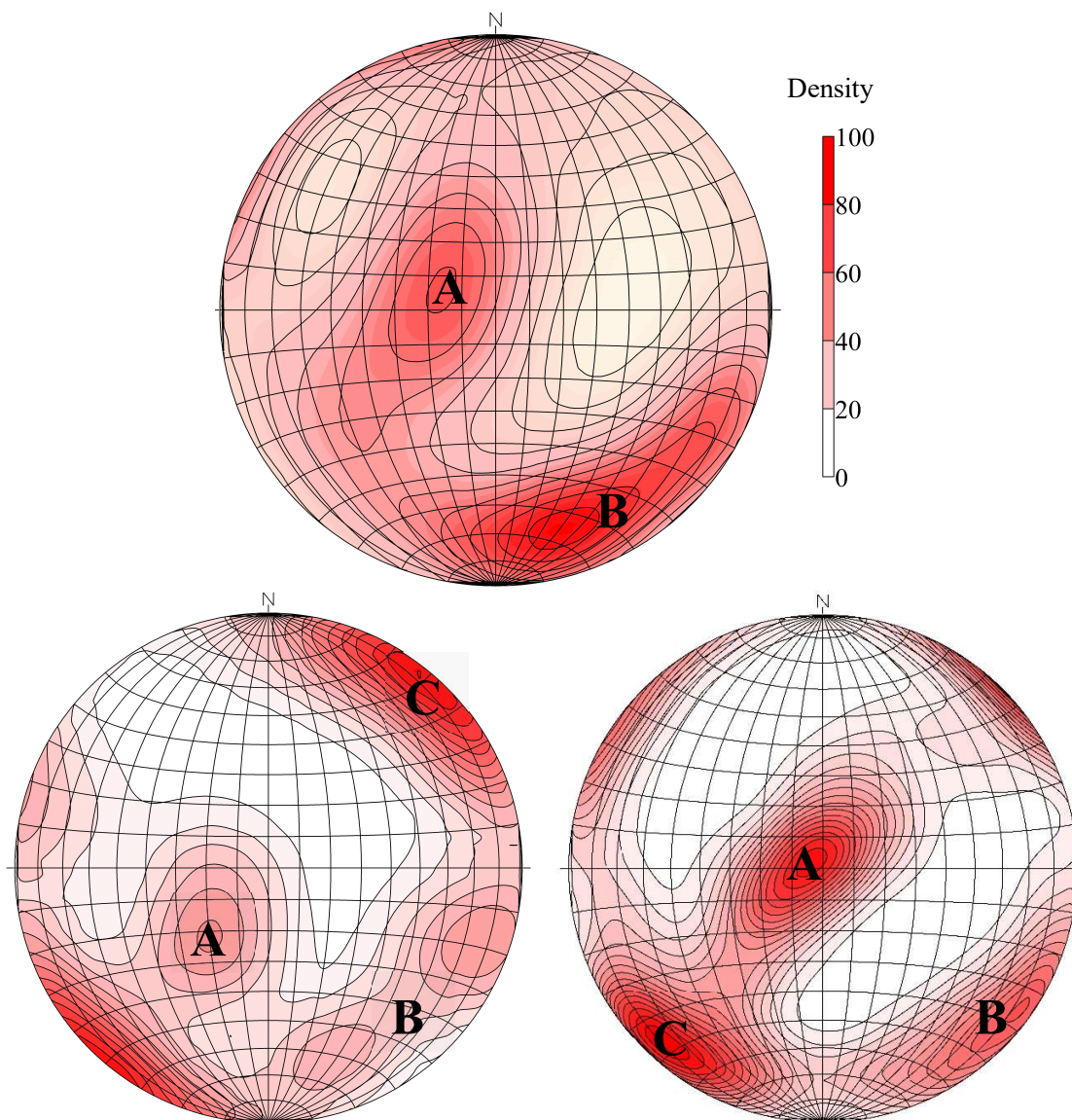


Figure 5.53: comparison between 1st campaign measurements (top) with LiDAR principal poles (bottom-left) and all photogrammetry poles (bottom-right)

Even if the first campaign was executed on an area 30 m far from the second, an evident correlation is observable between the two representations. Then, the geological theory of joints formation assumed in the previous studies can, here again, be adopted. Two main tectonic events were individuated:

- First tectonic event: the most important event is always found in all analysis with very low variation. It is relative to the subhorizontal set (Sh), which presents also as “A” zone in figure.

- Second tectonic event: after the first event, a second generated the joints belonging to “B” and “C” zone. In the second campaign can be found respectively in SvSE and SvSW sets. Those points are characterized by a higher variation with respect to those relative to the first event (“tail extension”).

6. Calculation of rock factors

After obtaining all results, two indexes that characterise the rock mass and its behaviour when blasted can be defined. A correlation between the two factors is expected; moreover, an analysis of the grain size distribution of the post-blast resulting muckpile will be a further check.

The numerical value of both parameters is directly proportional to the fragments size resulting from the blast: this means that it is inversely proportional to the fragmentation that can be obtained. In fact, the more unfavourable are the conditions, the higher is the value of the parameters involved in the calculation formulae. As will be explained later, the range scale of the values of the rock factors are different one each other: the Blastability index, in fact, is generally 8 times higher than the Rock mass discontinuity factor. This is due to the conceptual differences within the two models. However, the proportionality between the two factors in the single blast and the variation of the same factor within different blasts are the objects of analysis.

As explained in paragraphs 3.3.1 and 3.3.2, to calculate both rock factors it is necessary to define the orientation of each set with respect to the free face of the relative blast. In particular, the joint factor JF , needed for the Blastability index calculation, is function of the joint plane angle JPA . On the other hand, the joint orientation term J_O , necessary to calculate the Rock mass discontinuity factor, is function of the Lilly's joints orientation index j_{oi} . Both JPA and j_{oi} depend on the general orientation with respect to the free face, which can be defined in five principal categories: dip into, dip out, strike perpendicular, horizontal or parallel.

To mathematically assign each set of each blast to one of the 5 listed groups, the algorithm in Figure 6.55 was used (Segarra, et al., 2018). Orientations of the sets and the face are the inputs values, then 4 filtering conditions define at which category the set is assigned:

- Step 1: if the dip angle of the set j is lower than the internal friction angle of the rock ϕ , the set is horizontal;
- Step 2: if the dip angle of the set j is lower than the dip angle of the face and the absolute difference between the dip direction of the set j and the dip direction of the face is lower or equal to 30° , this set is dipping out the face.

- Step 3: if the dip angle of the set j is greater than the dip angle of the face and the absolute difference between the dip direction of the set j and the dip direction of the face is lower or equal to 30° , this set is “parallel” to the face.
- Step 4: if the difference between the dip direction of the set j and the opposite of the dip direction of the face is lower or equal to 30° , this set is dipping into the face; otherwise is strike perpendicular to the face.

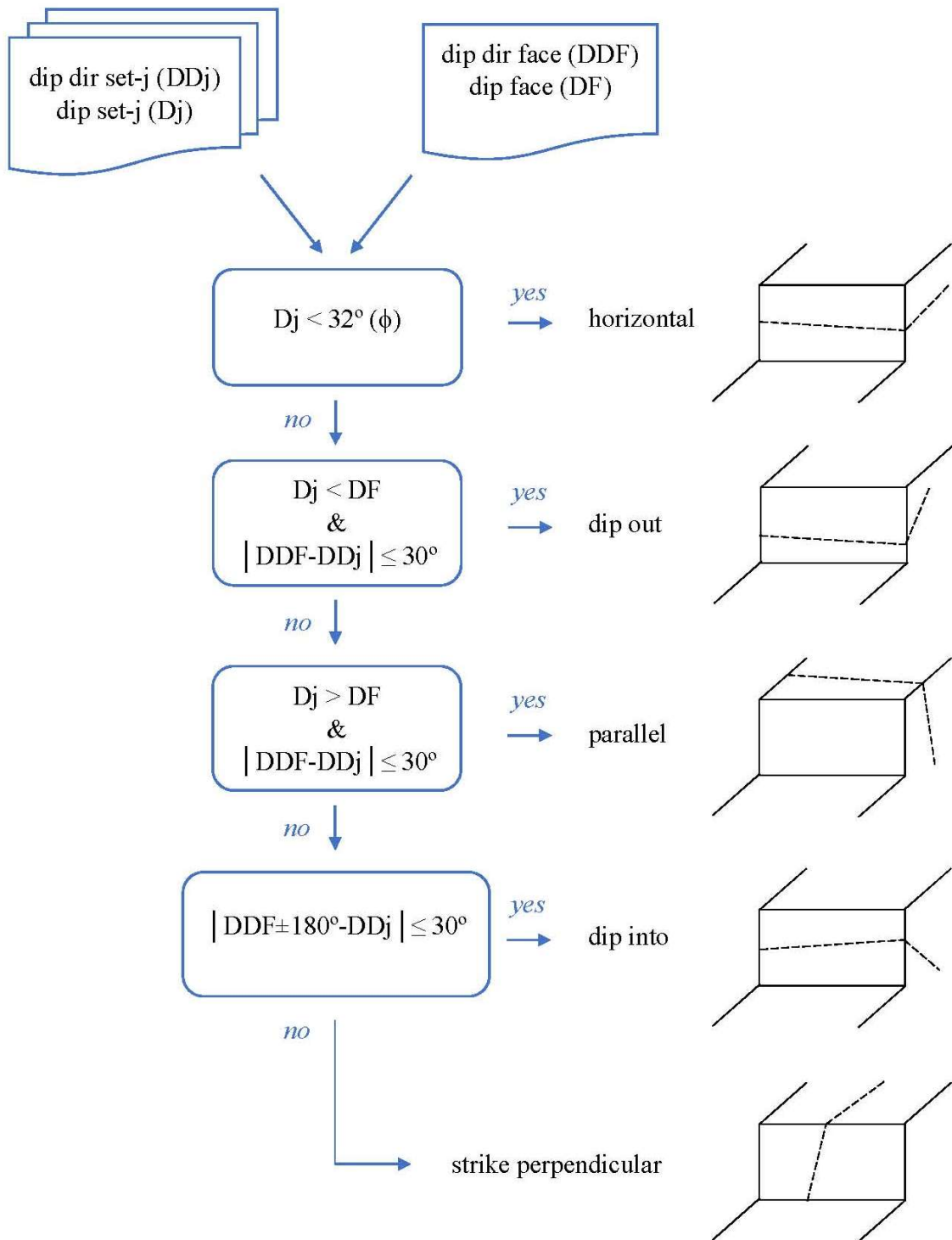


Figure 6.54: algorithm to mathematically assign each set of each blast to one of the 5 groups

6.1 Blastability index (Kuz-Ram model)

The Blastability index was calculated following the procedure explained in paragraph 3.3.1 and assigning values relative to the parameters listed in Table 3.4. In Appendix I, the results for each DSE set for each blast are reported in Tables I.44-I.49, while the results for each ShapeMetriX set for each blast are reported in Tables I.50-I.55. Then the summary comparison between the two techniques is presented in Table I.56.

The mean, weighed with the density of each set, allowed to obtain a unique index for each blast; then, the summary values obtained with both methods are shown in Table 6.21.

Table 6.21: mean Blastability index results for each blast

	Blastability index (A)	
	LiDAR	Photogrammetry
BLAST 7	7.88	7.83
BLAST 8	8.42	7.85
BLAST 9	8.58	7.94
BLAST 10	8.59	7.36
BLAST 11	7.85	7.39
BLAST 12	8.19	8.06

Figure 6.55 shows how the values related to photogrammetry results are systematically lower than the LiDAR ones. However, a general proportionality between both results is appreciable.

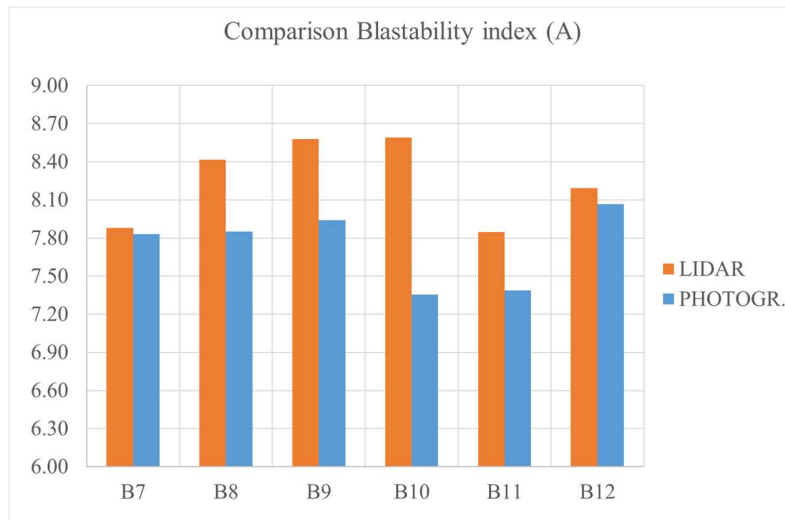


Figure 6.55: representation of the Blastability index for each blast

Then, the predicted x_{50} passing fraction has been calculated using equation 21 (presented in paragraph 3.3.1 - Cunningham model). The result for each blast are shown in Table 6.22.

$$x_{50} = A \cdot A_t \cdot q^{-0.8} \cdot Q^{\frac{1}{6}} \cdot \left(\frac{RWS}{115}\right)^{-\frac{19}{30}} \cdot C(A) \quad eq.21$$

Table 6.22: x_{50} passing fraction predicted by the Cunningham model

	Predicted x_{50} (m)	
	LiDAR	photogrammetry
Blast 7	0.389	0.387
Blast 8	0.479	0.447
Blast 9	0.515	0.477
Blast 10	0.453	0.388
Blast 11	0.349	0.328
Blast 12	0.452	0.445

As it can be observed, the values of x_{50} are characterized by a low variation among blasts. However, the differences allow to predict if any blast will present an anomalous fragmentation in order to eventually modify some blasting parameters to obtain a correct result. In this case, the six campaign blasts seem to give quite similar fragmentation (in terms of x_{50}). Another important consideration has to be done about the satisfactory similarity between LiDAR and photogrammetry result for the single blast. This can verify: the effectiveness of both techniques, the correctness of the execution of the data acquisition and the correct calibration of the parameters.

6.2 Rock mass discontinuity factor (xp-frag model)

The Rock mass discontinuity factor was calculated following the procedure explained in paragraph 3.3.2. The results for each DSE set for each blast are reported in Tables I.57-I.62 (Appendix I), while the results for each ShapeMetriX set for each blast are reported in Tables I.63-I.68. Then the summary comparison between the two techniques is presented in Table I.69.

While in the previous model the Blastability index was calculated in terms of the mean weighed with the density of each set, in this case this operation is not adoptable. In fact, due to the mathematical form of the equation 11 (paragraph 3.3.2), it would not be correct to calculate the weighted average. For this reason, the most unfavourable value (it means the higher) was considered for each blast; this decision was taken based also on literature.

By this way, a single index for each blast has been taken into consideration; Table 6.24 summarizes the values obtained with both methods.

Table 6.23: most unfavourable Rock mass discontinuity factor results for each blast

	Rock mass discontinuity factor	
	LiDAR	Photogrammetry
BLAST 7	1.06	1.00
BLAST 8	1.09	1.09
BLAST 9	1.08	0.98
BLAST 10	1.09	1.09
BLAST 11	1.09	1.09
BLAST 12	0.91	1.09

As shown in Figure 6.57, the results do not present systematically a correlation, as for Blastability index results (view Figure 6.55). However, the values are quite close each other.

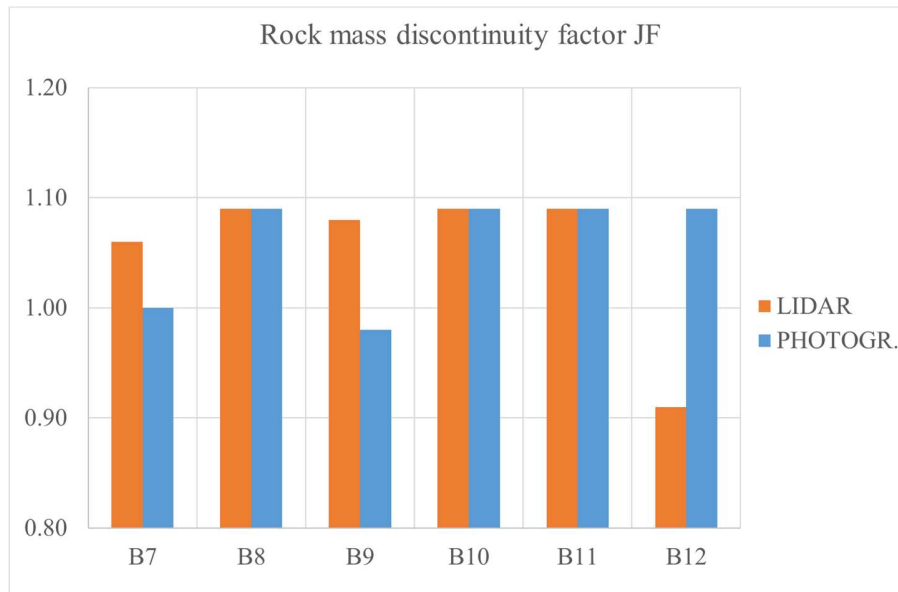


Figure 6.56: representation of most unfavourable Rock mass discontinuity factor for each blast

Then, the predicted x_{50} passing fraction has been calculated using equation 22 explained in paragraph 3.3.2 (Sanchidrián model).

$$\frac{x_p}{L_c} = k \cdot J_F \cdot k_2^h \cdot \left(\frac{\sigma}{q \cdot e}\right)^K \cdot \frac{1}{L_c^{\lambda \cdot K}} \cdot f_t \quad \text{eq.22}$$

The results for each blast are shown in Table 6.25.

Table 6.24: x_{50} passing fraction predicted by the Sanchidrián model

	Predicted x_{50} (m)	
	LiDAR	photogrammetry
Blast 7	0.525	0.496
Blast 8	1.124*	1.124*
Blast 9	0.439	0.398
Blast 10	0.808*	0.808*
Blast 11	0.892*	0.892*
Blast 12	0.391	0.468

As can be observed, the values of x_{50} are characterized by an higher variation between blasts with respect to the previous model. The differences allow to predict if any blast will present an anomalous fragmentation in order to eventually modify some blasting parameters to obtain a correct result.

In this case, the results from blasts № 8, 10 and 11 show anomalies in terms of x_{50} . This is due to the fact that not all the 6 blasts were performed with the same in-row delay: in fact, for the blasts № 7, 9 and 12 a 23 ms delay was adopted between the 7 blastholes, while blasts № 8, 10 and 11 were organized with a delay of only 4 ms. This second model takes in account this difference in its formulae (view equation 22) by means of a time function (f_t) of a non-dimensional delay factor (π_t):

$$f_t = \delta_1 + (1 - \delta_1 - \delta_2 \cdot \pi_t)^{-\delta_3 \cdot \pi_t} \quad eq.23$$

$$\pi_t = \frac{1}{\delta_2} + \frac{1}{\delta_3} - \frac{\delta_1}{\delta_2} \quad eq.24$$

where δ_1 , δ_2 and δ_3 are functions of the normalized passing fraction p , which value is 0.5.

The model seems then to give a too high weight to the time parameter f_t : due to this, the anomalies highlighted in Table 6.25. The blasting campaigns of the SLIM project are performed with different in-row delays (delay between the 7 blastholes of the row) in order to best calibrate this factor.

Another important consideration has to be done about the satisfactory similarity between LiDAR and photogrammetry results for a single blast. This can verify: the effectiveness of both techniques, the property of the execution of the data acquisition and the correct calibration of the parameters.

7. Muckpiles fragmentation analysis

The data acquisition for this last analysis was executed by the writer; however, the analysis of the results will be performed in April 2019, so it is not included in this work. Nevertheless, dealing the main concepts of this approach is useful to understand the potential and the target of this research.

After having performed the blasts, the fragmented material was loaded on dumpers, hauled out of the quarry, and stocked close to the processing plant for the fragmentation analysis. Figure 7.58 shows the muckpiles from blast № 7 and 8 and Figure 7.59 the muckpiles from blast № 9, 10 and 11.



Figure 7.57: muckpiles of fragmented material from blast № 7 and 8



Figure 7.58: muckpiles of fragmented material from blast № 9, 10 and 11

The data collection on fragmentation conditions of the 6 blasts was performed with the LiDAR technique, whose procedure is explained in paragraph 4.1. To best frame the pile, the instrument was installed on a truck 10 m far from the blocks, obtaining a scanning height of approximately 3 m; each scan includes approximately 10-15 m of the pile. The 6 targets are positioned as shown in Figure 7.60, to best individuate the area to scan after the “quick” scan (*low resolution* setting); then, a *high resolution* scan was executed.



Figure 7.59: configuration of the scanstation for muckpiles laser scanning (second scan for blast № 7)

The collection of as many scans as possible was prevented by the conditions of the field around the piles, so a total of approximately 7 scans were performed for each blast. The raw data were converted and trimmed as presented in paragraph 4.1.5; however, no referencing was necessary.

The data analysis, to obtain cumulative size distribution curves, will be carried out in April 2019 by prof. M. Thurley following a specific methodology explained in Thurley (2013) and Thurley (2017). The points cloud is generally adjusted by a 3D rotation of 15° with respect to the horizontal axis. Then, the blocks segmentation can identify 4 categories of elements: *individual* rocks, *overlapped* rocks, *non-overlapped* rocks and *areas-of-fines*. Sizing is applied only on *non-overlapped* rocks and *areas-of-fines*; *overlapped* elements, instead, are filtered to avoid bias due to mis-sizing them as smaller particles. The segmentation is shown in Figure 7.61: predominantly *non-overlapped* elements are colored.

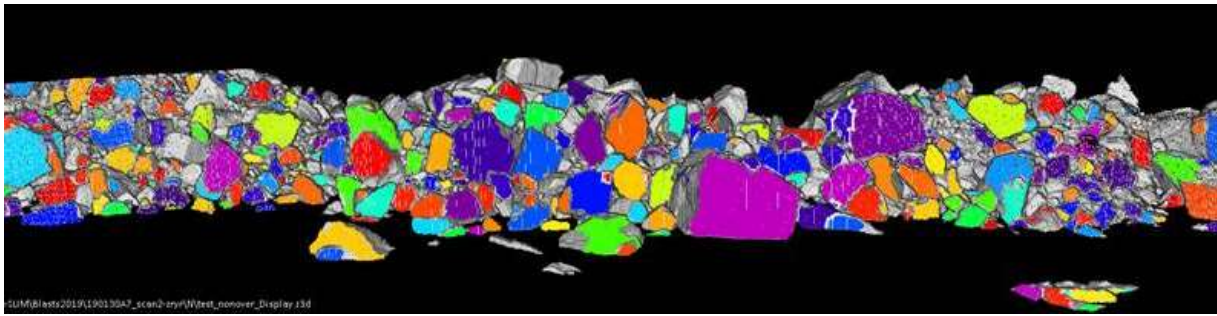


Figure 7.60: resulted segmentation: predominantly non-overlapped elements are presented in color

By this way it will be possible to obtain and compare the size distribution of the 6 different muckpiles resulting from the blasts. Then, a final comparison will be done between the x_{50} values *predicted* by Kuz-Ram and xp-frag fragmentation models and the x_{50} values *estimated* through the fragmentation analysis. This approach will allow to define which model best represents the obtained fragmentation in terms of x_{50} . Moreover, will be compared the LiDAR and the photogrammetry results for each model to find which methodology provides the best inputs (orientation and normal spacing) for the models.

8. Conclusions

The LiDAR data acquisition was performed with a *highest resolution* setting, however the points cloud was subsequently subsampled to reduce the file size and allow the computer to work with a lower size file. For future studies, using the *high resolution* setting (that implies the collection of a lower number of points with respect to the *highest resolution* setting) is advised in order to save time during both acquisition and processing phases. Then, would be interesting to test the merging of two scans, executed from different position with respect to the face. Maybe, the geographical reference of the models allows to overlap both by CloudCompare, in this way the “stereo” acquisition mode could increase resolution and precision of the resulting model.

From the LiDAR results it can be noticed that in the six blasts the main discontinuity sets repeat approximately in the same zone of the stereographic projection: this is the evidence of a geological structure that repeats in every blast.

The photogrammetry manual clustering returned high dispersion results, whereas the automatic one gave more compact and defined clusters. Then, some points in manual analysis were erroneously assigned to the wrong set by the operator. For these reasons, the automatic clustering is considered more appropriated for analysis and calculations. From the total spacing analysis was noticed a non-homogeneous distribution of the discontinuities on the face. In particular, the toe is systematically less fractured with respect to the top.

A satisfactory correlation is appreciable between the two methodologies, in fact, almost a complete combining was possible among the sets individuated by DSE and ShapeMetriX software. Only 4 LiDAR sets (J5 in blast № 8, J4 and J5 in blast № 9 and J5 in blast № 11) were not associable to any photogrammetry resulting set. However, those would find an association if the discrimination angle was increased to 45°. Generally, the SvSW set, which is identified by planes oriented similarly with respect to the free face, presents a higher association with DSE discontinuity sets. On the other hand, Sh and SvSE sets, which are identified by fracture striking the free face, show a lower association. This is due to ability of the DSE software to detect planes (so SvSW) and, by contrast, its difficulty in detecting striking joints (so Sh and SvSE).

In terms of mean normal set spacing the photogrammetry results from SvSE are a little higher with respect to those obtained by LiDAR: this is due to a lower number of joints individuated for that

set. This difference is probably due to a difficulty of the operator in the manual-mapping of this precise set and to a lower resolution. Besides, this set presents a very high standard deviation in ShapeMetriX results. However, both results agree with the geological characterization of the area and with the first investigation campaign. For Sh and SvSW sets, instead, the results are very close one to the other.

Comparing the mean poles individuated during the whole campaign by both methods, a lower dispersion of the clusters resulted from the photogrammetry is noticed, while the LiDAR ones presents a higher dispersion. However, the correlation between the results could validate the techniques efficacy. Finally, it notable as the SvSE photogrammetry set is grouped in two different cluster only in LiDAR results.

The comparison with the geological compass verify the presence of Sh and SvSE sets. However, during the manual acquisition of the orientations was hard to individuate the SvSW set, for this reason it does not found a correspondence. Maybe, collecting a higher number of measurements could expose this set too.

Applying the Kuz-Ram model was observed that the values of the predicted x_{50} are characterized by a low variation between blasts. The differences allow to predict if any blast will present an anomalous fragmentation in order to eventually modify some blasting parameters (such as the specific drilling, the charge per hole, the initiation system or the explosive type) to obtain a correct result. In terms of predicted x_{50} , the six campaign blasts seem to give quite similar fragmentation.

Applying the xp-frag model instead, the values of predicted x_{50} are characterized by a higher variation between blasts with respect to the previous model. In this case, the result from blasts № 8, 10 and 11 present anomalies in terms of x_{50} . This is due to the fact that this model seems then to give a too high weight to the time function (f_t) of the non-dimensional delay factor (π_t). For this reason, the blasting campaigns of the SLIM project are executed with different in-row delays in order to then calibrate this factor.

Another important consideration has to be done about the satisfactory similarity between LiDAR and photogrammetry result for the single blast applying both models. This can verify: the efficacy of both techniques, the property of the execution of the data acquisition and the correct calibration of the parameters.

Then, the final comparison between the x_{50} *predicted* values by the fragmentation models and the x_{50} *estimated* values with the fragmentation will be done by the writer in April 2019. This final analysis will allow to define the model which best represents the resulting fragmentation in terms of x_{50} and the best methodology to obtain the inputs data for the models. By this way, a further calibrations of the necessary parameters can contribute to improve the knowledge in fragmentation prediction in rock blasting.

9. References

- Barton, N., 1978. Suggested methods for the Quantitative Description of Discontinuities in Rock Masses, Intl. Journal Rock Mech. Min. Sci. & Geomech. Abstr., Vol. 15, pp. 319-368;
- Benito Arnó e hijos, 2016. Actualización del informe de obtención del distintivo de calidad adif para el suministro de balasto. Estudio geológico, geotécnico y petrográfico. Abril 2016;
- Bergmann, O.R., Wu, F.C., Edl, J.W., 1974. Model rock blasting measures effect of delays and hole patterns on rock fragmentation. E/MJ Mining Guidebook: System for Emerging Technology, June, pp124-127;
- Buyer. A., Schubert. W., 2017. Calculation the Spacing of Discontinuities from 3D Point Clouds. Procedia Engineering 191:270-278. December 2017. DOI: 10.1016/j.proeng.2017.05.181;
- CloudCompare 2017. Girardeau-Montaut. GPL software (version 2.8.1) <http://www.cloudcompare.org/>;
- Cunningham, C.V.B., 2005. He Kuz-Ram fragmentation model – 20 years on. In: Proceedings of 3rd world conference on explosives and blasting, Brighton, UK, 13-16 September 2005, pp 201-210;
- Cyclone 2012. Leica Geosystem Inc. – Hexagon Geosystems (version 7.4.0). <https://leica-geosystems.com/products/laser-scanners/software/leica-cyclone>;
- DSE discontinuity set extractor 2015. A. Riquelme (version 2.XX). <https://personal.ua.es/en/ariquelme/discontinuity-set-extractor-software.html>;
- Enrile, J. H. (1981). Evolución microestructural de rocas cuarzo-feldespáticas como resultado del aumento de la deformación en la milonita de Toledo. Journal of Iberian geology: an international publication of earth sciences, 7, 547-566;
- Fernández, A., 2018. Use of LiDAR technique to guide blasting: Rock mass characterization and fragmentation assessment. SLIM Technical Report;
- Fisher, R. (1953). Dispersion on a sphere. Proceedings of the Royal Society of London. Series A. Mathematical and Physical Science, 217(1130), 295-305;
- Fueyo, L., de la Cuadra, C.A. (2016). Actualización del informe de obtención del distintivo de calidad ADIF para el suministro de balasto. Estudio geológico, geotécnico y petrográfico. Fueyo Consultores y Benito Arnó e Hijos SAU;

- Gomes, T., Pérez Fortes, A.P., Segarra, P., Natale, M., 2017. Procedure for rock mass characterization with optical Televiewer. SLIM Technical Report;
- Gomes, T., Segarra, P., Pérez Fortes, A.P., Xisheng, G., 2017. Procedure for rock mass characterization with photogrammetry. SLIM Technical Report;
- Hack, H.R.G.K., 2003. Discontinuous rock mechanics. Lecture notes, version 2 (unpublished), International Institute for Aerospace Survey and Earth Sciences (ITC), Enschede, The Netherlands;
- Hobbs, B.E., Means, W.D. and Williams, P.F., 1976. An Outline of Structural Geology, J. Wiley & Sons, New York, 571 pp;
- Hustrulid, W., 1999. Blasting principles for open pit mining. Taylor & Francis Group, LLC;
- Iglesias, L., 2017. El Aljibe test blast – 2017. Data acquisition with UAV. SLIM Technical Report;
- Jaboyedoff M, Oppikofer T, Abellan A, Derron MH, Loye A, Metzger R, Pedrazzini A (2012) Use of LiDAR in landslide investigations: a review. Nat Hazards 61:5–28;
- Jaboyedoff M, Oppikofer T, Locat A, Locat J, Turmel D, Robitaille D, Demers D, Locat P (2009) Use of ground-based LIDAR for the analysis of retrogressive landslides in sensitive clay and of rotational landslides in river banks. Can Geotech J 46:1379–1390;
- Lilly, P.A., 1992. The use of blastability index in the design of blast open pit mines. Western Australia School of Mines, Kalgoorlie, pp 421-426;
- Martínez-Salanova, J., Martín Parra, L., Gutiérrez Alonso, G., Martín Herrero, D., Sánchez Carretero, R., Andonaegui, P., . . . Iglesias Peláez, A. (2009). Memoria de la Hoja nº 658 (Mora). Mapa Geológico de España E. 1:50.000 (MAGNA), Segunda Serie, Primera edición;
- Navarro, J., Segarra, P., Castedo, R., 2017. High speed video recording to determine rock movement. SLIM Technical Report;
- Patton, F.D., 1996. Multiple modes of shear failure in rock. Proc. 1st Congr. On Rock Mechanics, ISRM, Lisbon, Portugal, 1. ed. Rocha M. pp. 509-513;
- Ravanel, L., Bodin, X. & Deline, (2014). Using Terrestrial Laser Scanning for the Recognition and Promotion of High-Alpine Geomorphosites;
- Ravanel, L., Bodin, X. & Deline, Using Terrestrial Laser Scanning for the recognition and promotion of high-alpine geomorphosites (2014) 6: 129;

- Riquelme, A. J., Abellán, A., Tomás, R., & Jaboyedoff, M. (2014). A new approach for semi-automatic rock mass joints recognition from 3D point clouds. *Computers & Geosciences*, 68, 38-52;
- Riquelme, A.J., Abellán, A., Tomás, R., Jaboyedoff, M., 2014. A new approach for semi-automatic rock mass joints recognition from 3D point clouds. Universidad de Alicante, Alicante, Spain;
- RockWorks 2016. RockWare – Earth Science & GIS Software. Golden, Colorado USA;
- Sanchidrián, J.A., López, L.M., Segarra, P., 2017. Near-field seismic measurements. SLIM Technical Report;
- Sanchidrián, J.A., Ouchterlony, F., 2016. A Distribution-Free Description of Fragmentation by Blasting Based on Dimensional Analysis, Springer;
- Segarra, P., Pérez Fortes, A.P., Fernández, A., Gomes, T., Gao, X., 2018. Geomechanical models of El Aljibe tests blasts from measurements of the free face with photogrammetry and LiDAR, 4-5. SLIM Technical Report;
- Segarra, P., Sanchidrián, J.A., 2017. Dust emission in mining (TSP, PM10 and crystalline silica). SLIM Technical Report;
- Segarra, P., Sanchidrián, J.A., Castedo, R., 2018. Engineering models for rock fragmentation prediction. SLIM Technical Report;
- Segarra, P., Sanchidrián, J.A., López, L.M., Castedo, R., Iglesias, L., Navarro, J., 2017. Tests blasts-2017. El aljibe characteristics and fragmentation with mobile screens. SLIM Technical Report;
- ShapeMetriX 3S-SMX 2010. 3GSM (version 4.3);
- Slob, S., (2010). Automated rock mass characterization using 3-D terrestrial laser scanning. 7-25;
- Thurley, M., 2013. Automated image segmentation and analysis of rock piles in an open-pit mine, 2013 International Conference on Digital Image Computing: Techniques and Applications (DICTA 2013), Hobart, Australia, 26–28 November 2013, Vol. 8, 6691484, Piscataway, NJ, IEEE;
- Thurley, M., 2017. Fragmentation monitoring of run-of-mine (ROM). Controlling rock fragment size distribution: large and small-scale testing. SLIM Technical Report;

- UShapeMetriX3D User Manual – 3D imaging for measuring and assessing rock and terrain surfaces, December 2010;
- Yi, C., Johansson, D., Nyberg, U., Castedo, R., Natale, M., Santos, A.P., Segarra, P., Sanchidrián, J.A., 2018. Fragmentation prediction – Numerical Modelling. SLIM Technical Report;

Appendix A: geological compass measurements

In Table A.21 the orientation values collected in the 3 measurement stations positioned as Figure 2.7 shows (paragraph 2.1) are listed. Station 2 was in correspondence with the blast № 7 of the second investigation campaign.

Table A.25: list of the orientation values collected in the 3 monitoring stations

Station 1		Station 2	Station 3
Dip dir(°)/Dip(°)		Dip dir(°)/Dip(°)	Dip dir(°)/Dip(°)
169/68	198/38	70/9	189/84
322/65	198/38	152/84	189/84
176/60	155/74	108/9	189/84
176/60	155/74	102/85	275/65
172/70	155/74	17/37	260/73
266/78	205/22	233/31	260/9
266/78	205/22	63/9	258/81
266/78	205/22	296/82	272/8
266/78	174/74	325/72	174/59
266/78	174/74	164/9	266/9
151/64	174/74	346/6	88/86
271/72	160/66	346/6	261/9
271/72	179/80	346/6	261/9
157/68	90/72	346/6	261/9
157/68	94/80	346/6	261/9
157/68	173/36	115/9	276/64
329/70	173/36	130/7	
146/70	173/36	354/55	
147/70	94/72		
146/72	155/4		
147/72	155/4		
166/76	255/78		
166/76	114/84		
168/76	102/80		
147/72	104/78		
198/38			

Appendix B: geo-referencing coordinates

In Table B.22 the 3 coordinates (E, N, Z) are reported for each control points used for geo-referencing 3D model resulting from both LiDAR and photogrammetry techniques. To reduce error in the aligning process, there were subtracted 428,000 to the East coordinate and 4,400,000 to the North coordinate.

Table B.26: coordinates of the six target points for each blast

TARGET POSITION	BLAST 7			BLAST 8		
	E	N	Z	E	N	Z
up-right	428144.43	4400170.53	654.84	428126.69	4400190.66	653.93
up-center	428150.18	4400166.29	653.74	-	-	-
up-left	428156.59	4400159.03	654.43	428137.30	4400176.16	654.68
bottom-right	428145.60	4400173.13	644.88	428128.32	4400189.86	644.91
bottom-center	428151.73	4400169.23	645.98	428131.85	4400185.19	644.33
bottom-left	428157.68	4400164.26	644.98	428138.21	4400179.23	644.11

TARGET POSITION	BLAST 9			BLAST 10		
	E	N	Z	E	N	Z
up-right	428139.21	4400169.82	655.17	428124.44	4400185.72	653.17
up-center	428150.24	4400161.76	654.08	428130.21	4400178.47	653.44
up-left	428153.97	4400154.62	655.21	428136.99	4400169.95	654.76
bottom-right	428142.80	4400172.17	644.96	428125.66	4400187.20	643.69
bottom-center	428149.24	4400167.25	645.05	428132.45	4400180.23	642.38
bottom-left	428155.05	4400161.30	645.92	428137.52	4400174.23	642.93

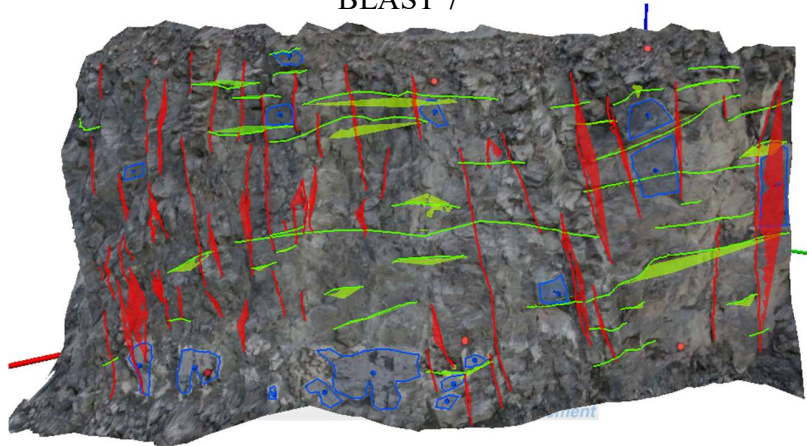
TARGET POSITION	BLAST 11			BLAST 12		
	E	N	Z	E	N	Z
up-right	428136.40	4400167.32	654.31	428135.52	4400163.31	654.86
up-center	428145.84	4400160.29	654.92	428145.12	4400156.49	653.37
up-left	428152.33	4400152.11	654.62	428148.97	4400151.08	653.81
bottom-right	428138.36	4400168.78	644.45	428138.35	4400164.38	644.98
bottom-center	428148.41	4400162.44	644.92	428147.05	4400158.61	644.84
bottom-left	428155.64	4400157.38	644.27	428149.56	4400155.64	645.73

Appendix C: manual and automatic structure maps

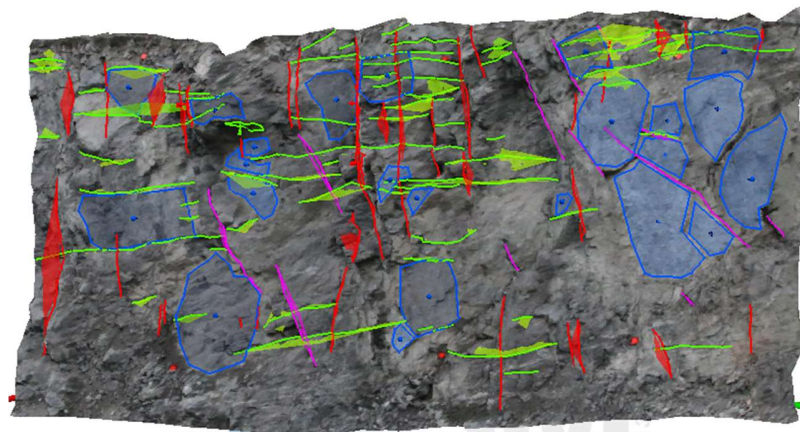
In Figure C.65 the manually marked structure is presented, the clustering is defined by the operator. A family (structure set) was assigned to every joint according to its orientation; different colours were given to each set:

- red to the SvSE set (subvertical in South-East direction);
- blue to the SvSW set (subvertical in South-West direction);
- green to the Sh set (subhorizontal).

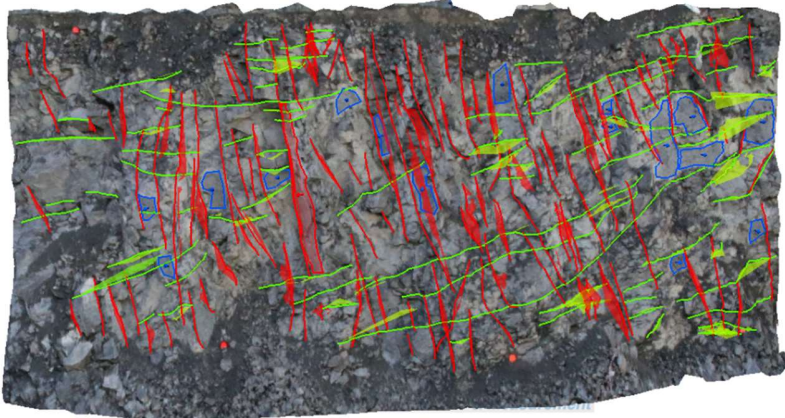
BLAST 7



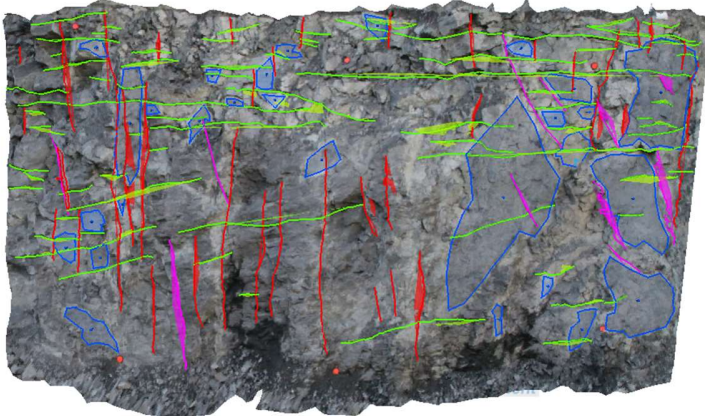
BLAST 8



BLAST 9



BLAST 10



BLAST 11



BLAST 12

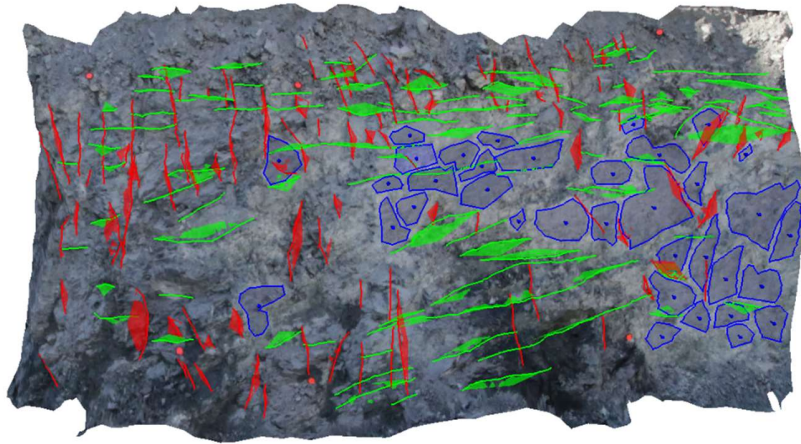
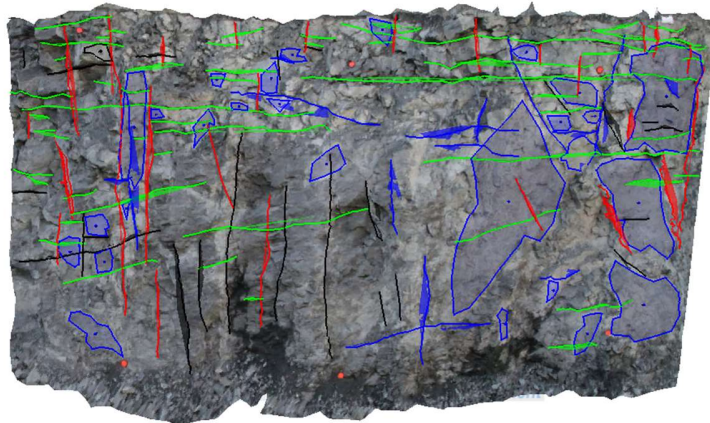


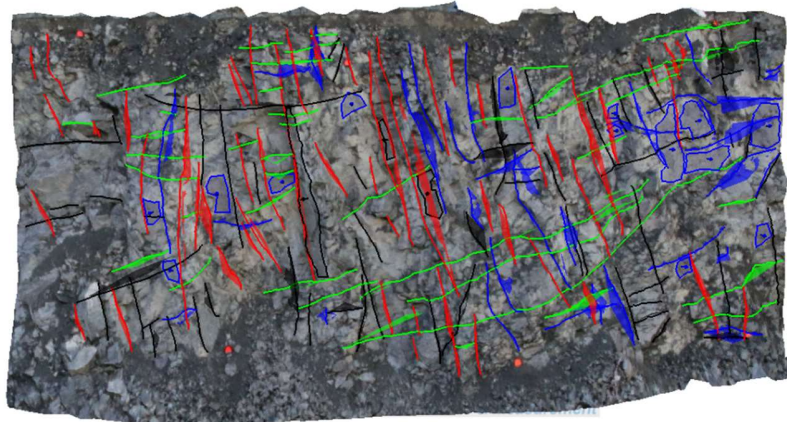
Figure C.61: manual cluster of the structure map marked by the operator

In Figure C.66 the automatic clustering of the marked joints is executed by the ShapeMetriX software. Not assigned joints are presented in black.

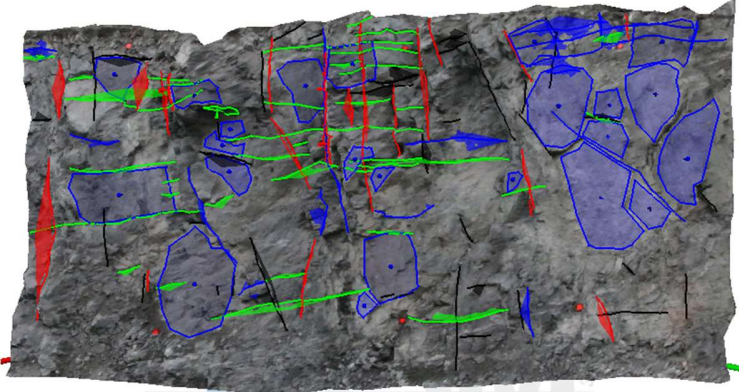
BLAST 7



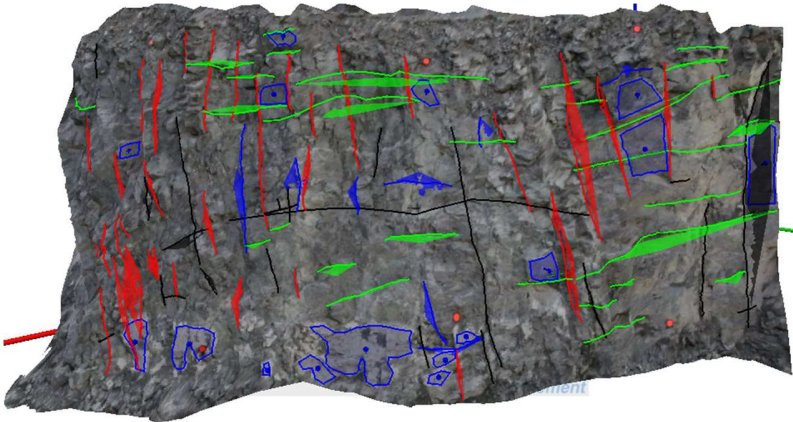
BLAST 8



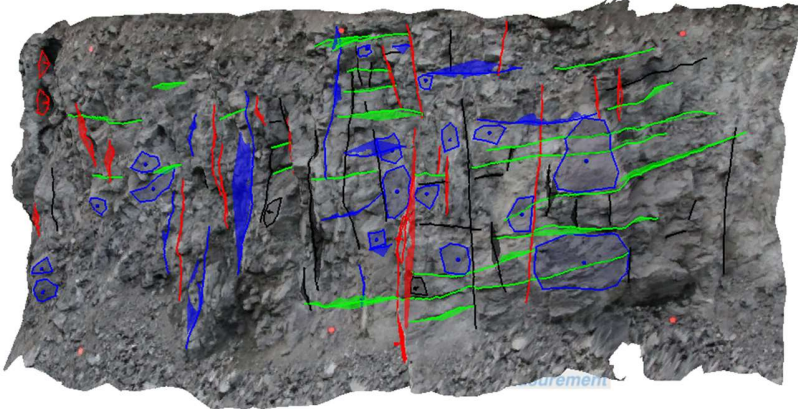
BLAST 9



BLAST 10



BLAST 11



BLAST 12

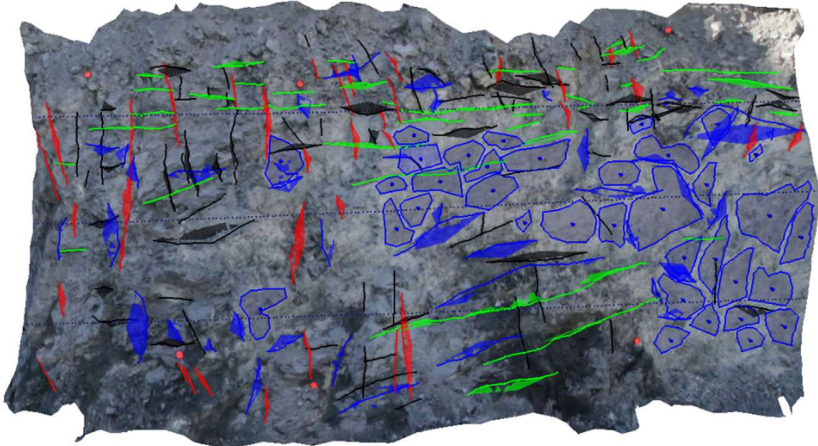


Figure C.62: automatic clustering of the structure map by ShapeMetriX software

Appendix D: density plot resulting from DSE

Figure D.67 shows the density plots for each blast; it is notable as the higher density pick was considered as the bench face, then no set was assigned to it. A systematic error occurs in this type of representation: those poles, in fact, should be represented with the *Schmidt* projection to prevent areal distortion. However, this diagram was useful to visually analyse the density of each pole and exclude the bench one.

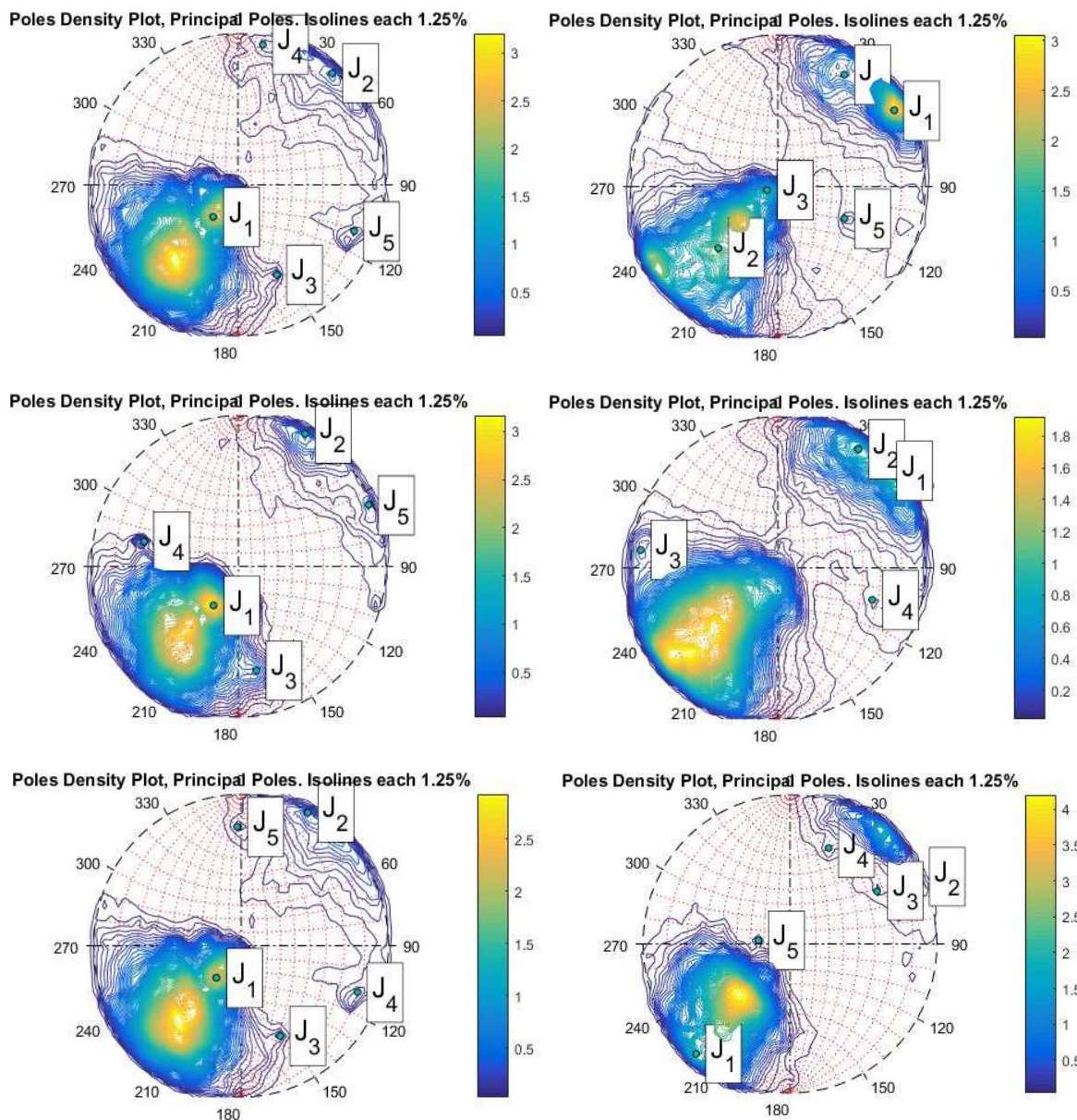


Figure D.63: poles density plot resulting from DSE analysis

Appendix E: photogrammetry normal set spacing

Table E.29 lists, for each set of each blast, the mean, minimum and maximum values of the normal set spacing; the standard deviation is also reported.

Table E.27: values of the normal set spacing for each set of each blast

BLAST 7				
	Mean value	Standard dev	Min value	Max value
SvSE	2.36	2.82	0.12	13.77
Sh	1.70	1.31	0	5.76
SvSW	1.03	1.19	0	5.04
BLAST 8				
	Mean value	Standard dev	Min value	Max value
SvSE	3.42	2.91	0	11.71
Sh	1.72	1.62	0	7.92
SvSW	0.34	0.55	0	3.80
BLAST 9				
	Mean value	Standard dev	Min value	Max value
SvSE	1.53	1.64	0	8.43
Sh	1.30	1.28	0	5.39
SvSW	1.76	1.78	0	9.95
BLAST 10				
	Mean value	Standard dev	Min value	Max value
SvSE	4.20	4.29	0.02	19.72
Sh	1.16	1.04	0	5.27
SvSW	0.73	1.01	0	4.26
BLAST 11				
	Mean value	Standard dev	Min value	Max value
SvSE	3.78	3.72	0.02	15.91
Sh	1.96	1.59	0.08	6.02
SvSW	0.65	0.59	0	2.80
BLAST 12				
	Mean value	Standard dev	Min value	Max value
SvSE	3.25	3.36	0.06	17.22
Sh	1.63	1.66	0.06	8.00
SvSW	0.52	0.57	0	3.22

Appendix F: photogrammetry total spacing

Table F.30 shows the values of mean, minimum and maximum of the total spacing resulting from each scanline. The standard deviation is also reported.

Table F.28: values of total spacing for each of the 3 scanlines for each blast

	Blast 7			Blast 8			Blast 9		
	sc. 1	sc. 2	sc. 3	sc. 1	sc. 2	sc. 3	sc. 1	sc. 2	sc. 3
Mean value	1.05	1.01	1.22	0.77	1.23	1.16	0.53	0.57	0.59
Min value	0.01	0.04	0.25	0.07	0.15	0.08	0.05	0.04	0.05
Max value	3.32	3.38	3.78	2.25	3.24	3.59	1.39	1.71	1.76
Standard dev	0.92	0.74	1.03	0.55	0.96	1.00	0.30	0.43	0.41

	Blast 10			Blast 11			Blast 12		
	sc. 1	sc. 2	sc. 3	sc. 1	sc. 2	sc. 3	sc. 1	sc. 2	sc. 3
Mean value	1.01	1.19	1.49	1.41	0.95	1.41	0.48	0.90	0.97
Min value	0.00	0.07	0.60	0.14	0.07	0.17	0.09	0.02	0.06
Max value	6.33	3.22	3.93	6.03	3.26	6.20	1.57	2.62	3.66
Standard dev	1.24	1.02	0.89	1.39	0.66	1.59	0.35	0.60	0.95

Appendix G: stereograms comparison

Blast № 7

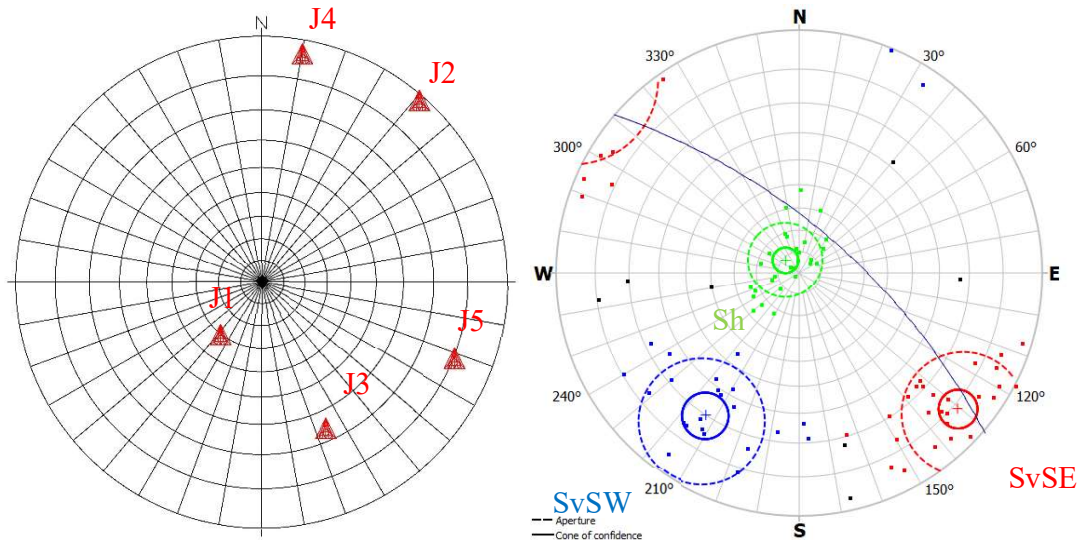


Figure G.64: comparison of pairs of stereograms from DSE and ShapeMetriX software. The matches are J1 with Sh, J2-J4 with SvSW, and J3-J5 with SvSE

Table G.29: sets matches for blast № 7

DSE set	Dip dir (°)	Dip (°)	SMX set	Dip dir (°)	Dip (°)
J1	37.93	30.31	Sh	132.66	8.72
J2	221.03	88.75	SvSW	33.29	69.93
J4	190.17	86.66			
J3	336.24	66.00	SvSE	310.59	81.25
J5	291.48	80.30			

Table G.30: angular distance (°) between matches for blast № 7

	Sh	SvSW	SvSE
J1	32.11	39.75	81.11
J2	88.52	22.63	89.37
J3	74.03	52.67	28.85
J4	82.02	32.60	60.61
J5	88.44	82.43	18.88

Blast № 8

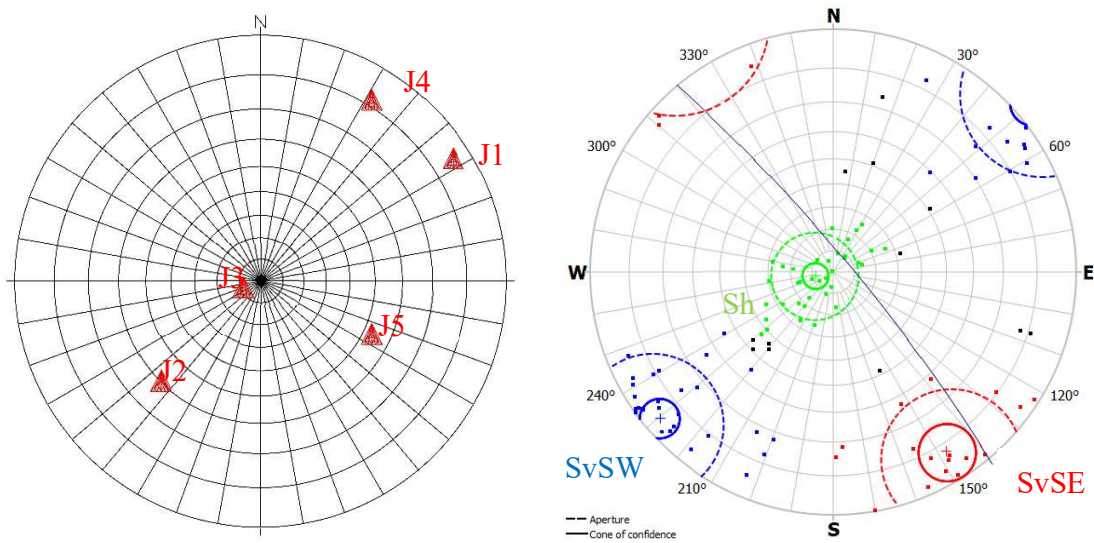


Figure G.65: comparison of pairs of stereograms from DSE and ShapeMetriX software. The matches are J3 with Sh, J1-J2-J4 with SvSW

Table G.31: sets matches for blast № 8

DSE set	Dip dir (°)	Dip (°)	SMX set	Dip dir (°)	Dip (°)
J1	237.58	85.89	SvSW	49.73	85.96
J4	211.54	81.70			
J2	44.97	59.59			
J3	71.12	8.63	Sh	76.41	8.59
J5	295.39	53.20	-	-	-
-	-	-	SvSE	327.75	82.23

Table G.32: angular distance (°) between matches for blast № 8

	Sh	SvSW	SvSE
J1	85.98	11.31	89.61
J2	52.38	26.75	75.08
J3	0.793	77.93	84.30
J4	87.82	21.94	65.57
J5	60.04	73.32	41.30

Blast № 9

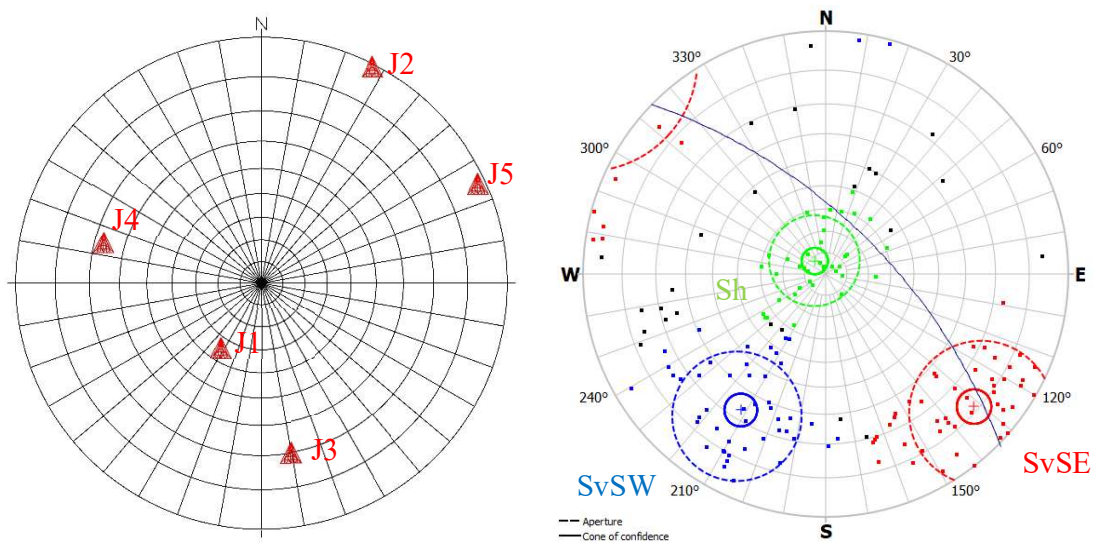


Figure G.66: comparison of pairs of stereograms from DSE and ShapeMetriX software. The matches are J1-J2 with SvSW, and J3 with SvSE

Table G.33: sets matches for blast № 9

DSE set	Dip dir (°)	Dip (°)	SMX set	Dip dir (°)	Dip (°)
J1	32.48	34.49	SvSW	31.98	66.71
J2	207.19	89.40			
J3	350.22	70.00	SvSE	311.75	78.52
J4	104.52	67.16	-	-	-
J5	245.34	88.20	-	-	-
-	-	-	Sh	139.80	7.95

Table G.34: angular distance (°) between matches for blast № 9

	Sh	SvSW	SvSE
J1	37.53	32.22	75.31
J2	86.36	24.33	75.86
J3	76.9	38.82	37.90
J4	60.76	65.95	43.46
J5	89.66	41.02	66.53

Blast № 10

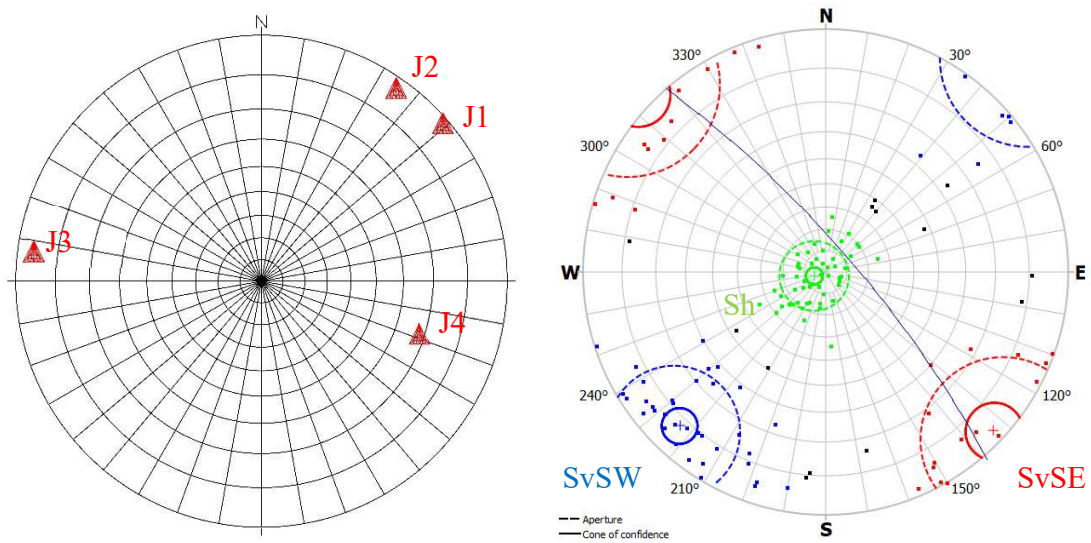


Figure G.67: comparison of pairs of stereograms from DSE and ShapeMetriX software. The matches are J1-J2 with SvSW, and J3-J4 with SvSE

Table G.35: sets matches for blast № 10

DSE set	Dip dir (°)	Dip (°)	SMX set	Dip dir (°)	Dip (°)
J1	228.96	88.76	SvSW	43.51	82.14
J2	214.90	87.51			
J3	97.31	86.19	SvSE	313.37	87.05
J4	288.42	68.25			
-	-	-	Sh	70.85	5.62

Table G.36: angular distance (°) between matches for blast № 10

	Sh	SvSW	SvSE
J1	86.03	10.59	84.35
J2	87.94	13.44	81.67
J3	81.16	53.64	36.66
J4	72.74	70.15	30.67

Blast № 11

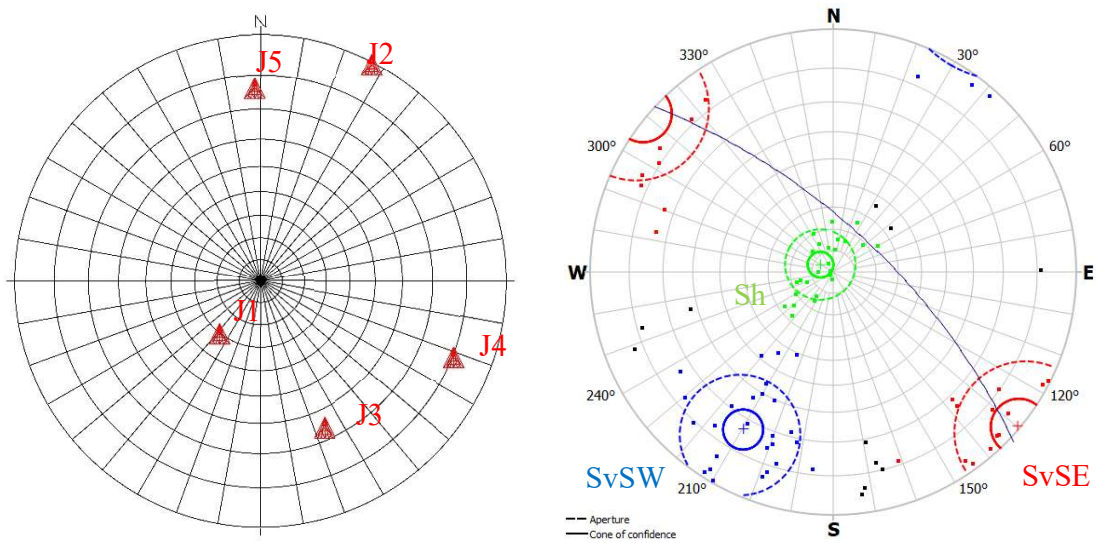


Figure G.68: comparison of pairs of stereograms from DSE and ShapeMetriX software. The matches are J1 with Sh, J2 with SvSW, and J3-J4 with SvSE

Table G.37: sets matches for blast № 11

DSE set	Dip dir (°)	Dip (°)	SMX set	Dip dir (°)	Dip (°)
J1	37.86	30.36	Sh	119.99	6.85
J2	207.19	89.42	SvSW	29.73	73.28
J3	336.24	66.06	SvSE	309.83	89.34
J4	291.50	80.36			
J5	178.27	76.32	-	-	-

Table G.38: angular distance (°) between matches for blast № 11

	Sh	SvSW	SvSE
J1	30.12	43.32	88.43
J2	89.09	17.48	77.36
J3	71.64	50.39	34.59
J4	87.14	85	20.32
J5	72.8	43.47	50.07

Blast № 12

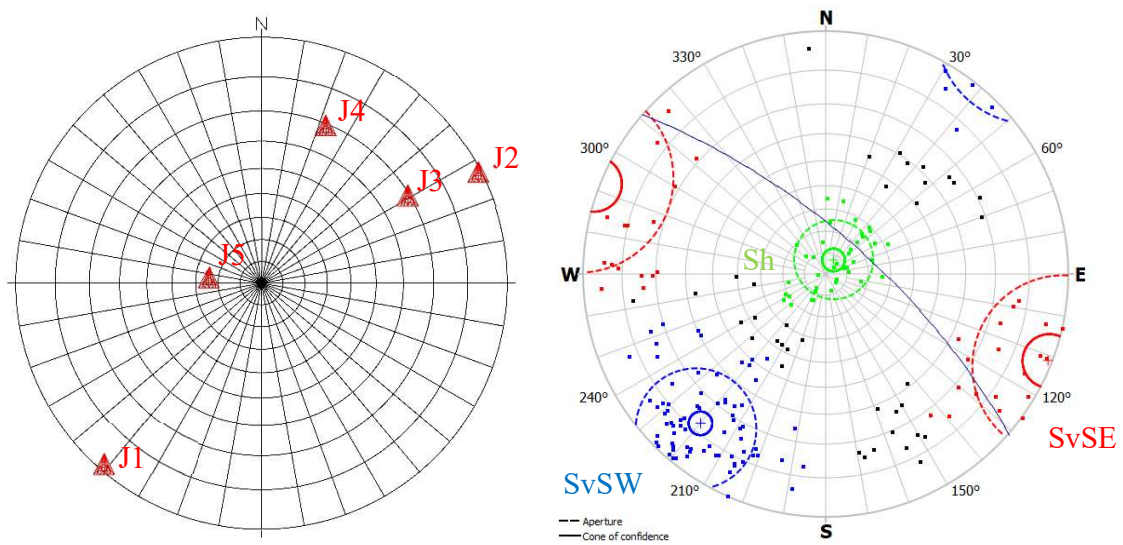


Figure G.69: comparison of pairs of stereograms from DSE and ShapeMetriX software. The matches are J5 with Sh, and J1-J2-J3-J4 with SvSW

Table G.39: sets matches for blast № 12

DSE set	Dip dir (°)	Dip (°)	SMX set	Dip dir (°)	Dip (°)
J1	41.07	88.67	SvSW	40.00	77.42
J2	242.85	89.36			
J3	239.07	69.45			
J4	202.20	69.42			
J5	96.31	24.28	Sh	209.29	7.55
-	-	-	SvSE	291.23	89.01

Table G.40: angular distance (°) between matches for blast № 12

	Sh	SvSW	SvSE
J1	83.94	11.29	70.19
J2	83.08	26.24	48.37
J3	62.95	38.06	54.52
J4	61.93	37.49	88.74
J5	28.05	65.09	67.57

Appendix H: normal spacing comparison

Table H.41: comparison of the mean normal set spacing and its relative standard deviation for each set of each blast

BLAST 7					
DSE set	Mean value	St. dev.	SMX set	Mean value	St. dev.
J1	1.07	0.88	Sh	1.70	1.31
J2	0.8	0.66	SvSW	1.03	1.19
J4	1.54	1.05			
J3	2.05	1.76	SvSE	2.36	2.82
J5	2.6	2.14			

BLAST 8					
DSE set	Mean value	St. dev.	SMX set	Mean value	St. dev.
J1	0.84	0.66	SvSW	0.34	0.55
J4	0.67	0.48			
J2	0.71	0.66			
J3	2.08	1.96	Sh	1.72	1.62
J5	3.31	2.53	-	-	-
-	-	-	SvSE	3.42	2.91

BLAST 9					
DSE set	Mean value	St. dev.	SMX set	Mean value	St. dev.
J1	0.92	0.74	SvSW	1.76	1.78
J2	1.07	0.88			
J3	1.36	1.1	SvSE	1.53	1.64
J4	2.3	1.51	-	-	-
J5	2.08	1.38	-	-	-
-	-	-	Sh	1.30	1.28

BLAST 10					
DSE set	Mean value	St. dev.	SMX set	Mean value	St. dev.
J1	1.58	1.03	SvSW	0.73	1.01
J2	0.94	0.64			
J3	1.2	0.82	SvSE	4.20	4.29
J4	2.87	1.92			
-	-	-	Sh	1.16	1.04

BLAST 11					
DSE set	Mean value	St. dev.	SMX set	Mean value	St. dev.
J1	1.05	0.79	Sh	1.96	1.59
J2	0.85	0.67	SvSW	0.65	0.59
J3	1.87	1.37	SvSE	3.78	3.72
J4	2.6	1.89			
J5	2.02	1.5	-	-	-

BLAST 12					
DSE set	Mean value	St. dev.	SMX set	Mean value	St. dev.
J1	0.87	0.74	SvSW	0.52	0.57
J2	0.7	0.53			
J3	2.26	2.88			
J4	2.04	1.99			
J5	0.95	0.07	Sh	1.63	1.66
-	-	-	SvSE	3.25	3.36

Appendix I: rock factors

Blastability index

Table I.42: Blastability index results for each DSE set of blast № 7

BLAST 7						
set		J1	J2	J3	J4	J5
JPA	Dip Dir/Dip (°/°)	37.93/30.31	221.03/88.75	336.24/66.00	190.17/86.66	291.48/80.30
	Set/face orientation	horizontal	parallel	strike perp.	strike perp.	strike perp.
	Assigned value	10	40	30	30	30
JPS	Normal spacing Sj (m)	1.07	0.8	2.05	1.54	2.6
	Burden B (m)	3.5				
	Spacing S (m)	3.72				
	Assigned value	80	80	80	80	80
JF=JPA+JPS		90	120	110	110	110
RMD=JF (vertically jointed)		90	120	110	110	110
RDI=25*RD-50	Rock density RD (t/m ³)	2.71				
	Final value	17.75				
HF=Y/3 (Y<50)	Young's Modulus Y (GPa)	19.8				
	Final value	6.6				
BLASTABILITY INDEX A=0.06*(RMD+RDI+HF)		6.861	8.661	8.061	8.061	8.061

I. Table 43: Blastability index results for each DSE set of blast № 8

BLAST 8						
set		J1	J2	J3	J4	J5
JPA	Dip Dir/Dip (°/°)	237.58/85.89	44.97/59.59	71.12/ 8.63	211.54/81.70	295.39/53.20
	Set/face orientation	parallel	dip into	dip into	dip out	strike perp.
	Assigned value	40	40	40	20	30
JPS	Normal spacing Sj (m)	0.84	0.71	2.08	0.67	3.31
	Burden B (m)	4.11				
	Spacing S (m)	3.73				
	Assigned value	80	80	80	80	80
JF=JPA+JPS		120	120	120	100	110
RMD=JF (vertically jointed)		120	120	120	100	110
RDI=25*RD-50	Rock density RD (t/m ³)	2.71				
	Final value	17.75				
HF=Y/3 (Y<50)	Young's Modulus Y (GPa)	19.8				
	Final value	6.6				
BLASTABILITY INDEX A=0.06*(RMD+RDI+HF)		8.661	8.661	8.661	7.461	8.061

Table I.44: Blastability index results for each DSE set of blast № 9

BLAST 9						
set		J1	J2	J3	J4	J5
JPA	Dip Dir/Dip (°/°)	32.48/34.49	207.19/89.40	350.22/70.00	104.52/67.16	245.34/88.20
	Set/face orientation	dip into	parallel	strike perp.	strike perp.	parallel
	Assigned value	40	40	30	30	40
JPS	Normal spacing S _j (m)	0.92	1.07	1.36	2.3	2.08
	Burden B (m)	3.19				
	Spacing S (m)	3.83				
	Assigned value	80	80	80	80	80
JF=JPA+JPS		120	120	110	110	120
RMD=JF (vertically jointed)		120	120	110	110	120
RDI=25*RD-50	Rock density RD (t/m ³)	2.71				
	Final value	17.75				
HF=Y/3 (Y<50)	Young's Modulus Y (GPa)	19.8				
	Final value	6.6				
BLASTABILITY INDEX A=0.06*(RMD+RDI+HF)		8.661	8.661	8.061	8.061	8.661

Table I.45: Blastability index results for each DSE set of blast № 10

BLAST 10						
set		J1	J2	J3	J4	J5
JPA	Dip Dir/Dip (°/°)	228.96/88.76	214.90/87.51	97.31/86.19	288.42/68.25	-
	Set/face orientation	parallel	parallel	strike perp.	strike perp.	-
	Assigned value	40	40	30	30	-
JPS	Normal spacing S _j (m)	1.58	0.94	1.2	2.87	-
	Burden B (m)	3.37				-
	Spacing S (m)	3.68				-
	Assigned value	80	80	80	80	-
JF=JPA+JPS		120	120	110	110	-
RMD=JF (vertically jointed)		120	120	110	110	-
RDI=25*RD-50	Rock density RD (t/m ³)	2.71				-
	Final value	17.75				-
HF=Y/3 (Y<50)	Young's Modulus Y (GPa)	19.8				-
	Final value	6.6				-
BLASTABILITY INDEX A=0.06*(RMD+RDI+HF)		8.661	8.661	8.061	8.061	-

Table I.46: Blastability index results for each DSE set of blast № 11

BLAST 11						
set		J1	J2	J3	J4	J5
JPA	Dip Dir/Dip (°/°)	37.86/30.36	207.19/89.42	336.24/66.06	291.50/80.36	178.27/76.32
	Set/face orientation	horizontal	parallel	strike perp.	strike perp.	strike perp.
	Assigned value	10	40	30	30	30
JPS	Normal spacing S _j (m)	1.05	0.85	1.87	2.6	2.02
	Burden B (m)	3.3				
	Spacing S (m)	4.23				
	Assigned value	80	80	80	80	80
JF=JPA+JPS		90	120	110	110	110
RMD=JF (vertically jointed)		90	120	110	110	110
RDI=25*RD-50	Rock density RD (t/m ³)	2.71				
	Final value	17.75				
HF=Y/3 (Y<50)	Young's Modulus Y (GPa)	19.8				
	Final value	6.6				
BLASTABILITY INDEX A=0.06*(RMD+RDI+HF)		6.861	8.661	8.061	8.061	8.061

Table I.47: Blastability index results for each DSE set of blast № 12

BLAST 12						
set		J1	J2	J3	J4	J5
JPA	Dip Dir/Dip (°/°)	41.068/88.665	242.85/89.358	239.07/69.453	202.2/69.416	96.308/24.283
	Set/face orientation	dip into	parallel	dip out	dip out	strike perp.
	Assigned value	40	40	20	20	30
JPS	Normal spacing S _j (m)	0.87	0.7	2.26	2.04	0.95
	Burden B (m)	3.23				
	Spacing S (m)	3.66				
	Assigned value	80	80	80	80	80
JF=JPA+JPS		120	120	100	100	110
RMD=JF (vertically jointed)		120	120	100	100	110
RDI=25*RD-50	Rock density RD (t/m ³)	2.71				
	Final value	17.75				
HF=Y/3 (Y<50)	Young's Modulus Y (GPa)	19.8				
	Final value	6.6				
BLASTABILITY INDEX A=0.06*(RMD+RDI+HF)		8.661	8.661	7.461	7.461	8.061

Table I.48: Blastability index results for each ShapeMetriX set of blast № 7

BLAST 7				
set		SvSE	Sh	SvSW
JPA	Dip Dir/Dip (°/°)	310,58/81,24	132,65/8,72	33,29/69,93
	Set/face orientation	stike perp.	horizontal	dip into
	Assigned value	30	10	40
JPS	Normal spacing Sj (m)	2.36	1.70	1.03
	Burden B (m)	3.5		
	Spacing S (m)	3.72		
	Assigned value	80	80	80
JF=JPA+JPS		110	90	120
RMD=JF (vertically jointed)		110	90	120
RDI=25*RD-50	Rock density RD (t/m3)	2.71		
	Final value	17.75		
HF=Y/3 (Y<50)	Young's Modulus Y (GPa)	19.8		
	Final value	6.6		
BLASTABILITY INDEX A=0.06*(RMD+RDI+HF)		8.061	6.861	8.661

Table I.49: Blastability index results for each ShapeMetriX set of blast № 8

BLAST 8				
set		SvSE	Sh	SvSW
JPA	Dip Dir/Dip (°/°)	327,74/82,22	76,40/8,58	49,72/85,95
	Set/face orientation	stike perp.	horizontal	dip into
	Assigned value	30	10	40
JPS	Normal spacing Sj (m)	3.42	1.72	0.34
	Burden B (m)	4.11		
	Spacing S (m)	3.73		
	Assigned value	80	80	80
JF=JPA+JPS		110	90	120
RMD=JF (vertically jointed)		110	90	120
RDI=25*RD-50	Rock density RD (t/m3)	2.71		
	Final value	17.75		
HF=Y/3 (Y<50)	Young's Modulus Y (GPa)	19.8		
	Final value	6.6		
BLASTABILITY INDEX A=0.06*(RMD+RDI+HF)		8.061	6.861	8.661

I. Table 50: Blastability index results for each ShapeMetriX set of blast № 9

BLAST 9				
set		SvSE	Sh	SvSW
JPA	Dip Dir/Dip (°/°)	311,74/78,51	139,79/7,94	31,98/66,71
	Set/face orientation	stike perp.	horizontal	dip into
	Assigned value	30	10	40
JPS	Normal spacing Sj (m)	1.53	1.30	1.76
	Burden B (m)	3.19		
	Spacing S (m)	3.83		
	Assigned value	80	80	80
JF=JPA+JPS		110	90	120
RMD=JF (vertically jointed)		110	90	120
RDI=25*RD-50	Rock density RD (t/m3)	2.71		
	Final value	17.75		
HF=Y/3 (Y<50)	Young's Modulus Y (GPa)	19.8		
	Final value	6.6		
BLASTABILITY INDEX A=0.06*(RMD+RDI+HF)		8.061	6.861	8.661

Table I.51: Blastability index results for each ShapeMetriX set of blast № 10

BLAST 10				
set		SvSE	Sh	SvSW
JPA	Dip Dir/Dip (°/°)	313,37/87,04	70,84/5,61	43,51/82,13
	Set/face orientation	stike perp.	horizontal	dip into
	Assigned value	30	10	40
JPS	Normal spacing Sj (m)	4.20	1.16	0.73
	Burden B (m)	3.37		
	Spacing S (m)	3.68		
	Assigned value	50	80	80
JF=JPA+JPS		80	90	120
RMD=JF (vertically jointed)		80	90	120
RDI=25*RD-50	Rock density RD (t/m3)	2.71		
	Final value	17.75		
HF=Y/3 (Y<50)	Young's Modulus Y (GPa)	19.8		
	Final value	6.6		
BLASTABILITY INDEX A=0.06*(RMD+RDI+HF)		6.261	6.861	8.661

Table I.52: Blastability index results for each ShapeMetriX set of blast № 11

BLAST 11				
set		SvSE	Sh	SvSW
JPA	Dip Dir/Dip (°/°)	309,83/89,33	119,99/6,84	29,72/73,27
	Set/face orientation	stike perp.	horizontal	dip into
	Assigned value	30	10	40
JPS	Normal spacing Sj (m)	3.78	1.96	0.65
	Burden B (m)	3.3		
	Spacing S (m)	4.23		
	Assigned value	50	80	80
JF=JPA+JPS		80	90	120
RMD=JF (vertically jointed)		80	90	120
RDI=25*RD-50	Rock density RD (t/m3)	2.71		
	Final value	17.75		
HF=Y/3 (Y<50)	Young's Modulus Y (GPa)	19.8		
	Final value	6.6		
BLASTABILITY INDEX A=0.06*(RMD+RDI+HF)		6.261	6.861	8.661

Table I.53: Blastability index results for each ShapeMetriX set of blast № 12

BLAST 12				
set		SvSE	Sh	SvSW
JPA	Dip Dir/Dip (°/°)	291,22/89,01	209,29/7,54	39,99/77,42
	Set/face orientation	stike perp.	horizontal	dip into
	Assigned value	30	10	40
JPS	Normal spacing Sj (m)	3.25	1.63	0.52
	Burden B (m)	3.23		
	Spacing S (m)	3.66		
	Assigned value	80	80	80
JF=JPA+JPS		110	90	120
RMD=JF (vertically jointed)		110	90	120
RDI=25*RD-50	Rock density RD (t/m3)	2.71		
	Final value	17.75		
HF=Y/3 (Y<50)	Young's Modulus Y (GPa)	19.8		
	Final value	6.6		
BLASTABILITY INDEX A=0.06*(RMD+RDI+HF)		8.061	6.861	8.661

Table I.54: Blastability index value for each LiDAR and photogrammetry sets

DSE set		ShapeMetriX set	
BLAST 7			
J1	6.86	Sh	6.86
J2	8.66	SvSW	8.66
J4	8.06		
J3	8.06	SvSE	8.06
J5	8.06		
BLAST 8			
J1	8.66	SvSW	8.66
J4	7.46		
J2	8.66		
J3	8.66	Sh	6.86
J5	8.06	SvSE	8.06
BLAST 9			
J1	8.66	-	-
J3	8.06	SvSE	8.06
J4	8.06	Sh	6.86
J2	8.66	SvSW	8.66
J5	8.66		
BLAST 10			
J1	8.66	Sh	6.86
J3	8.06		
J2	8.66		
J4	8.06	SvSE	6.26
-	-	SvSW	8.66
BLAST 11			
J1	6.86	-	-
J2	8.66	SvSW	8.66
J3	8.06	SvSE	6.26
J4	8.06	Sh	6.86
J5	8.06	-	-
BLAST 12			
J1	8.66	SvSW	8.66
J2	8.66		
J3	7.46		
J4	7.46		
J5	8.06	Sh	6.86
-	-	SvSE	8.06

Rock mass discontinuity factor

Table I.55: Rock mass discontinuity factor results for each DSE set of blast № 7

BLAST 7						
set		J1	J2	J3	J4	J5
Joint spacing term J_S	Normal spacing S_j (m)	1.07	0.8	2.05	1.54	2.6
	Characteristic size L_j (m)	3.5				
	Fraction passing value P	0.5				
	Limiting value a_s	0.77				
	Final value	0.31	0.23	0.59	0.44	0.74
Joint orientation term J_O	Dip Dir/Dip ($^\circ$)	37.93/30.31	221.03/88.75	336.24/66.00	190.17/86.66	291.48/80.30
	Set/face orientation	horizontal	parallel	strike perp.	strike perp.	strike perp.
	Joint orientation index j_{oi}	0.25	1	0.75	0.75	0.75
	Constant a_O	0.43				
	Final value	0.11	0.43	0.32	0.32	0.32
Rock mass discontinuity factor J_F		0.41	0.66	0.91	0.76	1.06

Table I.56: Rock mass discontinuity factor results for each DSE set of blast № 8

BLAST 8						
set		J1	J2	J3	J4	J5
Joint spacing term J_S	Normal spacing S_j (m)	0.84	0.71	2.08	0.67	3.31
	Characteristic size L_j (m)	4.11				
	Fraction passing value P	0.5				
	Limiting value a_s	0.77				
	Final value	0.20	0.17	0.51	0.16	0.77
Joint orientation term J_O	Dip Dir/Dip ($^\circ$)	237.58/85.89	44.97/59.59	71.12/ 8.63	211.54/81.70	295.39/53.20
	Set/face orientation	parallel	dip into	dip into	dip out	strike perp.
	Joint orientation index j_{oi}	1	1	1	0.5	0.75
	Constant a_O	0.43				
	Final value	0.43	0.43	0.43	0.21	0.32
Rock mass discontinuity factor J_F		0.63	0.60	0.93	0.38	1.09

Table I.57: Rock mass discontinuity factor results for each DSE set of blast № 9

BLAST 9						
set		J1	J2	J3	J4	J5
Joint spacing term J_S	Normal spacing S_j (m)	0.92	1.07	1.36	2.3	2.08
	Characteristic size L_j (m)	3.19				
	Fraction passing value P	0.5				
	Limiting value a_s	0.77				
	Final value	0.29	0.34	0.43	0.72	0.65
Joint orientation term J_O	Dip Dir/Dip ($^\circ$)	32.48/34.49	207.19/89.40	350.22/70.00	104.52/67.16	245.34/88.20
	Set/face orientation	dip into	parallel	strike perp.	strike perp.	parallel
	Joint orientation index j_{oi}	1	1	0.75	0.75	1
	Constant a_O	0.43				
	Final value	0.43	0.43	0.32	0.32	0.43
Rock mass discontinuity factor J_F		0.72	0.76	0.75	1.04	1.08

Table I.58: Rock mass discontinuity factor results for each DSE set of blast № 10

BLAST 10						
set		J1	J2	J3	J4	J5
Joint spacing term J_S	Normal spacing S_j (m)	1.58	0.94	1.2	2.87	-
	Characteristic size L_j (m)	3.37				-
	Fraction passing value P	0.5				-
	Limiting value a_s	0.77				-
	Final value	0.47	0.28	0.36	0.77	-
Joint orientation term J_O	Dip Dir/Dip ($^\circ$)	228.96/88.76	214.90/87.51	97.31/86.19	288.42/68.25	-
	Set/face orientation	parallel	parallel	strike perp.	strike perp.	-
	Joint orientation index j_{oi}	1	1	0.75	0.75	-
	Constant a_O	0.43				-
	Final value	0.43	0.43	0.32	0.32	-
Rock mass discontinuity factor J_F		0.90	0.71	0.68	1.09	-

Table I.59: Rock mass discontinuity factor results for each DSE set of blast № 11

BLAST 11						
set		J1	J2	J3	J4	J5
Joint spacing term J_S	Normal spacing S_j (m)	1.05	0.85	1.87	2.6	2.02
	Characteristic size L_j (m)	3.3				
	Fraction passing value P	0.5				
	Limiting value a_s	0.77				
	Final value	0.32	0.26	0.57	0.77	0.61
Joint orientation term J_O	Dip Dir/Dip ($^\circ$)	37.86/30.36	207.19/89.42	336.24/66.06	291.50/80.36	178.27/76.32
	Set/face orientation	horizontal	parallel	strike perp.	strike perp.	strike perp.
	Joint orientation index j_{oi}	0.25	1	0.75	0.75	0.75
	Constant a_O	0.43				
	Final value	0.11	0.43	0.32	0.32	0.32
Rock mass discontinuity factor J_F		0.42	0.68	0.89	1.09	0.93

Table I.60: Rock mass discontinuity factor results for each DSE set of blast № 12

BLAST 12						
set		J1	J2	J3	J4	J5
Joint spacing term J_S	Normal spacing S_j (m)	0.87	0.7	2.26	2.04	0.95
	Characteristic size L_j (m)	3.23				
	Fraction passing value P	0.5				
	Limiting value a_s	0.77				
	Final value	0.27	0.22	0.70	0.63	0.29
Joint orientation term J_O	Dip Dir/Dip ($^\circ$)	41.07/88.67	242.85/89.36	239.07/69.45	202.2/69.41	96.31/24.28
	Set/face orientation	dip into	parallel	dip out	dip out	strike perp.
	Joint orientation index j_{oi}	1	1	0.5	0.5	0.75
	Constant a_O	0.43				
	Final value	0.43	0.43	0.21	0.21	0.32
Rock mass discontinuity factor J_F		0.70	0.64	0.91	0.85	0.61

Table I.61: Rock mass discontinuity factor results for each ShapeMetriX set of blast № 7

BLAST 7				
set		SvSE	Sh	SvSW
Joint spacing term J_s	Normal spacing S _j (m)	2.36	1.70	1.03
	Characteristic size L _j (m)	3.5		
	Fraction passing value P	0.5		
	Limiting value a _s	0.77		
	Final value	0.68	0.49	0.30
Joint orientation term J_o	Dip Dir/Dip (°/°)	310,58/81,24	132,65/8,72	33,29/69,93
	Set/face orientation	stike perp.	horizontal	dip into
	Joint orientation index j _{oi}	0.75	0.25	1
	Constant a _o	0.43		
	Final value	0.32	0.11	0.43
Rock mass discontinuity factor J_F		1.00	0.59	0.72

Table I.62: Rock mass discontinuity factor results for each ShapeMetriX set of blast № 8

BLAST 8				
set		SvSE	Sh	SvSW
Joint spacing term J_s	Normal spacing S _j (m)	3.42	1.72	0.34
	Characteristic size L _j (m)	4.11		
	Fraction passing value P	0.5		
	Limiting value a _s	0.77		
	Final value	0.77	0.42	0.08
Joint orientation term J_o	Dip Dir/Dip (°/°)	327,74/82,22	76,40/8,58	49,72/85,95
	Set/face orientation	stike perp.	horizontal	dip into
	Joint orientation index j _{oi}	0.75	0.25	1
	Constant a _o	0.43		
	Final value	0.32	0.11	0.43
Rock mass discontinuity factor J_F		1.09	0.52	0.51

Table I.63: Rock mass discontinuity factor results for each ShapeMetriX set of blast № 9

BLAST 9				
set		SvSE	Sh	SvSW
Joint spacing term J_s	Normal spacing S_j (m)	1.53	1.30	1.76
	Characteristic size L_j (m)	3.19		
	Fraction passing value P	0.5		
	Limiting value a_s	0.77		
	Final value	0.48	0.41	0.55
Joint orientation term J_o	Dip Dir/Dip ($^\circ$)	311,74/78,51	139,79/7,94	31,98/66,71
	Set/face orientation	stike perp.	horizontal	dip into
	Joint orientation index j_{oi}	0.75	0.25	1
	Constant a_o	0.43		
	Final value	0.32	0.11	0.43
Rock mass discontinuity factor J_F		0.80	0.51	0.98

Table I.64: Rock mass discontinuity factor results for each ShapeMetriX set of blast № 10

BLAST 10				
set		SvSE	Sh	SvSW
Joint spacing term J_s	Normal spacing S_j (m)	4.20	1.16	0.73
	Characteristic size L_j (m)	3.37		
	Fraction passing value P	0.5		
	Limiting value a_s	0.77		
	Final value	0.77	0.35	0.22
Joint orientation term J_o	Dip Dir/Dip ($^\circ$)	313,37/87,04	70,84/5,61	43,51/82,13
	Set/face orientation	stike perp.	horizontal	dip into
	Joint orientation index j_{oi}	0.75	0.25	1
	Constant a_o	0.43		
	Final value	0.32	0.11	0.43
Rock mass discontinuity factor J_F		1.09	0.45	0.64

Table I.65: Rock mass discontinuity factor results for each ShapeMetriX set of blast № 11

BLAST 11				
set		SvSE	Sh	SvSW
Joint spacing term J_s	Normal spacing S _j (m)	3.78	1.96	0.65
	Characteristic size L _j (m)	3.3		
	Fraction passing value P	0.5		
	Limiting value a _s	0.77		
	Final value	0.77	0.60	0.20
Joint orientation term J_o	Dip Dir/Dip (°/°)	309,83/89,33	119,99/6,84	29,72/73,27
	Set/face orientation	stike perp.	horizontal	dip into
	Joint orientation index j _{oi}	0.75	0.25	1
	Constant a _o	0.43		
	Final value	0.32	0.11	0.43
Rock mass discontinuity factor J_F		1.09	0.70	0.62

Table I.66: Rock mass discontinuity factor results for each ShapeMetriX set of blast № 12

BLAST 12				
set		SvSE	Sh	SvSW
Joint spacing term J_s	Normal spacing S _j (m)	3.25	1.63	0.52
	Characteristic size L _j (m)	3.23		
	Fraction passing value P	0.5		
	Limiting value a _s	0.77		
	Final value	0.77	0.50	0.16
Joint orientation term J_o	Dip Dir/Dip (°/°)	291,22/89,01	209,29/7,54	39,99/77,42
	Set/face orientation	stike perp.	horizontal	dip into
	Joint orientation index j _{oi}	0.75	0.25	1
	Constant a _o	0.43		
	Final value	0.32	0.11	0.43
Rock mass discontinuity factor J_F		1.09	0.61	0.59

Table I.67: Rock mass discontinuity factor value for each LiDAR and photogrammetry sets

BLAST 7			
DSE set		ShapeMetriX set	
J1	0.41	Sh	0.59
J2	0.66	SvSW	0.72
J4	0.76		
J3	0.91	SvSE	1.00
J5	1.06		
BLAST 8			
DSE set		ShapeMetriX set	
J1	0.63	SvSW	0.51
J4	0.38		
J2	0.60		
J3	0.93	Sh	0.52
J5	1.09	SvSE	1.09
BLAST 9			
DSE set		ShapeMetriX set	
J1	0.72	-	-
J3	0.75	SvSE	0.80
J4	1.04	Sh	0.51
J2	0.76	SvSW	0.98
J5	1.08		
BLAST 10			
DSE set		ShapeMetriX set	
J1	0.90	Sh	0.45
J3	0.68		
J2	0.71		
J4	1.09	SvSE	1.09
-	-	SvSW	0.64
BLAST 11			
DSE set		ShapeMetriX set	
J1	0.42	-	-
J2	0.68	SvSW	0.62
J3	0.89	SvSE	1.09
J4	1.09	Sh	0.70
J5	0.93	-	-
BLAST 12			
DSE set		ShapeMetriX set	
J1	0.70	SvSW	0.59
J2	0.64		
J3	0.91		
J4	0.85		
J5	0.61	Sh	0.61
-	-	SvSE	1.09